UNIVERSIDAD COMPLUTENSE DE MADRID
FACULTAD DE CIENCIAS FÍSICAS

TESIS DOCTORAL

Estudio de primeros principios de propiedades magnéticas en óxidos complejos basados en ferritas

Ab-initio study of magnetic properties of complex oxides based on ferrites

MEMORIA PARA OPTAR AL GRADO DE DOCTOR

PRESENTADA POR

César Tejera Centeno

Directora

Silvia Gallego Queipo

Madrid

UNIVERSIDAD COMPLUTENSE DE MADRID

FACULTAD DE CIENCIAS FÍSICAS

TESIS DOCTORAL

Estudio de primeros principios de propiedades magnéticas en óxidos complejos basados en ferritas

Ab-initio study of magnetic properties of complex oxides based on ferrites

MEMORIA PARA OPTAR AL GRADO DE DOCTOR

PRESENTADA POR

César Tejera Centeno

DIRECTORA

Silvia Gallego Queipo

Ab-initio study of magnetic properties of complex oxides based on ferrites

-

Estudio de primeros principios de propiedades magnéticas en óxidos complejos basados en ferritas

Memoria para optar al grado de
Doctor en Ciencias Físicas por la

UNIVERSIDAD
COMPLUTENSE
MADRID

Facultad de Ciencias Físicas

presentada por
César Tejera Centeno

Directora

Silvia Gallego Queipo

Instituto de Ciencia de Materiales de Madrid (ICMM-CSIC)

Contents

Chaos is found in greatest abundance wherever order is being sought. It always defeats order, because it is better organized.

Terry Pratchett

Abstract

Permanent magnets are nowadays regarded as essential, meaning they cannot be replaced by other materials, for many different technological applications. The most powerful magnets contain rare-earths, elements that are at supply risk for the European Union (EU) and other regions, as China controls more than 80% of their global production. Besides, mining rare-earths is environmentally harmful and causes serious human health problems. This has moved the EU to promote research on rare-earth free magnets, an initiative that perfectly fits with the carbon-neutral goals and European Green Deal. This is the framework of this PhD thesis, developed under the H2020 EU project Amphibian, "Anisometric permanent hybrid magnets based on inexpensive and non-critical materials". The work presented here is devoted to the fundamental description of the electronic and magnetic properties of rare-earth free ferrite-based permanent magnets, using *ab initio* simulations. Its ultimate objective is to contribute from a theoretical approach to the improvement of the magnetic performance of these materials, as a way to minimize the dependence on critical rare-earth permanent magnets.

First, we address a description based on the density functional theory (DFT) of the hexagonal $SrFe_{12}O_{19}$ and cubic $CoFe_2O_4$, $NiFe_2O_4$, $MnFe_2O_4$ and $ZnFe_2O_4$ spinel ferrites, materials of different magnetic complexity. The bulk form of the cubic ferrites has already been described by DFT, while our work is pioneer in the simulation of $SrFe_{12}O_{19}$. However, we also revisit some previous assumptions on the theoretical conditions used to describe cubic ferrites, particularly relevant for $ZnFe_2O_4$, and we thoroughly explore the influence of different theoretical details on the quantitative determination of the magnetic exchange constants. Though our work is mainly focused on the *ab initio* determination of the magnetic properties, *i.e.* local moments, anisotropies and exchange constants, we also explore beyond-DFT methodologies to determine magnetic critical temperatures, demonstrating the better accuracy of Monte Carlo methods over mean field approaches. An important conclusion of this part of the PhD thesis is the ability to use the magnetic properties as targets to determine the best Hubbard U potential

that enters into the exchange correlation functional.

The study of the bulk oxides serves as the necessary departing point to the ensuing simulations of modifications intended to overcome the current magnetic performance of rare-earth free permanent magnets. Simulations of these systems constitute the second part of this PhD thesis. The specific systems have been chosen in the context of supporting experimental efforts within the framework of the Amphibian project, and are representative of nanostructured bicomponent permanent magnets that combine hard and soft magnets. In particular, we explore the ability of substitutional Zn cations at $NiFe_2O_4$ to increase the magnetization of this soft magnet, analyzing different dopant concentrations and distributions at the atomic level. Our results put limits on the success of this procedure to enhance the magnetization, due to the tendency of Zn atoms to distribute at both tetrahedral and octahedral coordination sites. We also analyze the contribution of interface effects to the magnetism of bicomponent soft/hard nanostructures based on $CoFe_2O_4$, $NiFe_2O_4$ and $MnFe_2O_4$. Our results identify the balance between inverse and direct spinel forms as the most determinant feature for the magnetic performance of these materials, identifying some of the relevant aspects that influence this balance. In addition, from the theoretical point of view, we demonstrate the fundamental role of the localization of the electrons governed by the local Hubbard U term. Besides its well known role in the electronic properties and the definition of the electronic gap, it is also crucial to determine the structural properties that govern the magnetic performance of these ferrites. Finally, we demonstrate that, even though most global magnetic properties at the bicomponent system correspond to the sum of the individual contributions of the bulk counterparts, the interface introduces relevant redistributions and local modifications.

Resumen

Los imanes permanentes se consideran hoy en día esenciales, es decir, no pueden ser sustituidos por otros materiales, para muchas aplicaciones tecnológicas diferentes. Los imanes más potentes contienen tierras raras, elementos que suponen un riesgo de suministro para la Unión Europea (UE) y otras regiones, ya que China controla más del 80% de su producción mundial. Además, la extracción de tierras raras es perjudicial para el medio ambiente, e incluso puede llegar a causar graves problemas de salud humana. Esto ha movido a la UE a promover la investigación sobre imanes sin tierras raras, una iniciativa que encaja perfectamente con los objetivos de la neutralidad de carbono y el Pacto Verde Europeo. En este contexto se enmarca esta tesis doctoral, desarrollada en el marco del proyecto europeo H2020 Amphibian, "Imanes híbridos permanentes anisométricos basados en materiales baratos y no críticos". El trabajo que aquí se presenta está dedicado a la descripción fundamental, utilizando simulaciones *ab initio*, de las propiedades electrónicas y magnéticas de imanes permanentes basados en ferritas libres de tierras raras. Su objetivo último es contribuir desde un enfoque teórico a la mejora de las propiedades magnéticas de estos materiales, como forma de minimizar la dependencia de los imanes permanentes de tierras raras.

En primer lugar, se aborda una descripción basada en la teoría del funcional de la densidad (DFT) de las ferritas hexagonales $SrFe_{12}O_{19}$ y cúbicas $CoFe_2O_4$, $NiFe_2O_4$, $MnFe_2O_4$ y $ZnFe_2O_4$, materiales de diferente complejidad magnética. La forma de volumen de las ferritas cúbicas ya ha sido descrita por DFT, mientras que nuestro trabajo es pionero en la simulación de $SrFe_{12}O_{19}$. Sin embargo, también reexaminamos algunas de las asunciones comúnmente aceptadas sobre las condiciones teóricas utilizadas para describir las ferritas cúbicas, particularmente relevantes para el $ZnFe_2O_4$, y exploramos a fondo la influencia de diferentes detalles teóricos en la determinación cuantitativa de las constantes de canje magnético. Aunque nuestro trabajo se centra principalmente en la determinación de las propiedades magnéticas, momentos locales, anisotropías y constantes de canje, también exploramos metodologías más allá de DFT para determinar las temperaturas críticas

magnéticas, demostrando que los métodos de Monte Carlo tienen mayor precisión que los enfoques de campo medio. Una conclusión importante de esta parte de la tesis doctoral es la capacidad de utilizar las propiedades magnéticas como referencia para determinar el mejor potencial de Hubbard U empleado en el funcional de canje-correlación.

El estudio de los volúmenes de los óxidos sirve como punto de partida necesario para las subsiguientes simulaciones basadas en modificaciones destinadas a superar el rendimiento magnético actual de los imanes permanentes libres de tierras raras. La simulación de estos sistemas constituye la segunda parte de esta tesis doctoral. Los sistemas específicos se han elegido en el contexto del apoyo a los esfuerzos experimentales en el marco del proyecto Amphibian, y son representativos de imanes permanentes bicomponentes nanoestructurados que combinan imanes duros y blandos. En particular, exploramos la capacidad de los cationes de Zn sustitutivos en el $NiFe_2O_4$ para aumentar la magnetización de este imán blando, analizando diferentes concentraciones y distribuciones de dopante a nivel atómico. Nuestros resultados ponen límites al éxito de este procedimiento para aumentar la magnetización, debido a la tendencia de los átomos de Zn a distribuirse en sitios tanto tetraédricos como octaédricos. También analizamos la contribución de los efectos de intercara al magnetismo de nanoestructuras bicomponentes blandas/duras basadas en $CoFe_2O_4$, $NiFe_2O_4$ y $MnFe_2O_4$. Nuestros resultados identifican el equilibrio entre las formas de espinela inversa y directa como la característica más importante para el rendimiento magnético de estos materiales, identificando algunos de los aspectos relevantes que influyen en este equilibrio. Además, desde el punto de vista teórico, demostramos el papel fundamental de la localización de los electrones gobernada por el término U local de Hubbard. Además de su conocido papel en las propiedades electrónicas y en la definición del "gap" electrónico, también es crucial para determinar las propiedades estructurales que rigen el rendimiento magnético de estas ferritas. Por último, demostramos que, aunque la mayoría de las propiedades magnéticas globales en el sistema bicomponente corresponden a la suma de las contribuciones individuales de los óxidos implicados, la intercara introduce redistribuciones y modificaciones locales relevantes.

Chapter 1

Introduction

Permanent magnets

Permanent magnets (PMs) are materials that are able to retain their magnetic properties after exposed to an external magnetic field. They are widely used in nowadays technologies including commercial applications such as computers, speakers, microphones, sensors, automobiles or household electronics (air conditioners, washing machines), among many others, and industrial applications including energy conversion and transportation. Recently emerging applications of PMs are found in areas such as electric vehicles, wind turbines, memory devices, magnetic levitation transportation, and biomedical tools [1, 2, 3, 4]. PMs are *necessary* for these applications, meaning they cannot be replaced by any other material, and thus they are regarded as *essential*. The first discovered permanent magnet, and the only one found in nature, is magnetite (Fe_3O_4), known for millennia by people in Sumeria, ancient Greece, China and pre-Colombian America. In fact, the word *magnet* may come from *"magnetis lithos"*, meaning "stone from Magnesia", a region in Anatolia. These civilizations used suspended magnetite as compasses in navigation. Since then, many other types of permanent magnets have been engineered. To compare them, we use the figure of merit of permanent magnets, the maximum energy product $(BH)_{max}$, which provides an estimation of the maximum energy than can be stored in the magnet. Figure 1.1 shows the evolution in time of the $(BH)_{max}$ for the different permanent magnets. In the 1960s, the discovery of the so called rare-earth PMs, compounds containing transition metals (TMs) and rare earths, revolutionized the PM market as $(BH)_{max}$ exceeded by up to 5 times the values of the materials known up to that time: carbon steels, ferrites or alnicos. Since then, one of the rare earths PMs, the neodymium magnet ($Nd_2Fe_{14}B$), holds the title of the commercially-available permanent magnet with the strongest

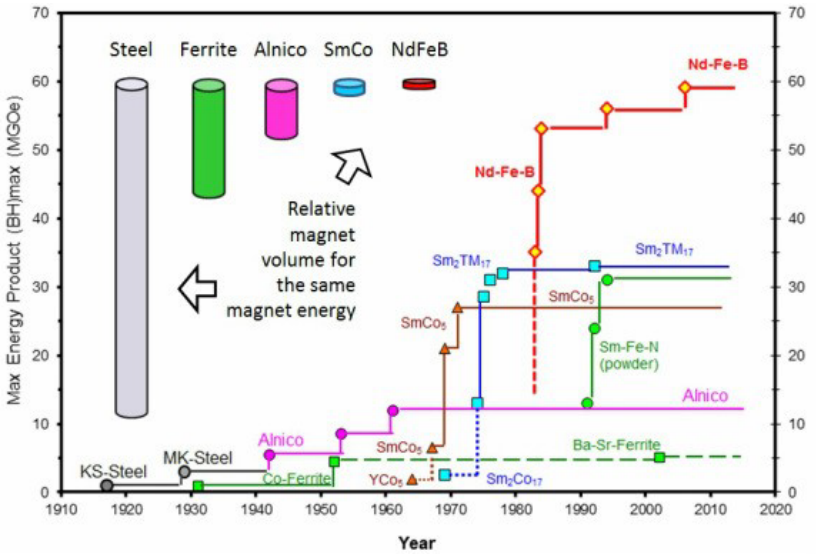

Figure 1.1: Progress in the energy product $(BH)_{max}$ improvement of permanent magnets in the last 100 years [5].

magnetic properties.

However, rare earths elements including Nd, Sm, Dy and Tb, and the associated permanent magnets, are very expensive as compared to other PMs. Hence, it is not surprising that, by weight, ferrites constitute close to 90% of the total global production of magnetic materials [1]. Besides, in the last decade, the vast majority of the production of rare earth permanent magnets has been situated in China, which in turn controls the supply of such strategic materials. An essential material that has a risk of supply disruption is considered a *critical* material [6]. Rare earths are thus classified within this group, as seen in the EU report about *critical* materials [7] and in similar reports of other regions and countries. There are three major ways to tackle the problem of supply shortage, *viz.* source diversification, improving the stewardship and *material substitution*. The latter implies identifying the specific utilization of a certain material and search for new ones exhibiting similar sought properties. Within this spirit, and in order to tackle the rare-earth supply shortage, the EU has funded several projects aimed at obtaining rare-earth free ferrite-based permanent magnets, including AMPHIBIAN (Anisometric permanent hybrid magnets based on inexpensive and non-critical materials), a project that formed part of the research and innovation funding programm Horizon2020, and where this work is framed. The use of ferrites is not fortuitous: even though they show weaker magnetic properties as compared to rare-earths PMs, they are still interesting due to their low production cost

and large abundance, together with their resistance to corrosion, their stability under extreme conditions and their low eddy current losses. Within the ferrite family, there exist two types depending on its structure: M-, W-, X-, Y-type hexagonal ferrites, usually named *hexaferrites*, and direct (or often called normal) and inverse *spinel ferrites* (magnetite lies within this group). In this work we study several spinel ferrites and the M-type Sr hexaferrite, a detailed analysis of their structure given at their respective chapters.

Bicomponent PMs

As mentioned before, permanent magnets strength is usually measured by its *maximum energy product*, which is derived from the magnetic hysteresis saturation loop (B-H curve). This parameter ultimately depends on the saturation magnetic polarization (M_s), related to the remanent magnetization (B_r), and the coercivity (H_c), which in turn originates from the magnetic anisotropy. Proper definitions of these two parameters must be introduced: B_r is the magnetization left behind after an external magnetic field is removed, while H_c is the field required to demagnetize the sample from a saturated state. Depending on these two parameters, a magnet can be classified as: *soft*, with large saturation magnetization and low coercivity; or *hard*, with low saturation magnetization and high coercivity. The combination of hard and soft magnetic materials enables interesting applications in a wide diversity of areas: not only for permanent magnets, but also for magnetic recording media, microwave absorption, ferrofluids or biomedical solutions [8, 9, 10, 11]. Combining hard and soft magnets is intended to retain the high saturation magnetization of the soft material and the high coercivity of the hard one, to overcome the maximum energy product of the individual counterparts, as seen in Figure 1.2.

The origin of this area can be traced back to a publication by Kneller and Hawig [13] where they predicted the existence of the exchange-spring magnets, and one publication by Skomski and Coey [14] where they found a combination (still using 5% of rare-earth elements) whose energy product was expected to reach 1MJ/m^3, which is larger than that of the neodymium magnets, that are about 445kJ/m^3 [15]. Even though it is not realistic to think that a combination of soft and hard rare-earth free *ferrites* would lead to such strong permanent magnets, an improvement over the current ferrite-based permanent magnets is expected, thus reducing the market dependence on rare-earth production. Different studies indicate that it is possible to fabricate nanostructures where this goal is achieved [9, 16, 17, 18], even though the details of the preparation procedure that determine the shape, size and morphology of the nanostructures are crucial. In addition to the preparation

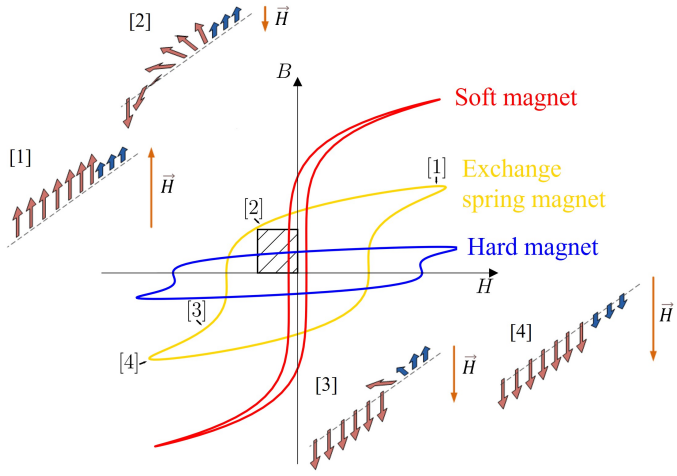

Figure 1.2: Schematic representation of the hysteresis loop of a *hard* magnet (blue), *soft* magnet (red) and a combined system (gold). The black square represents the maximum energy product $(BH)_{max}$ of the exchange spring magnet. The curves follow the parametric equations in [12]. [1], [2], [3] and [4] situations are schematically represented by blue and red arrows standing for magnetic moments of the hard and soft phase, respectively.

details, others at the interface between both materials (structural quality, lattice matching, strain, magnetic coupling between components) play an important role in the final properties of the system. From an experimental point of view, access to the interface properties is difficult, and often failure in the magnetic response emerges from defects at the interface. However, there are hints that complex interface interactions can be tuned to control the measured magnetic response of composite nanoparticles [19]. Opposite to experiments, first principles models are suitable to access to interfaces, and to explore both ordered and defected ones. To do so, it is important to understand the magnetic properties at the microscopic level, and how they are connected to magnetism at the macroscopic scale.

Fundamental microscopic magnetic properties

Ferrites are ferrimagnetic materials, with opposing magnetic moments (MMs) of the cations, as in antiferromagnets, but with a not-null total magnetization due to an unequal number or magnitude of *up*/*down* MMs. First principles calculations at the atomic level allow to understand how this arises. Magnetism is an inherently quantum mechanical effect, and trying to describe

it classically by means of the magnetostatic interaction of dipoles leads to energies of the order of 0.05 meV and a corresponding temperature of less than 1 K [20]. The experimental evidences of magnetic ordering persisting up to much higher temperatures (*e.g.* magnetite till about 860K) suggest that magnetism must have its origin in another interaction. Indeed, it is the interplay between the combination of Pauli principle with the Coulomb repulsion (*Coulomb exchange*) and the hopping of electrons (*kinetic exchange*) that leads to an effective coupling between the magnetic moments in a solid. To understand the origin of magnetism in ferrites, we first need to understand these two exchange mechanisms.

The idea behind the Coulomb exchange is quite simple: as the many-body fermionic wave function is antisymmetric, the electrons of like spin tend to avoid each other (Pauli principle), thus the probability of finding them close to each other is lower than the probability of finding electrons with opposite spins (exchange hole). Hence, the Coulomb repulsion depends on the spin by means of this effective interaction and spins with same direction tend to be energetically favorable. This is the basis of Hund's first rule: "For a given electron configuration, the term with maximum multiplicity has the lowest energy". In order to understand the mechanism of this Coulomb exchange let's consider a simple two-electron model. Solving the non-interacting hamiltonian H_0 gives the one-electron eigenstates $\psi_\alpha(\vec{r})$ and eigenvalues ϵ_α. Considering two orbitals $\alpha = a, b$, the two-electron Slater determinant with spins σ and σ' is

$$\Psi_{a,\sigma;b,\sigma'}(\vec{r}_1, s_1; \vec{r}_2, s_2) = \frac{1}{\sqrt{2}} \left(\psi_a(\vec{r}_1)\psi_b(\vec{r}_2)\sigma(s_1)\sigma'(s_2) - \psi_b(\vec{r}_1)\psi_a(\vec{r}_2)\sigma'(s_1)\sigma(s_2)\right) \tag{1.1}$$

leading to the degenerate eigenstates of H_0 with eigenvalues $\epsilon_a + \epsilon_b$. The manifestly spin-independent Coulomb repulsion,

$$H_U = \sum_{i<j} \frac{1}{|\vec{r}_i - \vec{r}_j|} \tag{1.2}$$

in the basis of states $\Psi_{\uparrow\uparrow}$, $\Psi_{\uparrow\downarrow}$, $\Psi_{\downarrow\uparrow}$ and $\Psi_{\downarrow\downarrow}$ takes the form:

$$H_U = \begin{pmatrix} U_{ab} - J_{ab} & 0 & 0 & 0 \\ 0 & U_{ab} & -J_{ab} & 0 \\ 0 & -J_{ab} & U_{ab} & 0 \\ 0 & 0 & 0 & U_{ab} - J_{ab} \end{pmatrix} \tag{1.3}$$

where U_{ab} and J_{ab} are the Coulomb and the exchange integral respectively:

$$\begin{aligned} U_{ab} &= \int d^3r_1 \int d^3r_2 \frac{|\psi_a(\vec{r}_1)|^2 |\psi_b(\vec{r}_1)|^2}{|\vec{r}_1 - \vec{r}_2|} \\ J_{ab} &= \int d^3r_1 \int d^3r_2 \frac{\psi_a^*(\vec{r}_1)\psi_b(\vec{r}_1)\psi_b^*(\vec{r}_2)\psi_a(\vec{r}_2)}{|\vec{r}_1 - \vec{r}_2|} \end{aligned} \tag{1.4}$$

The triplet states $\Psi_{\uparrow\uparrow}$ and $\Psi_{\downarrow\downarrow}$ are clearly eigenstates of H_U with an eigenenergy $\Delta\epsilon_{triplet} = U_{ab} - J_{ab}$ above H_0 eigenenergy. The third triplet state $(\Psi_{\uparrow\downarrow} + \Psi_{\downarrow\uparrow})/\sqrt{2}$ is obtained from diagonalizing the 2×2 submatrix, finding also the singlet state $(\Psi_{\uparrow\downarrow} - \Psi_{\downarrow\uparrow})/\sqrt{2}$ with eigenenergy $\Delta\epsilon_{singlet} = U_{ab} + J_{ab}$. As $J_{ab} > 0$ [20], we find that the triplet states are lower in energy than the singlet state by $2J_{ab}$. This is an example of the Hund's first rule, where the lowest state will have maximum spin. Hence, Coulomb exchange leads to favoring the alignment of spins.

When more than 1 atoms is involved, electrons can hop from one atom to the other. This is also modified by the Pauli principle, as electrons cannot hop to an orbital populated with an electron with the same spin, and by the Coulomb repulsion between the electrons. When electron hopping plays the main role in the exchange interaction, we speak of kinetic exchange. Consider the minimum molecular H_2 model with only 2 orbitals ψ_1 and ψ_2. When we introduce 2 electrons in the system, we can write the Hamiltonian in second quantization as:

$$\begin{aligned} H &= -t(c_{1\uparrow}^\dagger c_{2\uparrow} + c_{2\uparrow}^\dagger c_{1\uparrow} + c_{1\downarrow}^\dagger c_{2\downarrow} + c_{2\downarrow}^\dagger c_{1\downarrow}) + U(n_{1\uparrow}n_{1\downarrow} + n_{1\uparrow}n_{1\downarrow}) \\ &= -t\sum_{i,j,\sigma} c_{j\sigma}^\dagger c_{i\sigma} + U\sum_i n_{i\uparrow}n_{i\downarrow} \end{aligned} \tag{1.5}$$

where $-t$ is the energy gained by hopping onto the other orbital and U is the Coulomb repulsion of spins sharing the same orbital. Here, we have set the Coulomb exchange (Coulomb repulsion of spins in different orbitals) to zero, so we can isolate the kinetic exchange. Following the downfolding technique, based on partitioning the Hilbert space into the part of interest (the low-energy covalent states) and the states to be projected out (the high-energy ionic states), we find an effective Hamiltonian [20]:

$$H_{eff} = \frac{4t^2}{U}(\vec{S}_1 \cdot \vec{S}_2 - \frac{n_1 n_2}{4}) \tag{1.6}$$

where the spin operators are:

$$S_i^x = \frac{1}{2}(c_{i\uparrow}^\dagger c_{i\downarrow} + c_{i\downarrow}^\dagger c_{i\uparrow}) \ , \ S_i^y = -\frac{i}{2}(c_{i\uparrow}^\dagger c_{i\downarrow} - c_{i\downarrow}^\dagger c_{i\uparrow}) \ , \ S_i^z = \frac{1}{2}(n_{i\uparrow} - n_{i\downarrow}) \tag{1.7}$$

As $J = \frac{4t^2}{U} > 0$, the antiparallel spin states are lower in energy. Hence, kinetic exchange favors antiferromagnetism. When two neighboring atoms are interacting by this mechanism, we speak of *direct exchange*. When both exchange mechanisms (Coulomb and kinetic) are in play, we speak of *double exchange*. All these mechanisms are merely idealizations of a much more realistic description of the interactions in a solid.

However, direct exchange cannot explain the antiferromagnetism found in ferrites: the d-orbitals of transition metal ions are very localized, and hopping between atoms can only occur if they are very close to each other. In ferrites, transition-metals are separated by oxygen ions, preventing electrons to hop from one to another. Instead, hopping via the intermediate oxygen is found in which is called *superexchange mechanism*. As seen in Figure 1.3, depending on the angle formed by the TM-O-TM geometry, a different superexchange is taking place: while the 180° angle leads to a fundamentally kinetic exchange where the TM d-orbitals are coupled to the same oxygen p-orbital, the 90° angle leads to double exchange in which hopping between the two implied oxygen orbitals is not permitted and Coulomb exchange arises. Following the downfolding technique explained before, these two situations lead to exchange couplings of the form [20]:

$$J = \frac{4t_{pd}^4}{(U_d + \Delta_{pd})^2}\left(\frac{1}{U_d} + \frac{1}{U_d + \Delta_{pd}}\right) \tag{1.8}$$

and

$$J = -\frac{4t_{pd}^4}{(U_d + \Delta_{pd})^2}\frac{2J_{xy}}{4(U_d + \Delta_{pd})^2 - J_{xy}^2} \tag{1.9}$$

respectively, where ϵ_d and ϵ_p are the energy of one electron in the d or p orbital respectively, t_{pd} is the hopping between p and d-orbitals, U_d is the Coulomb repulsion between electrons at the same d-orbital, and $\Delta_{pd} = \epsilon_d - \epsilon_p$. From these two expressions follow that the 180° situation leads to antiferromagnetism while the 90° geometry leads to ferromagnetism. The former can be understood as a more complex direct exchange involving four hopping processes, and the latter can be understood by a combination of the kinetic exchange between the TMs and the oxygen, and the Hund's first rule operating at the oxygen p_x and p_y orbitals, that favors the alignment of oxygen spins and, hence, it favors antisymmetric d spins, as seen in Figure 1.4. This matches the Goodenough-Kanamori-Anderson (GKA) rules [21, 22] (specifically for partially filled d orbitals, which is the case in TM ferrites), a set of semi-empirical rules proposed to rationalize the magnetic properties of materials where the superexchange mechanism is involved. Indeed, the ferromagnetic/antiferromagnetic interaction between atoms in ferrites can

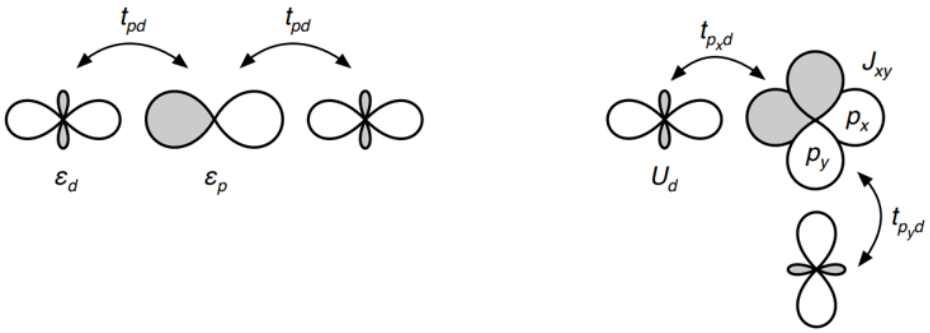

Figure 1.3: Schematic representation of the two types of superexchange mechanisms. On one hand, when the TM-O-TM forms a 180° angle (left) both d-orbitals couple to the same p-orbital of the oxygen. On the other hand, a 90° geometry prevents hopping of electrons from the p_x orbital to the p_y, and the superexchange is mediated by the Coulomb exchange. The energy of one electron at $d(p)$-orbital is ϵ_d (ϵ_p), and the hopping and Coulomb exchange energies are t_{pd} and J_{xy}, respectively. This figure is extracted from [20].

be accurately explained by these geometrical considerations, which depend on the specific structure (hexagonal or spinel).

The equations 1.8 and 1.9 allow to picture the mechanisms involved in the exchange interactions present in ferrites. However, they fail to provide a way to estimate the exchange constants implied in these interactions, as we do not know values for t_{dp}, U_d or J_{xy}. As we will show in detail in Chapter 2, Density Functional Theory (DFT), the first-principles method used in this work, allows to extract these exchange constants by mapping the total energy of the structure to a microscopic model of the interactions: the Heisenberg model. This model includes only the dipole interaction between spins, without resorting to high rank multipoles that have been proved to be relevant fir highly correlated weak magnets [23]. As we will show, the feasibility of reproducing reasonable exchange couplings that account for the magnetic behavior of ferrites without resorting to such multipoles indicates that Heisenberg model contains the relevant interactions.

Within a multi-scale spirit, we use our DFT results, including the exchange coupling values, as inputs for micromagnetic models that can provide estimates, of among other properties, magnetic transition temperatures of these materials. Multi-scale modeling is particularly interesting as it allows predictions of material properties occurring at different length scales, and ultimately based on first-principles considerations. An in-depth description of the multi-scale methods used in this work is given in Chapter 2.

Though the focus of this thesis is the description of the magnetic proper-

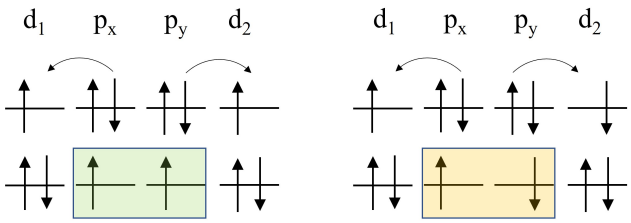

Figure 1.4: Schematic picture of the 90° superexchange mechanism. At left (right), aligned (opposite) d_1 and d_2 spins lead to aligned (opposite) p_x and p_y spins. Due to Hund's first rule, left situation is favored.

ties of the ferrite systems considered, the DFT formalism provides in addition an accurate description of their electronic and structural properties. Our work is pioneer on the description based on DFT of SFO and bicomponent systems combining two cubic ferrites. In particular, for the case of SFO, we will show that the magnetic properties can be exploited to refine our choice of the Hubbard strength.

This document is organized as follows: all the theoretical aspects of the models used in this thesis are provided in Chapter 2, where we describe in detail the basis of Density Functional Theory and other formalisms used to extract specific properties. Here, we also describe the Heisenberg model used to calculate exchange coupling constants, and the Generalized Molecular Field Theory and the Monte-Carlo methods used to estimate transition temperatures. In Chapter 3, we study the structural, electronic and magnetic properties of the SFO hexaferrite, paying special attention to obtain values for relevant calculation parameters that describe correctly atomic and, within a multi-scale spirit, microscopic properties simultaneously. Chapter 4 covers the study of the bulk Co-, Ni-, Mn- and Zn- spinel ferrites, where the conditions of the calculations have been exhaustively examined in order to provide an accurate framework to further investigate interfaces and defects. The ideal interface formed by cobalt and nickel spinel ferrites is studied in Chapter 5, evaluating its magnetic properties under different interface orientations and providing a departing point to investigate more realistic interfaces. The non-ideal interface formed by cobalt and manganese ferrite is studied in Chapter 6. Here, due to the mismatch between both ferrites, strain effects are considered, forcing us to examine different ionic distribution within the structure. In Chapter 7, we revisit the substitution of Ni by Zn at NFO with special attention to the influence of the Zn d band localization on the degree of inversion, the electronic structure and the magnetic properties. Lastly, in Chapter 8, we outline the main conclusion of this work.

Chapter 2

Theoretical Methods

In this chapter we will describe in detail the theoretical methods used in the calculations that have been carried out along this thesis. We outline the main aspects of Density Functional Theory (DFT), the core method of this work, and other additional formalisms used to evaluate specific properties. Details inherent to the implementation of DFT on the different computational packages used in this work, VASP and SIESTA, will also be described in this chapter.

2.1 Density Functional Theory

A system of interacting electrons and nuclei can be approximately described by the wave function satisfying the non-relativistic Schrödinger equation:

$$i\frac{\partial}{\partial t}\Psi(\mathbf{r},t) = \hat{H}\Psi(\mathbf{r},t) \tag{2.1}$$

where $\hat{H} = \hat{T}+\hat{V}$ is the non-relativistic Hamiltonian, with $\hat{T}$ and $\hat{V}$ being the kinetic and potential parts respectively. Specifically, static situations lead to a time-independent version of this expression:

$$i\frac{\partial}{\partial t}\Psi(\mathbf{r}) = \hat{H}\Psi(\mathbf{r}) \tag{2.2}$$

with a Hamiltonian:

$$\hat{H} = \hat{T}_N + \hat{T}_e + \hat{V}_{NN} + \hat{V}_{Ne} + \hat{V}_{ee} \tag{2.3}$$

where $\hat{T}$ represents the kinetic energy of the nuclei (N) and the system of electrons (e) and $\hat{V}$ the nucleus-nucleus (NN), nucleus-electron (Ne) and electron-electron (ee) potential energy. Historically, several approximations

have been made to try to solve this equation. The first one was introduced by Born and Oppenheimer, who noticed that the motion of electrons and nuclei could be separated due to the huge difference in mass of these particles [24]. The wave function can then be splitted:

$$\Psi(\mathbf{r}) = \Psi(\mathbf{r_A})\phi(\mathbf{r}) \tag{2.4}$$

where Ψ and ϕ represent the nuclei and electrons wave function respectively. The Hamiltonian can then be expressed as the sum of purely electronic $\hat{H}_e$ and nuclear parts:

$$\begin{aligned} \hat{H} &= \hat{H}_e + \hat{T}_N + \hat{V}_{NN} \\ \hat{H}_e &= \hat{T}_e + \hat{V}_{Ne} + \hat{V}_{ee} \end{aligned} \tag{2.5}$$

The term $\hat{V}_{Ne}$ can be treated as an external potential in which the electrons are embedded. However, the electron-electron interaction term $\hat{V}_{ee} = \frac{1}{|\mathbf{r}_a - \mathbf{r}_b|}$ makes this equation only solvable for systems made of few particles. For larger systems, further approximations must be made. Different *ab-initio* methods have been developed to solve this stationary equation of the electrons as the Hartree-Fock (HF) method or Density Functional Theory (DFT). While HF tries to obtain the anti-symmetric wave function of the electrons using Slater determinants, DFT focuses on the electronic density. The main advantage of the latter is that the number of dimensions is reduced from $3N$ (or $4N$ if spin is considered) to only 3, which makes it computationally much more efficient.

The $\hat{H}_e$ term couples the electronic and nuclear parts, ultimately allowing the evaluation of how the nuclei positions influence the electronic wavefunction through the Hellmann-Feynman theorem. This theorem states that for any parameter λ [25]:

$$\frac{dE_\lambda}{d\lambda} = \langle \psi_\lambda | \frac{d\hat{H}_\lambda}{d\lambda} | \psi_\lambda \rangle \tag{2.6}$$

As the coordinates of the nuclei are parameters of the Hamiltonian, an expression for the force arises for $\lambda = R$. However, this expression is not valid when the wavefunctions are not a complete basis set or when they depend explicitly on the nuclei positions. In these cases, additional forces emerge known as Pulay forces.

2.1.1 Hohenberg-Kohn (HK) approach

The wave function in quantum mechanics is defined in a way that contains all the information of the system. Hohenberg and Kohn, based on the work of Thomas and Fermi [26, 27], showed that all this information is also contained

in the electronic density [28]. They stated two theorems: the first one says that the external potential is uniquely determined by the electron density $\rho(\mathbf{r})$, which implies that the state and all properties of the system are defined by this function. The second one defined an energy functional:

$$E[\rho, V_{ext}] = \int d\mathbf{r} V_{ext}(\mathbf{r})\rho(\mathbf{r}) + F_{HK}[\rho] \tag{2.7}$$

with

$$F_{HK}[\rho] = T[\rho(\mathbf{r})] + V_{e-e}[\rho(\mathbf{r})] \tag{2.8}$$

and stated that the energy of the system is variational with respect to the density $E_0[\rho_0(\mathbf{r})] < E_0[\rho(\mathbf{r})]$, and hence the groundstate density would be the one that minimizes this energy functional. The only problem left was to find the electronic density that, precisely, minimizes the energy of the system.

2.1.2 Kohn-Sham (KS) method

The Kohn-Sham method is based on approximating the electronic density of the interacting particles by an electronic density of a system of non-interacting particles in an effective potential generated by the nuclei and the rest of the electrons [29]. They defined an energy functional:

$$E[\rho, V_{ext}] = \int d\mathbf{r} V_{ext}(\mathbf{r})\rho(\mathbf{r}) + F[\rho] \tag{2.9}$$

where the functional $F[\rho]$ is "universal" in the sense that it is independent of the external potential. They also defined this term as:

$$F[\rho] = T_s[\rho] + \frac{1}{2}\int d\mathbf{r}\rho(\mathbf{r})V_C(\mathbf{r}) + E_{xc}[\rho] \tag{2.10}$$

The first term of the right-hand side is not the real kinetic energy, but the kinetic energy that a non-interacting electrons system would have, and can be described with single-particle orbitals:

$$T_s[\rho] = \sum_{i=1}^{N}\int d\mathbf{r}\phi_i^*(\mathbf{r})\left(-\frac{1}{2}\nabla^2\right)\phi_i(\mathbf{r}) \tag{2.11}$$

The second and third terms in equation 2.10 describe the electron-electron interaction, with V_C the classical Coulomb potential and E_{xc} referring to the exchange and correlation energy. Provided a definition of the Exchange-Correlation (XC) term, the way of finding the electronic density for a given

system is by means of a self-consistent procedure. First, we solve the non-interacting Schrödinger equation:

$$[-\frac{1}{2}\nabla^2 + V(\mathbf{r})]\phi_i(\mathbf{r}) = \epsilon_i\phi_i(\mathbf{r}) \tag{2.12}$$

where the functions ϕ_i are the Kohn-Sham orbitals. Then, we can compute the electronic density defined by the Slater determinant:

$$\rho(\mathbf{r}) = \sum_{i=1}^{N} f_i|\phi_i(\mathbf{r})|^2 \tag{2.13}$$

The occupation numbers f_i are defined as the Fermi-Dirac occupancies. Then, we update the potential $V(\mathbf{r})$ with the new value of ρ:

$$V(\mathbf{r}) = V_{ext}(\mathbf{r}) + V_C(\mathbf{r}) + \frac{\delta E_{xc}[\rho]}{\delta\rho(\mathbf{r})} \tag{2.14}$$

and we use this new value in 2.9, finding new Kohn-Sham orbitals, and so on, until we reach a self-consistent requirement. Until this point, apart from the non-relativistic and the Born-Oppenheimer approximations, this procedure guarantees an exact solution. However, the functional form of the XC interaction is unknown, and some approximations are needed.

2.1.3 Approximations to the XC energy

Kohn and Sham also proposed an approximation for the exchange-correlation part, known as the local density approximation (LDA), which takes the form [29]:

$$E_{xc}^{LDA}[\rho] = \int d\mathbf{r}\rho(\mathbf{r})\epsilon_{xc}[\rho(\mathbf{r})] \tag{2.15}$$

where ϵ_{xc} is the exchange-correlation energy of a single electron in a homogeneous electron gas with density ρ. There are also generalizations to spin-polarized systems [30, 31] called local spin density approximation (LSDA) using the exchange-correlation energy of a homogeneous, spin-polarized electron gas $\epsilon_{xc}[\rho_\uparrow(\mathbf{r}), \rho_\downarrow(\mathbf{r})]$. This approximation is good only if the density of the system is nearly constant or at very high densities where the kinetic energy dominates the exchange-correlation term [32]. Hence, they did not expect it to correctly describe condensed matter bonding.

In order to account for rapid changes in electron density, extensions to this approximation were done introducing gradient expansions of the exchange-correlation energy [28]. Taking only the second-order term, this energy reads:

$$E_{xc}^{GGA}[\rho_\uparrow, \rho_\downarrow] = \int d\mathbf{r}\rho(\mathbf{r})\epsilon_{xc}[\rho_\uparrow, \rho_\downarrow, \nabla\rho_\uparrow, \nabla\rho_\downarrow] \tag{2.16}$$

This is called generalized gradient approximation (GGA). There are many ways to construct a GGA functional as there are many ways to construct ϵ_{xc}, and also different ways to do the cut-off needed to get rid of the spurious long-range parts of the exchange-correlation hole function. Two examples are the Perdew-Burke-Ernzerhof (PBE) functional [33], in which all parameters are fundamental constants, and a further modification (PBEsol) [34], which differs only in two parameters from PBE and which is designed and proved to accurately describe equilibrium properties of many densely-packed solids. In this work we will based mainly on PBEsol, although we systematically perform preliminary studies using different exchange-correlation functionals to guarantee that general structural and electronic properties of the system do not depend on our particular choice. However, as we demonstrate for ZFO in section 4.3 and ZNFO in section 7, no parametrization of the GGA functional is universally valid, and care should be taken in this choice.

Higher order expansions of the exchange-correlation energy have been developed leading to what is known as meta-GGA approximations. However, all of them fail in describing highly correlated systems. Further approaches called hybrid functionals combine Hartree-Fock formalism and DFT in an attempt to incorporate exact exchange. The weights used for each part of the functional are set to satisfy different empirical values, and many different functionals have been constructed using different criteria such as B3LYP or HSE. Sadly, introducing Hartree-Fock exact exchange leads to a huge computational cost, which constitutes a drawback to describe large unit cells and complex systems.

DFT+U

For some systems, called Mott insulators, the electronic localization is responsible for the creation of a band gap at the Fermi level. An attempt to describe these Mott insulators was made by Hubbard in what is called the Hubbard model, where the Hamiltonian is defined as:

$$H = -t\sum_{i,\sigma}\left(\hat{c}_{i,\sigma}^\dagger\hat{c}_{i+1,\sigma} + \hat{c}_{i+1,\sigma}^\dagger\hat{c}_{i,\sigma}\right) + U\sum_i \hat{n}_{i\uparrow}\hat{n}_{i\downarrow} \tag{2.17}$$

where the first term accounts for the energy of hopping electrons and the second term for the on-site Coulomb interaction which ultimately represents the electron repulsion. Here, $\hat{c}$ and $\hat{c}^\dagger$ are the annihilation and creation operators respectively, $\hat{n} = \hat{c}^\dagger\hat{c}$ is the density operator and i runs over the valence

electrons d and f only. Following Hubbard's idea, the electronic localization can be efficiently incorporated in DFT in which is called DFT+U method by the definition of a new XC-functional that includes this localization, which ultimately requires a redefinition of all terms. Specifically, in L(S)DA+U this translates into the introduction of an additional Hubbard-like term in the Hamiltonian with two parameters: the on-site Coulomb parameter U and the site exchange parameter J. The total energy of the system resulting from the summation of the L(S)DA energy $E_{L(S)DA}$ and the Hubbard-like energy E_{Hub} leads to a double-counting error which is corrected by the substraction of an additional "double-counting" (dc) term E_{dc}:

$$E_{DFT+U}[\rho] = E_{DFT}[\rho] + E_{Hub}[\rho] - E_{dc}$$

There are several ways to incorporate this idea, but the one we use in this thesis is the simplified rotationally invariant approach to L(S)DA+U introduced by Dudarev *et al* [35]:

$$E_{DFT+U} = E_{DFT} + \frac{U-J}{2} \sum_{\sigma} \left[\left(\sum_{m1} \hat{n}^{\sigma}_{m1,m1} \right) - \left(\sum_{m1,m2} \hat{n}^{\sigma}_{m1,m2} \hat{n}^{\sigma}_{m2,m1} \right) \right]$$

This is, a penalty functional term is added to the DFT total energy which forces the valence levels to be either fully occupied or fully unoccupied. In Dudarev's approach, only the difference $U - J$ is meaningful, so there is only one parameter in the model. We should also mention that we use Dudarev's approach in all the calculations, and that we use U to refer to the difference $U - J$. The main drawback of this method is that it introduces a parameter in an otherwise *ab-initio* method. There are *ab-initio* approaches to extract values of U and J, *e.g.* the constraint random-phase approximation (cRPA) [36]. However, they are computationally demanding, and often provide values that do not result in band gaps close to the experiments. As a practical alternative, the most usual way to determine U, J (or U-J) is to select target features, and to compare the DFT+U and experimental values for them, choosing this way the best U, J as that describing most features accurately. This is the approach we use throughout this work.

2.2 Basis sets

The Kohn-Sham method, which implies solving a series of single-particle Schrödinger equations, requires to choose a basis set to describe the wave-functions. There are different basis sets in which the single-electron wave functions can be expanded on, and all of them have some advantages and

disadvantages with respect to the others. They can be classified in three different families: atomic spheres, localized basis sets and planes waves.

2.2.1 Types of basic sets

2.2.1.a Atomic Spheres

The main idea behind the Atomic Spheres method is to split the space in two kind of regions: the ones around the atoms, where the potential is strong and thus is dominated by atomic-like features, and some interstitial regions where the potential is much slower and can be represented by plane waves. Thus, the wave functions are made by the combination of atomic-like orbitals and plane waves:

$$\psi_{i,\mathbf{k}}(\mathbf{r}) = \sum_m c_{i,m}(\mathbf{k})\chi_{\mathbf{k}+\mathbf{G}_m}(\mathbf{r})$$

$$\chi_{\mathbf{k}+\mathbf{G}_m}(\mathbf{r}) = \left\{ \begin{array}{cc} e^{i(\mathbf{k}+\mathbf{G}_m)\cdot\mathbf{r}} & r > S, \\ \sum_L C_L(\mathbf{k}+\mathbf{G}_m)\psi_L(\epsilon,\mathbf{r}) & r < S \end{array} \right\} \tag{2.18}$$

Within this family, we can find Augmented Plane Waves (APW) and Muffin Tin orbitals (MTO).

2.2.1.b Plane Waves

The use of plane waves arises naturally since they are the eigenfunctions of the homogeneous electron gas. They are also a good choice for systems with 3-dimensional periodic boundary conditions such as solids, which impose translational invariance through the Bloch theorem, leading to a single particle wavefunction of the form:

$$\psi_{n,\mathbf{k}} = \frac{1}{\Omega}\sum_{\mathbf{G}} c_{\mathbf{G},n,\mathbf{k}} e^{i(\mathbf{G}+\mathbf{k})\cdot\mathbf{r}} \tag{2.19}$$

Integrating over the entire Brillouin zone and summing over the filled bands, we recover the charge density:

$$\rho(\mathbf{r}) = \sum_n^{\infty} \int d^3\mathbf{k} f_{n,\mathbf{k}} \psi_{n,\mathbf{k}}(\mathbf{r})\psi^*_{n,\mathbf{k}}(\mathbf{r}) \tag{2.20}$$

where

$$f_{n,\mathbf{k}} = \frac{1}{1+\exp(\beta(\epsilon_{n,\mathbf{k}} - \epsilon_f))} \tag{2.21}$$

are the Fermi weights. Theoretically, an infinite number of plane waves is required to form a complete basis set. In practice this cannot be accomplished

for numerical reasons and the need to keep matrices at finite size, hence we restrict to a finite number of plane waves defined by an energy cutoff:

$$\frac{\hbar^2}{2m_e}|\mathbf{G}+\mathbf{k}|^2 < E_{cutoff} \tag{2.22}$$

All those plane waves with energy below that limit are included in the basis set. The use of plane waves is very convenient for several reasons:

- they are not biased by the nature of the system or the atoms that conform it
- their trivial independence on the atomic positions ease the evaluation of forces, which can be extracted straightforwardly from Hellmann-Feynman theorem
- some integrals can be efficiently calculated using fast Fourier transform (FFT) between real an reciprocal space
- plane waves basis set shows a smooth and monotonic convergence on the cutoff, as opposed to localized basis sets

On the other hand, there are several drawbacks of using plane waves as the basis set. In some particular problems, such as describing surfaces and computing some physical values as the work of separation at interfaces (which will be our object of study in chapters 5 and 6), we need to include a vacuum region in our unit cell in order to mimic the presence of the surface within 3D periodic boundary conditions. It turns out that vacuum is not efficiently described by plane waves, as the computational cost is the same as that used in describing matter. Besides, due to the nature of plane waves, they do not represent any physically meaningful function (as opposed to atomic orbitals), and in practice many plane waves are needed to achieve a good accuracy. This also implies a limitation of these basis sets to provide a localized atomic-like picture. There are several approaches to assign a charge to each atom, *e.g* projecting into spheres centered at each atomic site and integrating the charge density within those regions. However, in these approaches, the interstitial regions between those spheres are neglected. Instead, we rely on the Bader method [37], which efficiently considers all space by splitting it into regions around atoms defined by zero flux surfaces on which the charge density is minimum, and then associates the atomic charge and magnetic moment to the integrated charge and magnetic moment density, respectively, within those regions.

We should also mention that the integration in $\mathbf{k}$ over the entire Brillouin zone in Eq. 2.20 is not such in practice. Due to our finite computer resources,

this integral has to be transformed into a sum over a discrete set of k-points. Convergence in k-points must be studied in order to choose a sufficiently large set that ensures a certain desired precision of our calculations.

2.2.1.c Atomic orbitals

When the system is very large, the plane wave basis sets are not efficient, as the computational cost scales with N^3. In order to achieve a linear scaling, localized basis sets are employed. Atomic orbitals (AO) belong to this class. They are defined as:

$$\phi_{Ilmn}(\mathbf{r}) = R_{Iln}(|\mathbf{r}|)Y_{lm}(\mathbf{r}) \tag{2.23}$$

with R_{Iln} being the radial funtions and Y_{lm} the spherical harmonics. The radial functions are not uniquely determined, and several possibilities are found:

- Gaussian based. This is one very common option as there are very efficient libraries for treating with these functions. This is better suited to molecules.

- Slater-type orbitals. These are functions used as atomic orbitals that involve complex integrals usually resolved by semiempirical parametrizations.

- Numerical atomic orbitals (NAO). The radial functions are obtained from numerical solutions to the Kohn-Sham equations for the isolated pseudoatom. These are the ones used in SIESTA code.

In addition, different numbers of atomic orbitals per atom can be defined for the radial part. Depending on that, we refer to single-ζ (one radial orbital) or multiple-ζ (for multiple radial orbitals). In general, these basis sets provide an efficient mechanism to incorporate vacuum regions as opposed to plane waves basis sets, as the atomic interactions become zero at a certain distance. The evaluation of the atomic charge is also more straightforward and is calculated just by integrating the projected density of states (PDOS), which results in the charge associated to each orbital. The PDOS is just the projection of the density of states (DOS) on each orbital, the DOS being defined as the proportion of occupied states at each energy. This method of assigning local charges to the atoms is based on Mulliken population analysis, where Mulliken charges are obtained adding atomic orbital contributions on the same atom, and are strongly dependent on the basis set and the functional used.

2.2.2 Treatment of core electrons: pseudopotentials and PAW

In order to deal with the core electrons, Hellmann introduced the pseudopotential approximation, which replaces the atomic all-electron potential with an effective potential [38], as shown in Figure 2.1. The idea behind this method is to get rid of the rapidly oscillating full-electron wavefunction by a pseudo-wavefunction with fewer nodes that matches the full-electron wavefunction above certain cut-off radius $\mathbf{r_c}$, hence, making the use of a plane wave basis set much more feasible, and not affecting the chemical bondings as they are determined only by the valence part of the wavefunctions. This approach, though conceived using a plane wave basis set, can be extended to basis sets of different nature.

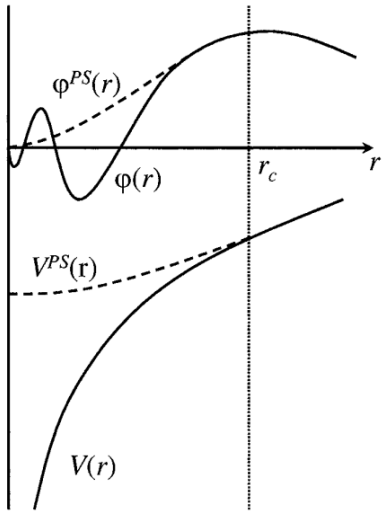

Figure 2.1: Schematic representation of the replacement of the real potential and wave function by a pseudopotential and pseudo-wave function.

A better approach that really takes into account the all-electron wavefunction is the Projector augmented wave method (PAW) introduced by Blöchl [39]. Following the idea of the pseudopotential approximation, this method consists in transforming the wave-function and all operators with a linear transformation that separates formally the smooth part and the rapidly oscillating part of the wave function at the core regions. This is the one used in the VASP code.

2.2.3 Green function methods

Though most of the work performed in this thesis is based on solving the DFT equations using wavefunctions, we should mention here alternative methods based on Green function approaches. These methods solve the equivalent Lippman-Schwinger equation, and we have used its implementation in the GREEN code, developed by J. Cerdá [40, 41], and interfaced to the SIESTA package, at our calculations in chapter 3.

Green function methods have the advantage to allow formulations not relying on 3D periodic boundary conditions (PBC), which becomes useful to describe problems involving surfaces or interfaces. Within the models based on 3D PBC, surfaces are modeled by introducing a finite vacuum region that defines the surface planes. This allows to describe satisfactorily certain surface properties, such as most local features (structure, local charges and moments) and properties such as the cohesive energy. But it fails to describe those electronic properties that rely on the correct identification of the loss of 3D PBC, such as surface states. To this end, it is necessary to model the surface as a truly semi-infinite system, in which the surface layers are connected to a semi-infinite bulk. Green function methods are particularly useful in this sense, as the 2D surface Green function can be expressed exactly in terms of the 3D Green function of the entire system. The drawback of these methods is the difficuty to implement the Hellman-Feynmann theorem, and their higher computational cost, that often prevents their application for complex systems or large unit cells.

2.3 Spin-orbit coupling (SOC)

In this thesis, we study soft and hard magnetic materials. This feature is ultimately determined by the magnetocrystalline anisotropy (MA), which is a fundamental property responsible of the high or low coercivity of materials. The MA has its origin in the spin-orbit coupling (SOC), that describes the interaction of the electronic orbital moment and the spin moment, and can be understood as the influence of the electric field arising from the nucleus. The MA is also affected by the crystal field, that is the electric field generated by the surrounding atoms on the spin. The implementation of SOC in the PAW method has been developed by Steiner *et al* at [42]. The one electron orbitals in PAW method are written as:

$$|\psi_n\rangle = |\tilde{\psi}_n\rangle + \sum_i (|\phi_i\rangle - |\tilde{\phi}_i\rangle) \langle \tilde{p}_i|\tilde{\psi}_n\rangle \tag{2.24}$$

where $|\tilde{\psi}_n\rangle$ are the pseudo orbitals and $|\phi_i\rangle$ and $|\tilde{\phi}_i\rangle$ the all-electron and pseudo partial waves respectively, which are only nonzero within the PAW spheres, and therefore $|\psi_n\rangle$ matches $|\tilde{\psi}_n\rangle$ in the interstitial regions. Within this method, a (semi)-local operator acting on $|\psi_n\rangle$ can be written by means of a pseudo operator $\tilde{O}$ acting on the pseudo orbitals $|\tilde{\psi}_n\rangle$:

$$\tilde{O} = O + \sum_{ij} |p_i\rangle \left(\langle\phi_i|O|\phi_j\rangle - \langle\tilde{\phi}_i|O|\tilde{\phi}_j\rangle\right) \langle p_j| \tag{2.25}$$

where $|p_i\rangle$ are the projector functions. The spin-orbit coupling mainly affects the region surrounding the nucleus, so it can be neglected outside the PAW spheres. Due to that and to the fact that, within PAW spheres, the pseudo partial waves $\tilde{\phi}_i$ form a complete basis set, the SOC Hamiltonian can be written as:

$$\tilde{H}_{SO} = \sum_{ij} |p_i\rangle \langle\phi_i|H_{SO}|\phi_j\rangle \langle p_j| \tag{2.26}$$

Given the form of H_{SO} as

$$H_{SO}^{\alpha\beta} = \frac{\hbar^2}{(2m_e c^2)} \frac{K(r)}{r} \frac{dV(r)}{dr} \vec{\sigma}^{\alpha\beta} \cdot \vec{L} \tag{2.27}$$

where $\vec{L} = \vec{r} \times \vec{p}$ is the angular momentum operator, $\vec{\sigma}$ are the (2×2) Pauli matrices, $V(r)$ is the spherical part within the PAW sphere of the effective all-electron potential, α and β the spin-up and spin-down component, and $K(r)$:

$$K(r) = \left(1 - \frac{V(r)}{2m_e c^2}\right)^{-2} \tag{2.28}$$

and using $\phi_i(\mathbf{r}) = R_i(|\mathbf{r}|)Y_{l_i m_i}(\mathbf{r})$, where R_i and $Y_{l_i m_i}$ are the radial part and the spherical harmonics respectively, we can write the pseudo Hamiltonian operator as:

$$\tilde{H}_{SO}^{\alpha\beta} = \frac{\hbar^2}{(2m_e c^2)} \sum_{ij} |\tilde{p}_i\rangle R_{ij} \vec{\sigma}_{\alpha\beta} \cdot \vec{L}_{ij} \langle\tilde{p}_j| \tag{2.29}$$

where

$$R_{ij} = 4\pi \int_0^{r_c} R_i(r) \frac{K(r)}{r} \frac{dV(r)}{dr} R_j(r) dr \tag{2.30}$$

with r_c a core radius outside of which $\tilde{\phi}_i$ are equivalent to ϕ_i. This SOC operator acting on the pseudo orbitals reads:

$$|\tilde{\psi}_n^{\alpha}\rangle = \sum_{\alpha\beta} \tilde{H}_{SO}^{\alpha\beta} |\tilde{\psi}_n^{\beta}\rangle \tag{2.31}$$

This method allows to describe non-collinear magnetism within the PAW method in VASP. We have employed two different procedures to extract the MA of our different materials, based on quantifying the MAE (magnetic anisotropy energy). On one side, by total energy difference of configurations with the magnetization forced to lie along certain high symmetry directions of the unit cell, on the other, by a step-wise canting of the magnetization following the magnetic constraints method [43] which adds a penalty energy to the total energy of the form:

$$E = E_0 + \sum_I \lambda \left(\vec{M}_I - \hat{M}_I^0 (\hat{M}_I^0 \cdot \vec{M}_I) \right)^2 \tag{2.32}$$

where E_0 is the DFT energy, I goes over all atomic sites, $\hat{M}_I^0$ and $\vec{M}_I$ are the desired and the actual direction of the magnetic moment of atom I, respectively.

In SIESTA, for those calculations including spin-orbit coupling, the fully relativistic pseudopotential (FR-PP) approach [44, 45] was used to construct the SOC Hamiltonian. MAEs and orbital magnetic moments were calculated self-consistently varying the spin quantizaton axis from the out-of-plane to in-plane direction, $\theta = 0°$ and $90°$, respectively. Additionally, an alternative estimation of the MAEs was obtained via the force theorem (FT) based on the difference in the non-self-consistent band energies between different spin quantization axis [46, 47].

2.4 Exchange constants

The total energy obtained from DFT calculations allows to extract the exchange coupling constants that can be used as input of larger scale models (atomistic, micromagnetic) or to estimate macroscopic properties such as the magnetic ordering temperature. To do so, we map the *ab-initio* energies of different magnetic configurations defined by different orientations of the spins of the atoms, to a Heisenberg Hamiltonian, whose exchange energy is written as:

$$E_\alpha = \frac{1}{2} \sum_{i,j}^{N} n_i z_{ij} J_{ij} \, \vec{S}_i^\alpha \cdot \vec{S}_j^\alpha \tag{2.33}$$

where n_i is the number of atoms in the i-th sublattice, z_{ij} the number of nearest neighbors to an i-th ion that belong to sublattice j, $\vec{S}_{i/j}^\alpha$ are the spin vectors of the ions in the i/j sublattice, with α being the specific magnetic configuration, and J_{ij} is the exchange coupling constant between atoms of

sublattices i and j. With this definition, $J_{ij} > 0$ ($J_{ij} < 0$) indicate an antiferromagnetic (ferromagnetic) interaction between atoms i and j. We should mention that E_α can also be defined with an overall minus sign, thus changing J by -J and reversing the previous analysis. Assuming that the modulus S_i of the spin vector $\vec{S}_i^\alpha$ of the i-th ions does not change between different spin configurations (that is, independent of α), we can rewrite it as:

$$E_\alpha = \frac{1}{2}\sum_{i=1}^{N}\sum_{j\neq i=1}^{N} n_i z_{ij} J_{ij} S_i S_j \sigma_i^{(\alpha)} \sigma_j^{(\alpha)} \tag{2.34}$$

where $\sigma_{i,j}^{(\alpha)}$ take values ± 1. From this expression, and taking into account that $n_i z_{ij} = n_j z_{ji}$, we can derive the energy difference between the groundstate α_0 and a configuration α_k, in which the kth sublattice spin is inverted relative to α_0, to be:

$$\Delta(\alpha_k - \alpha_0) = -2 n_k S_k \sum_{j\neq k=1}^{N} z_{kj} J_{kj} S_j \sigma_k^{(\alpha_0)} \sigma_j^{(\alpha_0)} \tag{2.35}$$

where $\sigma_i^{(\alpha_0)}$ are the spin orientation of sublattice i at the groundstate. In a similar way, if we define the magnetic configuration α_{km} to have the spins of sublattices k and m flipped with respect to the groundstate, an expression for the energy difference between this configuration and the groundstate is given by:

$$\Delta(\alpha_{km} - \alpha_0) = \Delta(\alpha_k - \alpha_0) + \Delta(\alpha_m - \alpha_0) + 4 n_k z_{km} J_{km} S_k S_m \sigma_k^{(\alpha_0)} \sigma_m^{(\alpha_0)} \tag{2.36}$$

It is now straigthforward to show that the exchange constants J_{ij} between sublattices i and j can be directly determined from the expression [48]:

$$J_{ij} = \frac{E_{ij} + E_0 - E_i - E_j}{4 n_i z_{ij}\ \vec{S}_i^{\alpha_0} \cdot \vec{S}_j^{\alpha_0}} \tag{2.37}$$

where E_0 corresponds to the DFT total energy of the ground state spin configuration $\alpha = \alpha_0$, $E_{i/j}$ to that of the spin configuration where the spin of sublattice i/j has been inverted with respect to α_0, and E_{ij} to that where the spins of both lattices i and j have been simultaneously flipped.

This expression is formally valid only to first nearest neighbors, and thus we restrict our calculations to the exchange couplings between them.

2.5 Estimation of magnetic ordering temperature T_N

The transition temperature from ferrimagnetism to paramagnetism called Néel temperature T_N, have been estimated in this work under two different approaches: micro-magnetic Monte Carlo simulations and the Generalized Molecular Field Theory (GMFT).

The Monte Carlo simulations have been performed using the software package VAMPIRE [49] which uses the Metropolis algorithm [50]. The procedure is the following:

- Select a random spin S_i and change its direction to a new trial one S_i'
- Calculate the energy difference $\Delta E = E(S_i') - E(S_i)$ between the new state and the old one. If the system has reduced its energy, it is accepted unconditionally. If not:
- Compute the probability P of this new state to be accepted through the Boltzmann distribution $P = \exp\left(-\frac{\Delta E}{k_B T}\right)$, where k_B is the Boltzmann constant and T is the temperature

This process is repeated N times in which is called one Monte-Carlo step, with N the number of atoms in our system. To estimate T_N we perform this procedure for increasing temperature values, letting the system to adapt to its new temperature at each step (equilibration cycles) and computing the average magnetization for each temperature, getting the magnetization curve $M(T)$. When the net magnetization reaches $0\mu_B$, that is the temperature where the system undergoes a phase transition from ferro-(ferri-)magnetism to paramagnetism, that is the Curie(Néel) temperature. The starting point of this Monte Carlo simulation comes from the results of our *ab-initio* simulations, which formally correspond to $T = 0$ K. Specifically, the required input values are the exchange coupling constants and the magnetic moments of every atom, as well as the unit cell of the structure which is repeated in the 3-dimensions in order to work with a supercell.

A computationally less demanding, but also less accurate, estimation of the T_N can be obtained using GMFT, which represents a generalization of Weiss MFT to high order and anisotropic interactions [51, 52]. Within this theory, the so called Weiss molecular field acting on the atoms of the i-th sublattice, H_i, is given by:

$$H_i = H_0 + \sum_{j=1}^{n} \gamma_{ij} M_j \tag{2.38}$$

where H_0 is the external magnetic field, M_j the thermal averaged MM of the jth sublattice, defined as $M_i = g\mu_B\langle S_i\rangle$, where S_i is the spin of the atoms of sublattice i and g is the Landé factor. γ_{ij} are the molecular field coefficients for a field exerted on an i-th sublattice atom by a neighbor atom of the j-th sublattice: $\gamma_{ij} = 2z_{ij}J_{ij}/(N_j g^2\mu_B^2)$, with z_{ij} the number of j neighbors of an i atom, J_{ij} the exchange constant between i and j sublattices (here derived from the DFT calculations) and N_i the number of atoms at the $i-$th sublattice. Note that the γ_{ij} coefficients are symmetric and it is typical practice to set the diagonal terms $\gamma_{ii} = 0$, which implicitly assumes that intra-sublattice interactions are negligible.

The main idea behind the GMFT is to assume that the material behaves like a paramagnet at high enough temperatures well above the magnetic ordering temperature (T_N for ferrimagnets), in which case the magnetization may be expressed as:

$$M_i = N_i g\mu_B S_i B_S(\frac{g\mu_B H_i}{k_B T}S_i) \tag{2.39}$$

where B_S are the Brillouin functions. For temperatures sufficiently high, these functions can be approximated by $B_S(x) = \frac{S+1}{3S}x$, so one ends up with a system of linear equations:

$$M_i = N_i g\mu_B S_i \frac{S_i+1}{3S_i}\frac{g\mu_B H_i}{k_B T}S_i = \frac{C_i}{T}H_i = \frac{C_i}{T}(H_0 + \sum_{j=1}^{n}\gamma_{ij}M_j) \tag{2.40}$$

In order to calculate the critical temperature for the onset of paramagnetism, the external field is removed ($H_0 = 0$), and the non-trivial solutions to the above system of equations are obtained by setting the associated determinant to zero:

$$\begin{vmatrix} \frac{T}{C_1} & -\gamma_{12} & \cdots & -\gamma_{1n} \\ -\gamma_{12} & \frac{T}{C_2} & \cdots & -\gamma_{2n} \\ & & \ddots & \\ -\gamma_{n1} & -\gamma_{n2} & \cdots & \frac{T}{C_n} \end{vmatrix} = 0 \tag{2.41}$$

Chapter 3

Hexagonal ferrites: SFO

3.1 Introduction

Among the hexagonal ferrites, SFO ($SrFe_{12}O_{19}$) is particularly attractive, due to its large saturation magnetization and coercivity, a high uniaxial magnetocrystalline anisotropy and excellent chemical stability. It is an M-type hexaferrite isostructural to magnetoplumbite with space group $P6_{3/mmc}$. The SFO structure, shown in Fig. 3.1, has five different sublattices: $2a$, $2b$, $12k$ with parallel and $4f1$, $4f2$ with antiparallel magnetic moments (MMs), what makes it a ferrimagnet. Sublattices $2a$, $12k$ and $4f2$ have an octahedral environment (the latter being distorted due to the presence of the Sr atoms), $2b$ a bipyramidal one while $4f1$ is tetrahedrally coordinated. The magnetic coupling among most of the neighbor Fe ions is of the superexchange type with an oxygen atom involved in the Fe-O-Fe bond.

The main magnetic properties of SFO, that is a MAE of 1.9 meV at 100 K (or 1.4 meV at 300 K) and a Néel temperature of $T_N = 780$ K, have been measured decades ago[53]. Still, important properties such as the electronic gap have not yet been determined. In the last two decades, significant effort has been devoted to improve its magnetic performance, particularly for permanent magnet applications, by chemical substitution and nanostructuring [54, 55, 56, 57, 58]. Nanometric thin SFO platelets have been recently characterized combining fundamental experimental techniques, as X-ray absorption based and Mössbauer spectroscopies, to DFT calculations intended to rationalize Oxygen K absortion edge spectrum measurements [59]. Still, hardly any recent works have revisited the SFO magnetic structure in depth employing state-of-the-art experimental techniques. From the theoretical side, and since the early work of Fang *et al* [60] where Gorter's prediction [61] on the ferrimagnetic arrangement of the Fe sublattices was confirmed via

ab initio calculations, M-type hexaferrites (M=Ba,Sr) have been extensively studied [62, 63, 64, 65, 66, 67, 68, 69] A number of properties have been derived in these works including, among others, the electronic gap, the saturation magnetization (M_s) and the MMs on the Fe ions together with their associated spin-resolved DOS, the MAE [64, 66, 67] as well as exchange couplings (Js) subsequently employed in the estimation of T_N [48, 63] or the evolution of M_s with temperature [65]. In addition, a large effort has been put in exploring substitutional elements either for the M-ion (La [48, 62, 66], Pb [68], Pr [66], Nd [66]) or the Fe ions (Al [67], Zn-Sn [64]) in order to improve the material's magnetic performance. Most of these studies have relied on the DFT+U framework, paying special attention to the precise value of the Hubbard term U, for which values in the 3-10 eV range have been considered. However, the simultaneous influence of U on M_s, the MAE and T_N has not been addressed systematically in order to derive a unique value that can accurately describe the most relevant SFO's magnetic properties. Here we fill this gap performing a comprehensive characterization of the electronic and magnetic properties of SFO at the DFT+U level, providing estimates for the electronic gap, MMs, orbital angular momenta, MAE, Js and additionally, within a multi-scale spirit, the T_N, here obtained via Monte-Carlo simulations using as input solely the DFT-derived parameters. Moreover, and apart from a systematic study of the Hubbard term U, further attention is paid to physically relevant calculation parameters such as the precise lattice constant, the inclusion of spin-orbit coupling or the ions spin relaxation time in the evaluation of the exchange constants.

3.2 Methods

All *ab initio* calculations have been performed with the Green code [40, 41] and its interface to the SIESTA package. In a first stage both the LDA and the GGA approximations were considered for the exchange-correlation functional, although results will only be presented for the latter since LDA consistently provided larger structural deviations from the experimental SFO lattice parameters, as well as it often led to spurious low-spin states for the Fe ions so that, overall, it may be considered less reliable. Hubbard type corrections were included within the DFT+U formalism following the Dudarev approach [45, 71, 72]. For the single parameter U different values were considered while its effect on the computed SFO properties is extensively discussed in section 3.3.

A double-zeta polarized (DZP) atomic orbital basis set was defined for all elements. The AOs are strictly localized as determined from a confinement

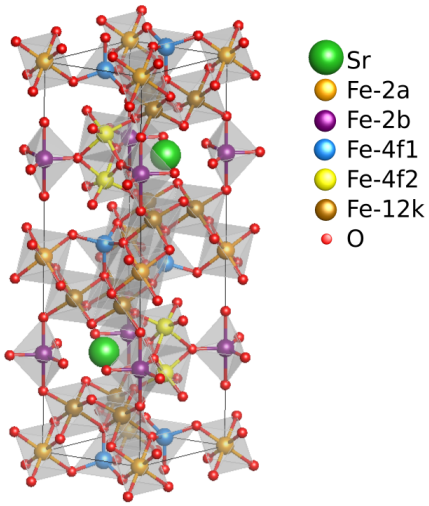

Figure 3.1: Atomic Structure of the SFO. The unit cell contains two formula units, $(SrFe_{12}O_{19})_2$, and has 64 atoms in total. The environement around each Fe ion has been shaded in order to highlight its coordination to oxygen atoms (tetrahedral, octahedral or bipyramidal). This figure has been obtained using VESTA [70].

energy of 100 meV. Pseudo-core corrections were included for both the Fe and Sr ions. The resolution of the real space grid was set to an ultra-fine value below 0.04 Å^3 (equivalent to a Mesh Cutoff of 2000 Ryd) to ensure a good convergence around the Fe cores, while the reciprocal space was sampled with a $(9 \times 9 \times 3)$ supercell. A value of 100 meV was used in the Fermi-Dirac distribution function (electronic temperature).

In the DFT models both the experimental SFO lattice constants ($a = b = 5.884$ Å and $c = 23.05$ Å) as well as the theoretically GGA optimized values ($a = b = 5.955$ Å and $c = 23.33$ Å) were considered. For both cases, in the determination of the SFO ground state all ions were allowed to relax until forces on atoms were below 0.02 eV/Å.

Exchange constants, J_{ij}, between sublattices i and j, have been calculated from the energy differences between different spin-collinear configurations, as explained in section 2.4. The number of nearest neighbours and their distances between all SFO sublattices are provided in Table 3.1. In order to determine the intra-sublattice exhange couplings, the *4f1*, *4f2* and *12k* groups have been splitted into sub-sublattices *4f1a-4f1b*, *4f2a-4f2b* and *4k-8k*, respectively. The other two intra-sublattice couplings, *2a-2a* and *2b-2b*, may be safely ignored due to their large nearest neighbor distances (see Table 3.1). This leads to 13 exchange constants for this material: J_{2a-2b},

	$2a$	$2b$	$4f1$	$4f2$	$12k$
$2a$	5.95 (6)	5.84 (2)	3.50 (6)	5.62 (6)	3.09 (6)
$2b$		5.95 (6)	6.23 (6)	3.71 (6)	3.72 (6)
$4f1$			3.66 (3)	3.82 (1)	∼3.56 (9)
$4f2$				2.77 (1)	3.53 (6)
$12k$					∼2.98 (4)

Table 3.1: Nearest neighbours distances in Å and number of nearest neighbor ions, z_{ij}, in parenthesis, for the five Fe-sublattices, obtained for the theoretically optimized SFO lattice constants.

J_{2a-4f1}, J_{2a-4f2}, J_{2a-12k}, J_{2b-4f1}, J_{2b-4f2}, J_{2b-12k}, $J_{4f1-4f2}$, $J_{4f1-12k}$, $J_{4f2-12k}$, $J_{4f1-4f1}$, $J_{4f2-4f2}$, J_{4k-8k} which, according to eq. (2.37), require up to 21 different spin configurations apart from the ground state.

A systematic study of the influence of U on the J_{ij} constants has been performed via DFT calculations for the 22 spin configurations varying U between 0 and 5 eV in 1 eV steps. These sets of calculations have been done for both the experimental and the theoretically optimized lattice constants. Furthermore, the exchange constants have been computed under two different limits. In a first stage the optimized ground state geometry (calculated independently for each U value) was used for all spin configurations α. Such standarized approach assumes that the spin orientation on the atoms evolves in time much faster than the ions themselves move as a consequence of the *exchange* forces. Thus, it is denoted as the *static* limit. In a second stage the SFO geometry was optimized for each magnetic configuration independently, thus simulating a *dynamic* limit where the spin relaxation time would be much longer than the atoms response to the exchange forces.

It should be noted, however, that the assumption in eq. (2.37) that the modulus of $\vec{S}_i^{\alpha}$ does not change among spin configurations was not fullfilled in certain cases for U$\leq$ 1 eV. Figure 3.2 provides a summary of the MMs per Fe sublattice for the 22 spin configurations and all U values considered. Although most of the MMs remain fairly constant (within less than 0.5 μ_B) for all α, at small U values sublattices $2a$ and $4f2$ suffer a drop of their MMs to low spin states in a few spin configurations, thus invalidating the estimation of the Js via eq. (2.37). Therefore, results of the exchange constants are presented for values of U$>$ 1 eV only. Recall, however, that no low spin-states appear for the ground state (case α =0) in any of the sublattices throughout the entire U range.

Micro-magnetic Monte Carlo simulations have been performed within the software VAMPIRE [49] using our DFT+U results (exchange constants

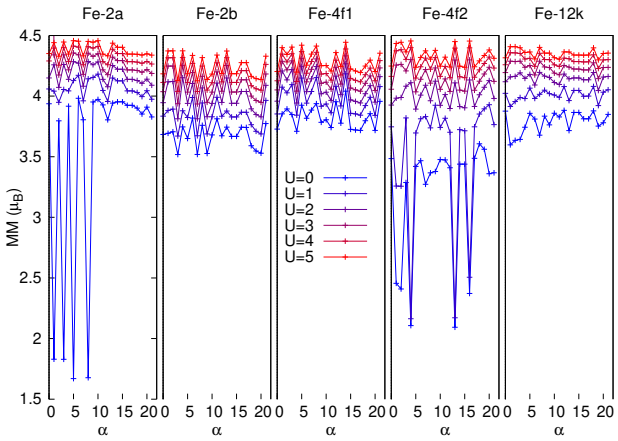

Figure 3.2: MMs for each Fe sublattice as a function of the spin configuration index α (the case $\alpha = 0$ corresponds to the ground state). Each color corresponds to a different value of U, as indicated in the legend in eV. The MMs in sublattices $2a$ and $4f2$ attain anomalously small values (low spin states) when U$\leq$ 1 eV at some specific spin configurations.

and MMs) as inputs to estimate the Néel temperature, T_N, of the SFO. A $(5 \times 5 \times 5)$ supercell comprising only Fe sub-lattices was employed in these calculations (leading to a total of 3,000 atoms). The temperature of the system was slowly increased from 0 K up to 1500 K in 20 K steps. Each temperature step included 50,000 equilibration cycles followed by another 50,000 time steps.

Alternative, less accurate, estimations of T_N have been performed under the Generalized Molecular Field Theory as explained in section 2.5. In order to get rid of the diagonal terms $\gamma_{ii} = 0$, it is required to remove any intra-sublattice interaction. In SFO, this is done by splitting sublattice $12k$ into 3 different sub-sublattices each with four atoms. The rest of the sublattices don't show intra-sublattice interaction.

In SFO, the equation 2.41 leads to a 7×7 determinant that leads to 7 different critical temperatures, each of them associated with a transition to a specific spin arrangement. The one with the highest value corresponds to the Néel temperature, T_N.

3.3 Results and discussion

3.3.1 Projected charges and magnetic moments

The effect of the Hubbard term on the electronic and magnetic properties projected on each sublattice for the ground state spin configuration is first explored. Figure 3.3(a) shows the dependence of the Mulliken charges with U. Although the Mulliken population analysis, being basis dependent, is known to be imprecise when estimating projected charges on ions, it nevertheless provides reliable trends. Here, the non-distorted octahedral Fe-ions (sublattices $2a$ and $12k$) become more ionized (hold less electronic charge) than the $4f1$ and $4f2$ ones which attain almost the same charges despite having different number of oxygen neighbors, while the bipyramidal $2b$ is clearly the less ionized one. All charges diminish with U in the same way (around $0.1e$ loss in the entire U range), implying that the Hubbard term leads to a slightly more ionic character of the Fe-O bonds. In the same figure the evolution of the band gap is shown as well (dark line). As expected, it increases considerably with U, starting from an almost gapless situation (U=0) and reaching a value of 1.0 eV for U= 5 eV. These values are smaller than the reported SFO gaps in previous DFT+U works which, for U$\approx$ 3 eV, are in the 0.7-1.0 eV range [62, 64, 68] versus the 0.5 eV found here. The discrepancy may be assigned to the tendency of the SIESTA formalism to underestimate gaps in semiconductor and insulators probably due to the finite basis set employed. Unfortunately, there is no reported experimental value of the SFO band gap which could be directly compared with the calculated data and, hence, help in the determination of an optimum U.

Figure 3.3(b) displays the MMs per Fe sublattice as a function of U. Roughly, the behaviour of the MMs is anti-correlated with that of the projected charges; the formers increase with U in a non-linear way whith sublattices $2a$ and $12k$ presenting the largest MMs. The increase in the MMs in the U= $0-5$ eV interval ($\sim$0.5 μ_B) is similar for all ions except for the anti-ferromagnetically coupled $4f2$ sublattice, which shows a much larger increase of around 0.8 μ_B. To understand this behaviour, Figure 3.4 shows the spin-resolved PDOS on the iron atoms for U= 0 eV (black lines) and 3 eV (yellow). Apart from the opening of the gap, the main effect of the Hubbard term is a clear shift towards lower energies for the majority components and towards positive energies for the minority electrons, hence yielding a net increase of the MMs of all ions. The largest shift occurs for the minority PDOS of the $4f2$ ions, which explains their stronger dependence with U. Upon comparison of the calculated MMs with those reported by Liyanage *et al* [64], which may be considered as the most accurate ones as they were obtained

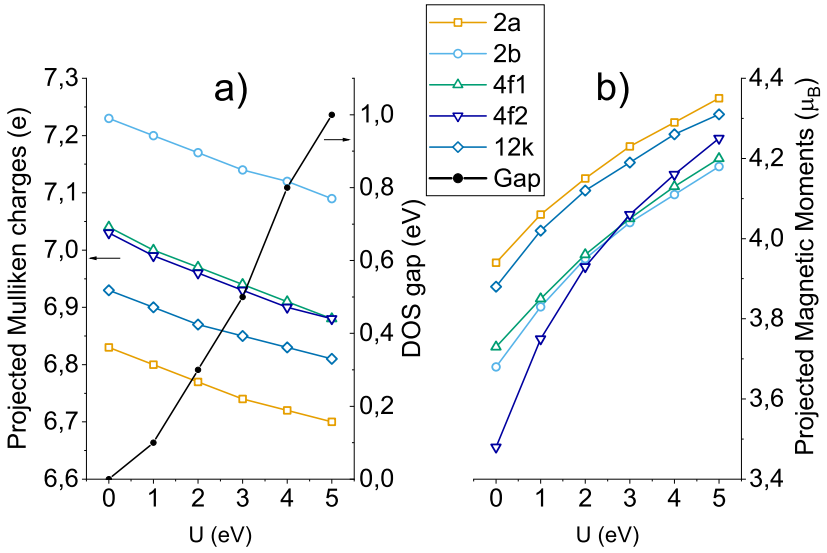

Figure 3.3: Evolution with the Hubbard term U of: (a) the Mulliken charges and, (b) the absolute value of the MMs, projected on the Fe sublattices. In (a) the dark line shows additionally the calculated SFO band gap (right y-axis).

under a hybrid exchange-correlation functional free of the Hubbard parameter, an excellent agreement (within 0.06 μ_B) is obtained for all sublattices for the U=3 eV case (that is, close to the U=3.7 eV deduced in Ref.[[64]]).

In summary, increasing U leads to larger magnetic moments, a larger gap and slightly more ionized bonds, which is fully compatible with the fact that the Hubbard term induces a higher level of localization in the Fe-d states.

3.3.2 Exchange couplings

The SFO exchange constants have been obtained from eq. (2.37) employing up to 22 different spin configurations and systematically varying the U term in the $2-5$ eV interval. In order to check the robustness of our approach, two different unit cell volumes have been considered (the experimental (E) and the theoretically optimized (T) ones) as well as the static (S) and dynamical (D) limits concerning the response time of the ions' positions to an inversion of their MMs, as explained in section 3.2. Throughout this subsection, the calculation conditions used for each set of Js will be denoted by two capital letters: ES, ED, TS or TD (for instance, ED refers to Js calculated employing the experimental lattice constants under the dynamic limit).

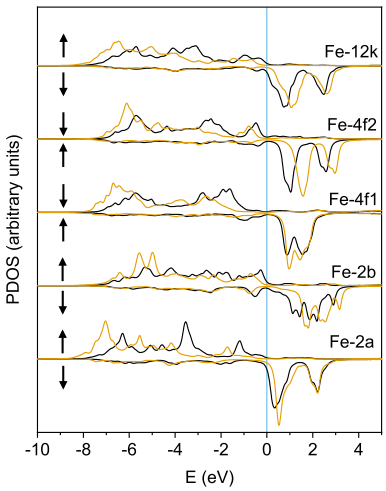

Figure 3.4: Spin-resolved PDOS for the five Fe sublattices computed at two different U values: 0 eV (black lines) and 3 eV (yellow). For each sublattice the majority spin component along the positve y-axis and the minority along the negative y-axis are plotted. Notice that since the $4f1$ and $4f2$ sublattices are antiferromagnetically coupled to the rest, their up and down spin directions (indicated by arrows at the left of each plot) are interchanged.

Figure 3.5 presents the dependence of the most relevant exchange constants on U for the ES case (the same trend is found for the other three cases). A strong decay in the strength of almost all interactions is apparent as U increases, which is in line with the results of Wu *et al* [48] and Novak *et al* [63] for Ba hexaferrite and derives from the fact that the Hubbard term tends to localize the d-states at the Fe sites and hence, their MMs become less influenced by the precise magnetic state of the neighboring ions. Furthermore, all Js remain positive indicating a robust anti-ferromagnetic character. The most relevant constants are $J_{4f2-12k}$ and J_{2b-4f2}, which attain values over 12 meV at U=2 eV and decrease to around 8 meV at the largest U. $J_{4f2-12k}$ and J_{4k-12k} are the next in relevance ($J \approx 10$ meV for U=2 eV), with the latter showing the largest decrease with U as its initial value ends up reduced by $\sim$50%. The J_{2b-12k} and $J_{4f1-4f2}$ interactions take intermediate values between 3 and 6 meV, with the latter showing an *anomalous* behaviour for U$>$ 3 eV as the slope becomes slightly positive. Finally, J_{2a-12k} and $J_{4f1-4f1}$ attain small values between $1-2$ eV. The rest of couplings, namely J_{2a-2b}, J_{2a-4f2}, J_{2b-4f1} and $J_{4f2-4f2}$, have been omitted since they attained almost negligible values below 1 meV in all cases considered.

In order to rationalize the hierarchy among the calculated Js, it should

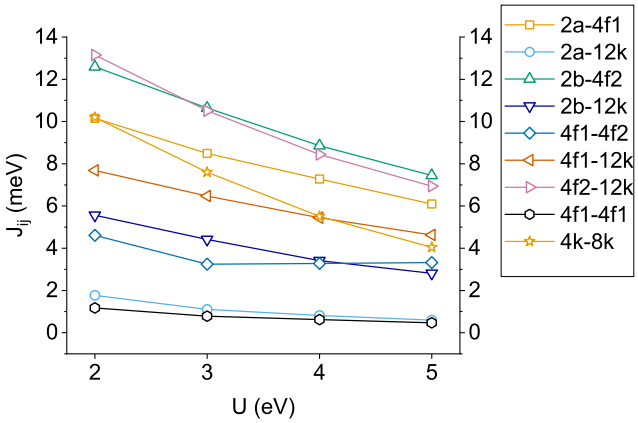

Figure 3.5: Dependence of the most relevant exchange coupling constants, J_{ij}, on the Hubbard parameter U for the ES case.

be first noted that their strengths do not correlate with the inverse of the direct Fe-Fe distances (see Table 3.1). Instead, and as expected for a super-exchange type coupling, it is the angles, θ, and distances, d, of the Fe-O-Fe bonds what determine their relative strengths. Figure 3.6(a) shows the value of the couplings as a function of the Fe-O-Fe bond distance for the ES case and U=3 eV –only the eight Fe-Fe couplings mediated by an oxygen atom are included. There is an obvious correlation with the bond distances, as all Js with $d < 4$ Å attain values above 6 meV, while beyond this distance they become clearly smaller. The dependence of the same constants on θ is displayed in Figure 3.6(b). Overall, small J values correspond to angles $\theta < 110°$ while almost all of the larger Js appear at greater angles. This behaviour corroborates the GKA rules, which, as mentioned in Chapter 1, dictate that the 180° super-exchange interaction with partially filled d orbitals is strongly antiferromagnetic, while 90° bonds tend to be weaker (and sometimes even ferromagnetic). Here, a clear trend towards stronger anti-ferromagnetic coupling is obtained as θ approaches 180° . The rest of interactions which do not involve an oxygen atom attain values below 1 meV with the only exception of $J_{4f1-4f2}$, indicating that this is the only relevant direct exchange term in the SFO.

The effect of varying the lattice constant or relaxing each spin configuration is shown in Figure 3.7, where the Js corresponding to the ED, ES, TD and TS calculation conditions are displayed side by side, all obtained for a Hubbard term of U=3 eV (equivalent trends are found for the U=2 eV and U=5 eV cases). Two main general conclusions become apparent from this

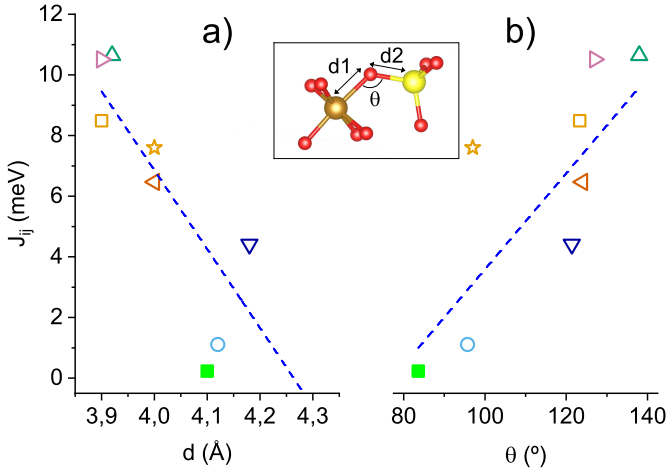

Figure 3.6: Dependence of the exchange constants strength, J_{ij}, on: (a) the total Fe-O-Fe bond distance, $d = d_1 + d_2$, and, (b) the super-exchange Fe-O-Fe angle θ (see inset). Each exchange constant is represented by the same symbol as that used in Fig. 3.5, while all values correspond to the ES and U=3 eV case. In both plots the blue dashed line is a guide to the eye.

comparison: (i) the expanded theoretical unit cell yields smaller exchange constants by 10% than the experimental one, which is easily understood from the above discussion due to the increase of the Fe-O-Fe bond distances and, (ii) the dynamical approach tends to provide slightly larger Js for the two lattice constants. The explanation to this latter effect is more subtle and derives from the balance in eq. (2.37) between the energy gain per unit cell, ΔE, upon relaxation of spin configurations i plus j versus that of the combined spin configuration ij. The results indicate that $\Delta E_i + \Delta E_j$ tends to be larger than ΔE_{ij}, although this is not a general rule and some exceptions can be seen in the figure (for instance, the $4f1 - 12k$ and $4f2 - 12k$ interactions).

Finally, the influence of the inclusion of the spin-orbit interactions on the exchange couplings has been examined for some selected cases. However, for the largest Js the difference was only $\sim 0.2\%$, indicating that SOC may be safely ignored when computing the exchange constants. This is not surprising since energy differences between different spin configurations are typically of the order of eVs, while SOC contributions are at least one order of magnitude smaller.

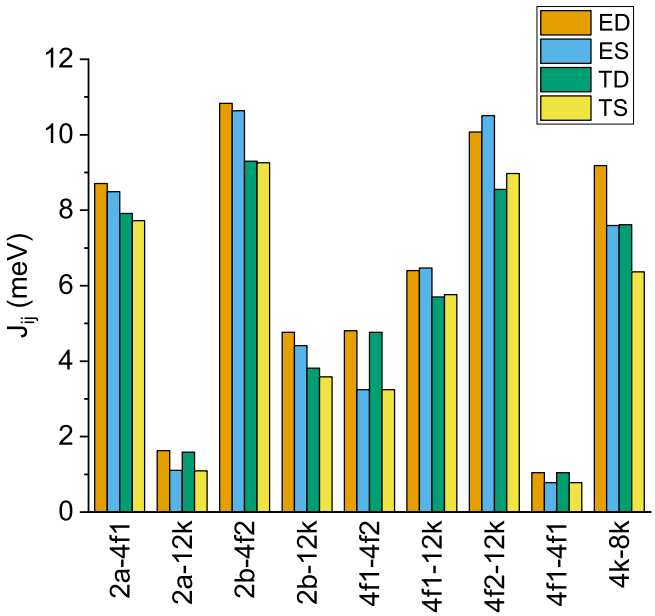

Figure 3.7: Comparison between the exchange constants obtained under different calculation conditions: experimental lattice under the static (ES) and dynamic (ED) limits, as well as theoretically optimized lattice under the static (TS) and dynamic (TD) limits. All results correspond to the case U=3 eV.

3.3.3 Néel temperature, T_N

Once the magnetic moments and exchange constants under different calculation conditions have been obtained, the SFO's Néel temperature, T_N, may be estimated following two different approaches: (i) analytically using the Generalized Molecular Field Theory (GMFT) and, (ii) numerically via Monte Carlo simulations (see section 3.2).

Figure 3.8(a) shows, as a function of U, the T_Ns derived from the GMFT formalism after employing the DFT derived J_{ij} constants (ES case) in expression (2.41). The graph shows a clear linear dependence with a strong decrease of the temperatures as U increases. However, even at the largest U value considered, T_N is close to 2,000 K, that is, more than twice the experimental value, $T_N^{exp} = 780$ K. In fact, by linear extrapolation T_N^{exp} would be recovered at a U value as large as 7.3 eV. It should be recalled that a mean field approach was also employed in Refs. [63] and [48] and, similar to our case, a best fit to the experimental Néel temperature could only be obtained for a large Hubbard term U$\geq$ 7 eV (inclusion of spin fluctuations at the RPA level reduced the T_N overestimation but, still, yielded optimized U values of

around 7 eV).

Panel (b) in Figure 3.8 displays the Néel temperatures obtained from the Monte Carlo simulations as a function of U and for the four calculation conditions described above. Plots of the evolution of the cell magnetization with the system temperature, from which the T_N values are deduced, are presented in panel (c). Although T_N also decreases as U is increased, this time all curves reach values close to T_N^{exp} in a narrow U=2.5 – 3.2 eV range, with the ED and ES cases yielding slightly larger critical temperatures (for fixed U) than the TD and TS ones, as expected from the similar behaviour followed by the exchange constants (Fig. 3.7). The main conclusion, therefore, is that the Monte Carlo approach results more reliable than the GMFT, as it leads to an *optimized* Hubbard term clearly smaller than that derived from the GMFT, ∼3 eV versus ∼7 eV, in better agreement with the 3.7 eV deduced in Ref. [64] as well as with a number of DFT+U calculations involving Fe ions under different chemical environments [73, 74, 75, 76].

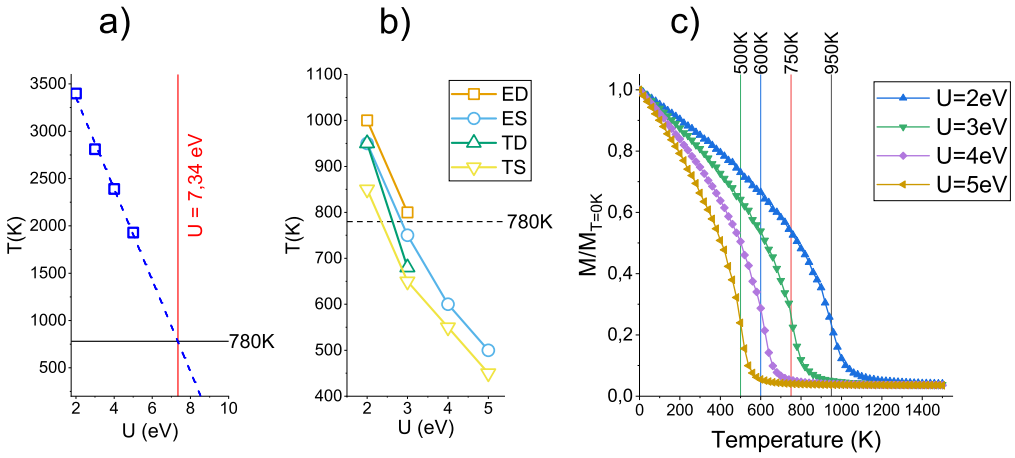

Figure 3.8: Néel temperature as a function of the U parameter obtained from: (a) the GMFT approximation (blue squares) and, (b) Monte Carlo simulations for the ES, TS, ED and TD calculation conditions. The horizontal dashed line indicates the experimental T_N^{exp} value in both panels. In (a) the blue dashed line is a linear fit to the data points. (c) Total magnetization of the unit cell normalized to that at $T = 0$ as a function of the system temperature in the Monte Carlo simulations. Data obtained from the ES exchange constants and for different U values. The Néel temperature, T_N, in each case is indicated by the vertical lines.

3.3.4 Magnetic anisotropy and orbital angular momenta

In this section magnetic properties which require the inclusion of SOC in the DFT+U calculations are addressed (see section 3.2). Focusing first on the magnetic anisotropies, Figure 3.9(a) shows the evolution of the SFO's total energy per unit cell, E_θ, as the spin quantization axis is rotated from the out-of-plane (0001) direction ($\theta = 0$) to the in-plane (1000) direction ($\theta = 90°$) and for the different U values considered. In these calculations, evaluated at the experimental lattice constant, the SOC has been included at the level of the force theorem approximation. All curves show a nice $K \sin^2\theta$ behavior, with a marked perpendicular magnetic anisotropy (PMA), although it is steadily reduced as U is increased. The associated MAEs, defined as the difference $K = E_{90°} - E_{0°}$, are displayed in Figure 3.9(b), where the evolution of the PMA is plotted as a function of U and for both the experimental and theoretical lattices (solid red and blue lines, respectively). For a fixed U value, the PMAs calculated at the experimental lattice constant are always larger than those obtained using the theoretical lattice. Naively, the decrease of the PMAs with increasing unit cell volume or increasing U may be understood from the reduction of the effective crystal field due to either smaller Fe-O overlaps or an increased electron localization. Nevertheless, the most relevant conclusion in Fig. 3.9(b) is that, for the experimental lattice constant, the low temperature experimental PMA of 1.9 meV [53] is retrieved for U$\approx$ 2 eV, which is close to the optimum 3 eV value deduced in the previous subsection. Notice that the fitted U in the figure approaches 3 eV if the 300 K experimental PMA value of 1.4 meV is considered instead.

In the same figure the MAEs calculated self-consistently, that is, beyond the FT approximation, are also shown by dashed lines. They present the same trend with U as their FT counterparts, but attain smaller values (by more than 0.5 meV) which are in closer agreement with previous MAE calculations on M-hexaferrites where PMAs of around 0.8 eV were reported for U in the 3.7-4.5 eV range [64, 66, 67]. As a consequence, the experimental MAE is retrieved at unusually small values of U$\approx 1.0 - 1.5$ eV. Nevertheless, we consider more reliable the MAEs derived from the FT given their nice $\sin^2\theta$ behavior for all U values (panel (a)) while the self-consistent approach failed to yield such smooth MAE(θ) curves for finite U –mainly due to numerical instabilities in the precise occupation number of the Fe-3d states. Furthermore, and as expected from the relatively small SOC of the Fe ions, the FT reproduces fairly well the self-consistent values in the absence of the Hubbard term (U=0).

Last, Figure 3.10 shows the orbital magnetic momenta (OMM) in ab-

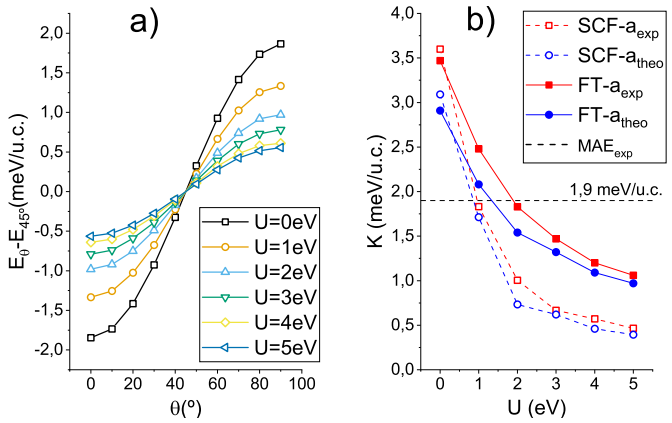

Figure 3.9: (a) Total energies per unit cell (u.c.), E_θ, obtained under the FT approach for different polar angles of the spin quantization axis ($\theta = 0$ corresponds to out-of-plane magnetization and $\theta = 90°$ to in-plane). All curves have been substracted by their value at $\theta = 45°$ for visual purposes. The MAE in each case is given by the difference $K = E_{0°} - E_{90°}$. (b) Evolution of the MAEs with the Hubbard term U calculated for both the experimental and theoretically optimized lattice constants a_{exp} and a_{theo}, respectively. SOC has been included either at the FT level (solid lines) or self-consistently (dashed lines). The dashed horizontal line corresponds to the experimental MAE per unit cell.

solute value calculated for the experimental lattice and including SOC self-consistently for the spin quantization axis aligned out-of-plane, panel (a), and in-plane, panel (b). The net OMM of the SFO unit cell (black lines and right axis) attains a considerable value of 0.25 μ_B at U=0, but decreases non-linearly as U increases down to $\sim 0.13\mu_B$ at U=5 eV. The OMMs of the individual Fe-ions (colored lines and left axis) are an order of magnitude smaller; still, they also follow the same trend with U (recall that the sign of the OMMs for the $4f1$ and $4f2$ ions appears inverted in the graph). Panel (c) displays the orbital magnetic momenta anisotropy (OMMA) defined as $L_z - L_x$ (here the sign of the $4f1$ and $4f2$ ions has not been inverted). The OMMA of the SFO remains out-of-plane but, unexpectedly, it increases with the Hubbard strength –we associate the small kink at U=4 eV to numerical inaccuracies– as a result of a stronger attenuation with U of the out-of-plane OMM. A similar behaviour is found for all individual ions, with the peculiarity that the $2a$ and specially the $2b$ sublattices show an in-plane OMMA at small U values. It is timely to note that the opposite dependence on U between the OMMA and the MAE points to the fact that the correla-

tion between the two quantities is far from trivial, as it is often assumed in perturbative theoretical approaches [77, 78].

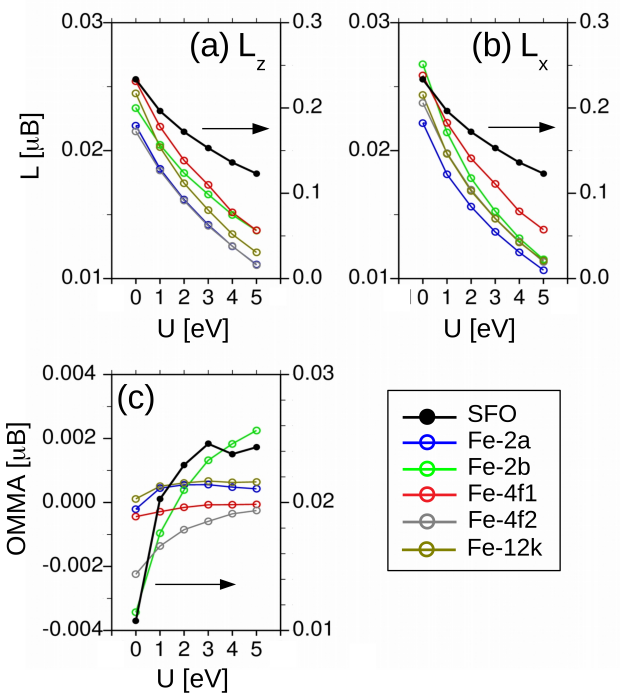

Figure 3.10: OMMs for the SFO unit cell (black line and right axis) and for each Fe ion (colored lines and left axis) for: (a) out-of-plane and, (b) in-plane spin quantization axis. In both plots the sign of the antiferromagnetically coupled $4f1$ and $4f2$ sublattices has been inverted for visualization purposes. (c) Orbital magnetic moment anisotropy, OMMA=$L_z - L_x$, for the SFO and each of the Fe sublattices. Here the signs of the $4f1$ and $4f2$ ions have not been inverted, so that their negative values correspond to an out-of-plane OMMA.

3.4 Conclusions

A comprehensive study at the DFT+U level of the magnetic properties of the strontium hexaferrite (SFO) has been performed, providing estimates of the Fe-resolved spin and orbital magnetic moments, the MAEs and the associated exchange constants. Furthermore, the influence of different calculation parameters on these properties, such as the Hubbard strength, the precise

lattice parameters or the relaxation time of the ions versus spin relaxations (static or dynamic limits) has been explored in detail.

It has been found that, by far, the most relevant parameter is U, as it progressively induces a larger electron localization around the ions which translates into larger gaps and MMs, smaller Js and smaller MAEs and OMMs (but, surprisingly, larger OMM anisotropies). Rather than a drawback, such a strong dependence may be considered as an excellent opportunity for deriving an optimium U value for $3d$ electrons in different magnetic systems. Here, a value of U$\approx 2-3$ eV nicely reproduces the experimental MAE and yields exchange constants which, when employed in micro-magnetic Monte Carlo simulations, accurately reproduce the SFO's Néel temperature as well. Our results are at contrast with similar studies on Ba-hexaferrite [48, 63] where anomalously large U values of $6-10$ eV were required to obtain, via the random phase approximation (RPA) or a mean field approach, T_N temperatures close to the experimental ones.

We note that it is common practice within DFT+U studies to treat the Hubbard strength as an adjustable parameter; its value is tpycally tuned to obtain specific electronic (mainly the gap) or thermodynamic properties [72, 74, 76, 79, 80]. However, and apart from atomic MMs, magnetic properties such as the MAE or the critical temperature are rarely employed as targets [48, 81] in the fitting process. In this work it has been shown that from the simultaneous fit to both quantities, meaningful U strengths are obtained which can ultimately deliver reliable *ab initio*-derived parameters for use in micromagnetic simulations.

Chapter 4

Cubic spinel ferrites

In this chapter, we show our results on the structural, electronic and magnetic properties of the bulk forms of Co-, Ni-, Zn- and Mn- ferrites. Cubic spinel ferrites are key elements for numerous magnetic applications, including rare-earth-free permanent magnets, switching and recording devices, color imaging, magnetic refrigeration or diverse biomedical solutions, from drug delivery to detoxification of fluids [82, 83, 84, 85, 86, 87]. Their stability under extreme conditions, together with their robust magnetism, low eddy current losses, abundance and low cost confer spinel ferrites an added value. We will present our results for the bulk structure of each oxide at a separate section.

These ferrites have been widely studied by *ab-initio* methods previously, and we base the theoretical conditions of our study on this previous knowledge [88, 89, 90, 91, 92, 93, 94, 95, 96, 97, 98, 99]. They all have a cubic spinel structure, shown in Figure 4.1, with a chemical formula TFe_2O_4, T standing for the transition metal ion. The oxygens occupy an fcc lattice interconnected with another incomplete fcc lattice made of two cations with octahedral coordination (B) and one tetrahedrally coordinated cation (A) filling the voids. Iron atoms can be distributed over the tetrahedral and octahedral sites in different manners, the extreme cases called *direct* (or *normal*) spinel structure, in which all trivalent ions (Fe^{3+}) are placed in octahedral positions and the divalent ions (Co^{2+}, Ni^{2+}, Zn^{2+} or Mn^{2+}) in tetrahedral positions, and *inverse* spinel structure, where half of the irons are in octahedral and half in tetrahedral sites, divalent ions occupying the rest of the octahedral sites. In practice, intermediate cases can be found depending on the specific preparation conditions. Commonly, it is defined the degree of inversion λ, with $0 \leq \lambda \leq 1$, $\lambda = 0$ corresponding to *direct* and $\lambda = 1$ to *inverse* structure. In general, these ferrites show a magnetic order in which the magnetic moments of A cations are antiparallel to those of B cations, which makes them ferri-

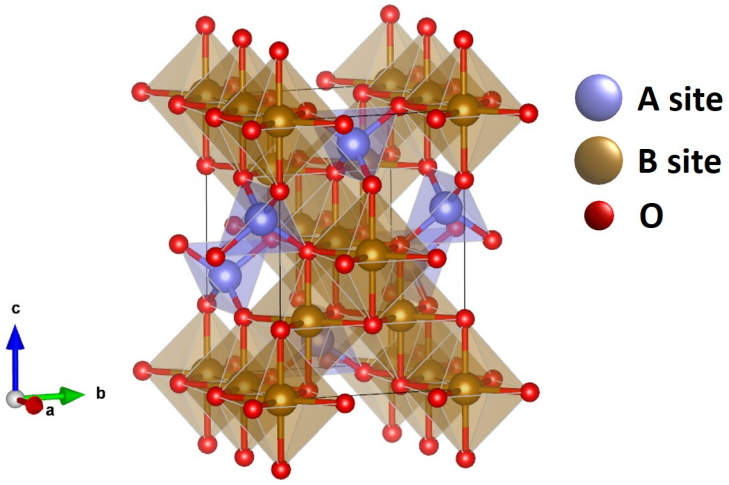

Figure 4.1: Atomic structure of the cubic spinels. The unit cell contains four formula units (TFe_2O_4) with 28 atoms in total. Shaded regions show the polyhedra that define the coordination units of each cation, distinguishing octahedral and tetrahedral sites.

magnets. However, as we will see in section 4.3, and due to the fact that zinc is a non-magnetic atom, ZFO shows a more complex magnetic behaviour, in which there is a competition between different magnetic orders. Besides, the degree of inversion plays a fundamental role in the magnetic behavior of CFO, that behaves as a *soft* magnet at the *direct* spinel structure and as *hard* at the *inverse* spinel structure. All these aspects will be considered when describing the corresponding oxides.

All the calculations in this chapter have been performed with the Vienna *ab-initio* simulation package VASP which is based on a plane wave basis set within the PAW method, using an energy cutoff of 500 eV and sampling the Brillouin zone with a $(7 \times 7 \times 3)$ k-mesh. Electronic relaxations were carried out self-consistently until convergence in energy of 10^{-5} eV was reached. In those calculations involving ionic relaxation, the atoms were allowed to relax until the forces were below 0.004 eVÅ^{-1}. We start analyzing the properties and relative stabilities of the *inverse* and *direct* forms of CFO, NFO and MFO for different magnetic configurations as a function of the effective Hubbard U under Dudarev approach, using the same U value on all magnetic cations (Fe, Mn, Co, Ni) 4*d* electrons. This choice of applying the same U to all *d* states of all transition metal ions is not fortuitous, but rather has proven to provide a realistic description of CFO and NFO ferrites [88, 89, 100]. Then we show our results on ZFO, with a more complex magnetic structure depending on the Zn distribution.

4.1 $CoFe_2O_4$ (CFO)

This section is organized as follows: first, we will study the relative stability between the direct and inverse spinel structures using two different exchange-correlation functionals, PBE and PBEsol, and also exploring the effect of the Hubbard U value. Then, we evaluate the electronic structure, charge and magnetic moment of each atom and the magnetic anisotropy. Lastly, we calculate the exchange coupling constants and we estimate the Néel temperature using Monte-Carlo simulations and the Generalized Molecular Field Theory.

4.1.1 Structural properties

In this section we focus on both the relative stability between the inverse and direct forms, and their lattice structure. The degree of inversion λ in these spinel ferrites is important because it ultimately affects key magnetic properties such as saturation magnetization and magnetic anisotropy. Experimentally, a large λ is found for cobalt ferrite, with a low but not null probability of finding iron atoms at tetrahedral sites, indicating the dominance of the inverse spinel structure [91, 101, 102]. We explore the relative stability between the two extreme λ, relaxing all the ions within the unit cell until forces were below $0.004eV$Å. We find an energy difference of $0.11eV/f.u.$ (per formula unit) between λ=0,1 favoring the *inverse* structure. When ionic relaxations are not allowed, the inverse CFO structure is favored with a considerably larger energy difference of $0.54eV/f.u.$. This indicates that breaking the internal cubic symmetry of the atomic positions favors the direct structure. The effect might also be used to tune the growth of CFO, as it suggests that, when slowly grown so as to approach equilibrium conditions, CFO tends to favor lower degrees of inversion.

We start exploring the long range magnetic order based on the ideal cubic structure at the experimental lattice parameter $a_{exp} = 8.392$Å. The magnetic configurations considered are: ferromagnetism, which is defined with all magnetic moments (MMs) aligned at the same direction (this corresponds to c1 in Table 4.1 for the *inverse* spinel); ferrimagnetism between A and B sites, which is defined with the MMs of the ions at A sites oriented antiparallel to those at B sites (c0 at Table 4.1); ferrimagnetism between Fe and Co atoms, which is defined only for *inverse* form and corresponds to Fe and Co MMs antiparallel to each other (c2 at Table 4.1). The results of this study are shown in Figure 4.2, where besides the relative stabilities (top) we also include the internal pressure of each configuration (middle) and the total magnetic moment of the unit cell (bottom). This study has been done for

Magnetic configuration	Fe_A	Fe_B	Co
c_0 (AF)	$-$	$+$	$+$
c_1 (FM)	$+$	$+$	$+$
c_2	$-$	$-$	$+$
c_3	$+$	$-$	$+$
c_4	$+/-$	$+$	$+$
c_5	$-/+$	$+$	$+$
c_6	$-$	$-/+$	$+$
c_7	$-$	$+/-$	$+$
c_8	$-$	$+$	$-/+$
c_9	$-$	$+$	$+/-$

Table 4.1: Schematic representation of the different magnetic configurations explored in an inverse spinel structure of CFO. + (−) sign accounts for the relative alignment of the spin sublattices. In configurations c4-c9, one magnetic sublattice is splitted in two (indicated with a forward slash (/))

two different exchange-correlation functionals, PBE and PBEsol, which have already been introduced in section 2.1.3, in order to find which one better describes the electronic and magnetic properties of our material. We notice that the ferrimagnetic state between A and B sites is the most stable case for both *inverse* and *direct* structures of CFO for the whole range of U values considered and both XC functionals, with essentially no difference in the E trends upon variations of U or the XC functional. The internal pressure of the structure at the middle panel, at the chosen lattice parameter, is an indicative of the stability of that structure. Middle panels of Figure 4.2 show that, in general, PBE leads to larger pressures for any magnetic configuration, while PBEsol describes a structure with a lattice parameter closer to experiment for U values above 3 eV. Lastly, differences in total magnetic moment for the two exchange-correlation functionals are negligible. Except for the lowest U, the total magnetization is also stable upon variations of U.

We performed a similar study focusing solely on the most stable magnetic configuration, the ferrimagnetic state between A and B sites, which we call from now on just the *ferrimagnetic* state. We explored different U values for both XC functionals, varying the value of the structure lattice parameter. The results are shown in Figure 4.3. One of the first conclusions one can extract from these results is that PBE predicts smaller lattice parameters than PBEsol, which are determined by the minimum of the energy curves. It is also found that larger U leads to larger lattice parameters, and that, in order to recover a lattice parameter close to the experimental value a_{exp},

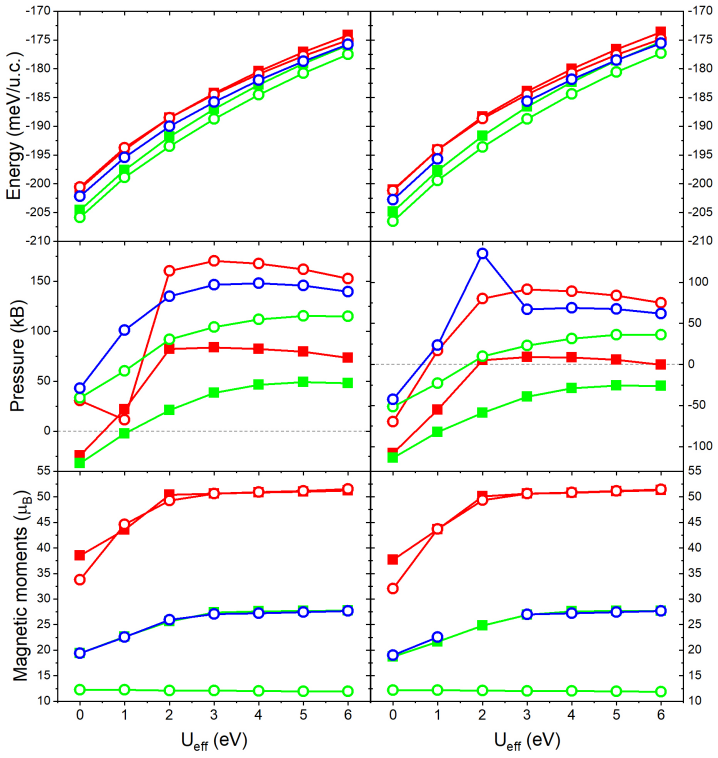

Figure 4.2: Left (right) panels show total energy (top row), pressure (middle) and magnetic moment of the whole unit cell (bottom) under PBE (PBEsol) functionals for the different values of U considered. Open circles and filled squares represent *inverse* and *direct* structures respectively. The different colors represent the different magnetic configurations considered: red for ferromagnetism (c1), green for ferrimagnetism (c0), and an additional configuration for *inverse* structure for ferrimagnetism between Co and Fe atoms in blue (c2).

we need to use a U close to 0eV when using PBE and larger U values when using PBEsol. However, the Hubbard U is needed to recover some important properties in these materials as it is the electronic band gap, as explained in Section 2.1.3. The total magnetic moment enlarges (diminishes) as U is increased at the *direct* (*inverse*) structure, and essentially no difference is found when using the different XC functionals. Hence, we concluded that PBEsol is more suitable to describe these materials, and from now on we will be using exclusively this exchange-correlation functional.

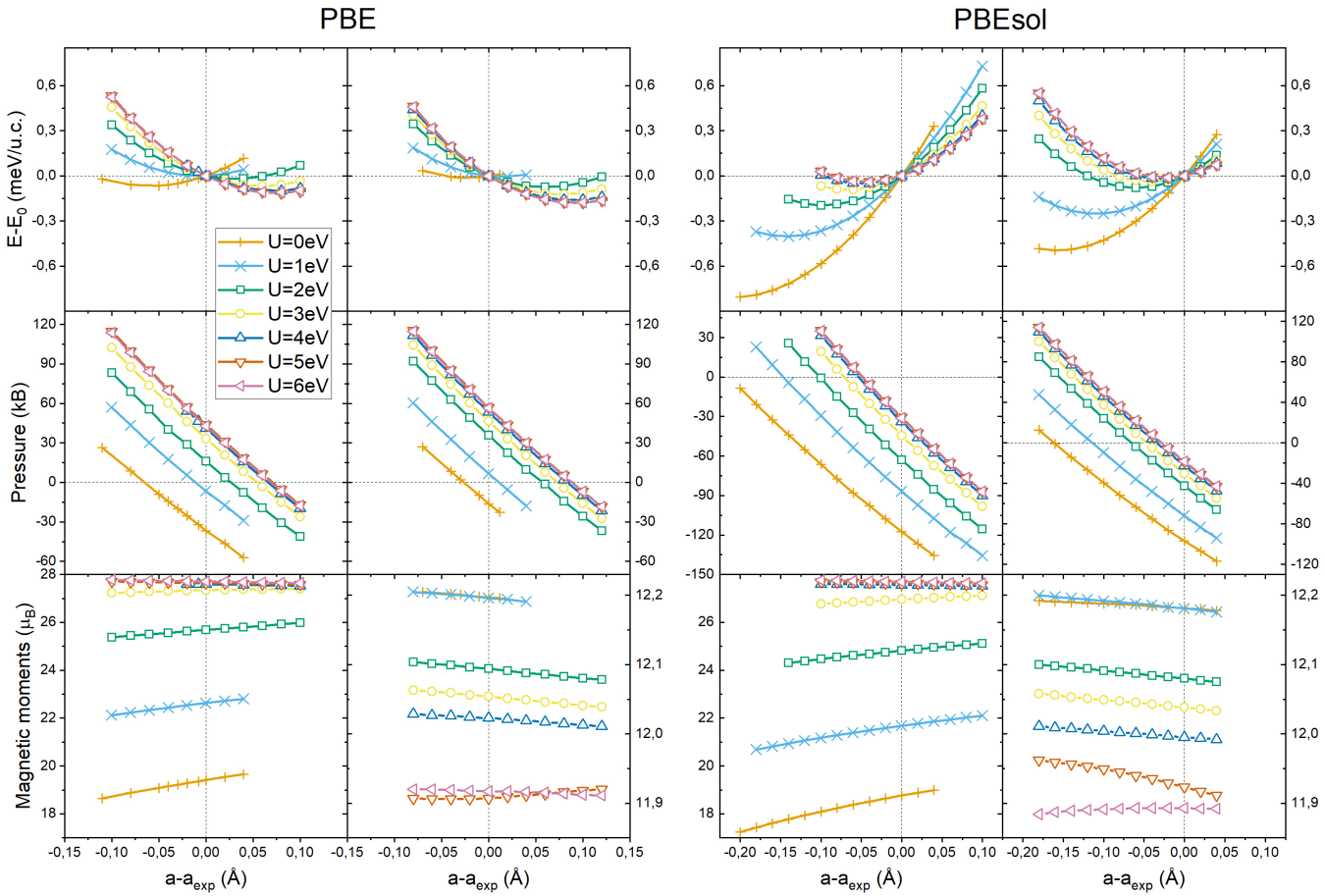

Figure 4.3: Energy referred to the groundstate (top panels), pressure (middle panels) and magnetic moment of the unit cell (bottom panels) with respect to the lattice parameter (referred to the experimental value, a_{exp}) for the different values of U considered. From left to right, columns represent: *direct* structure using PBE, *inverse* structure using PBE, *direct* structure using PBEsol, *inverse* structure using PBEsol. The experimental lattice parameter is $a_{exp} = 8.38$Å at the *inverse* structure and $a_{exp} = 8.40$Å at the direct.

4.1.2 Electronic and magnetic properties

The density of states and its dependence with the value of the Hubbard U is shown in Figure 4.4 for both inverse and direct spinel forms of CFO. As expected, the inclusion of electronic correlation through the Hubbard term is creating a band gap at the Fermi level, with a gapless situation for U< 2eV and U< 5eV at the inverse and the direct structures, respectively. The indirect band gap is experimentally found to lie between 0.8eV in nanoparticles [103] and 1.2eV in thin films [104]. This can be understood since the band gap decreases with decreasing inversion rate [104, 105, 106], and nanoparticles usually show smaller degrees of inversion (around 70%-80% [104, 107, 108]) than thin films (88% [109]). In our calculations, this band gap value is recovered at U = 4 eV. This is better seen through an example: as the direct and inverse forms contribute proportionally to the band gap, $\lambda = 0.8$ leads to $E_{gap}^{\lambda=0.8} = 0.2*0$ eV + $0.8*1.2$ eV = 0.96 eV, where the first and second terms refer to the direct and inverse contributions, respectively. Besides opening the gap, this graph shows how increasing U pushes the Co and Fe *d* states at the valence band (VB) and conduction band (CB) far apart, modifying the band width and the O-cation orbital overlaps.

The Bader charges of the different cations at the *inverse* spinel CFO are shown in Figure 4.5. A slight decrease is found with increasing U, meaning that the Hubbard term is favoring the ionic character of the cation bonds. The evolution of the electronic gap with the value of U, extracted from Figure 4.4, is also shown at Figure 4.5. The figure also shows the evolution with U of the magnetic moments, where opposite to trend for charges, increasing the Hubbard term is increasing the magnetic moments. This behavior can be explained by how the Hubbard term is affecting the spin-resolved PDOS of each atom, which is shown in Figure 4.6. There, PDOS is shown for U=0eV (black lines) and 4eV (green lines). There is a clear shift to lower energy values of the majority spin while the minority electrons are pushed towards positive energies, leading to an overall increase of the MMs of all ions. A similar behaviour, not shown here, is found at the direct CFO lattice.

We have also explored the magnetocrystalline anisotropy energy (MAE) of inverse and direct CFO including the SOC term. Experimentally, the bulk structure of both CFO forms has cubic symmetry, related to a random distribution of cations at the octahedral sites. Modeling a truly random distribution of cations in a finite unit cell has limitations, in fact just retrieving quasi-random distributions would imply enlarging the number of atoms in our unit cell, which largely affects the computational time and memory requirements. Moreover, MAE calculations are already computationally very demanding. For all this, in our model we are attached to a specific atomic

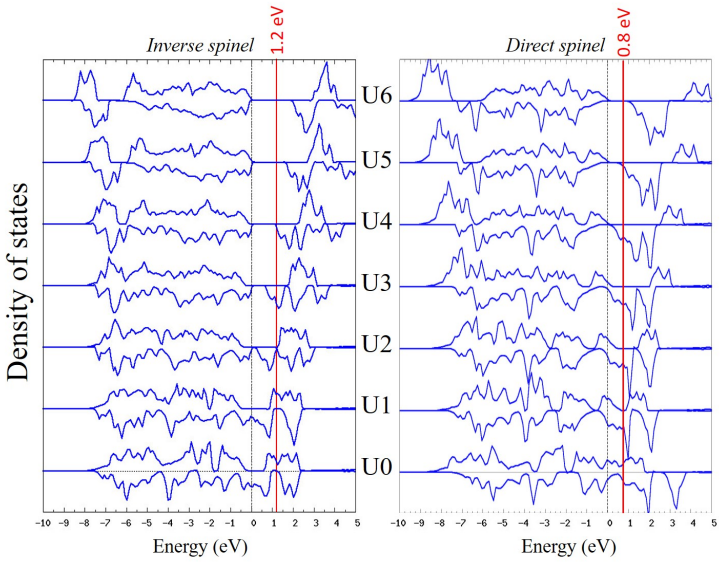

Figure 4.4: Total spin-resolved density of states of inverse (left) and direct (right) CFO for different values of the Fe_d and Co_d effective U. The experimental values (red line) for thin films (1.2 eV) and nanoparticles (0.8 eV) are shown. Positive (negative) DOS represents the majority (minority) spin states.

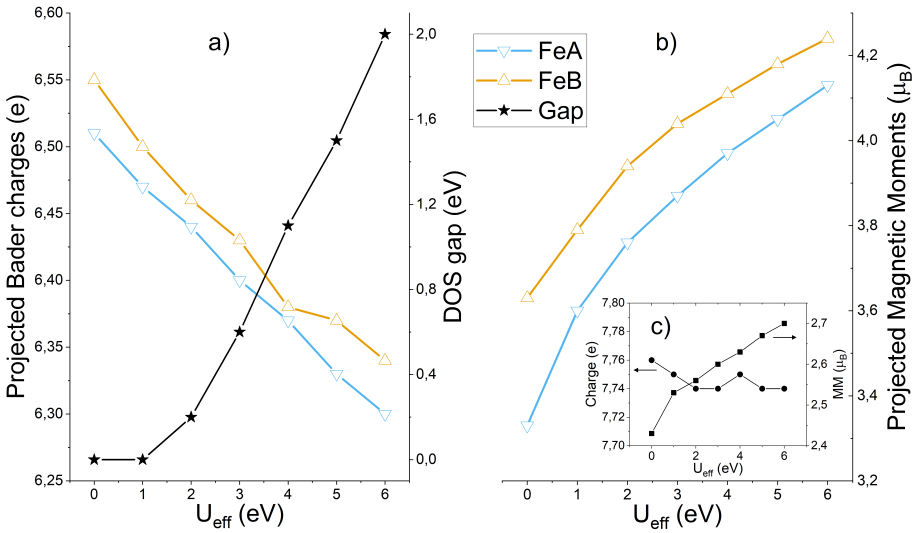

Figure 4.5: *a*) Bader charges and *b*) magnetic moments of A and B iron sublattices at inverse CFO as a function of U. The value of the DOS gap is also shown in *a*). The corresponding Co charge and MM are shown in *c*).

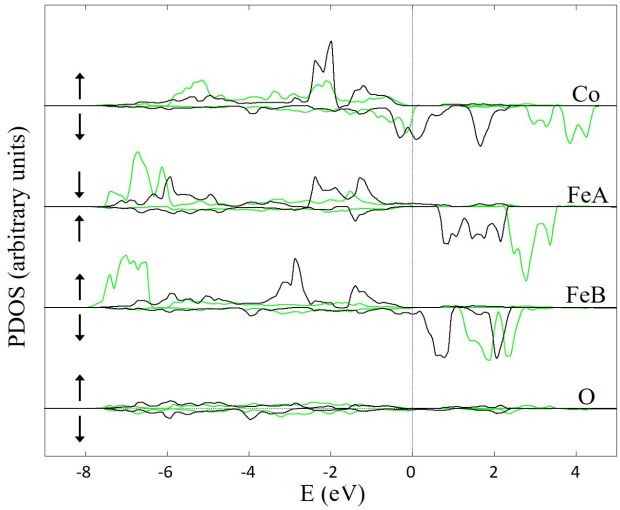

Figure 4.6: *a*) Projected spin-resolved DOS for the different atomic species in CFO under U=0 eV (black lines) and 4 eV (green lines). The majority and minority spin components are plotted on the positive and negative axis respectively. Notice that as Fe_A is coupled antiferromagnetically to the rest of cations, it shows an inversion of the majority/minority spin DOS, identified with arrows on the left side of the figure.

arrangement, selected because it corresponds to the lowest energy configuration and it properly describes the short-range order measured for CFO and NFO [100]. As a result, the cubic symmetry is lowered, with consequences on the magnetic anisotropy. Previous studies [88, 89] have shown that, while the effect is negligible for NFO, the calculated magnetoelastic response of CFO depends on the details of the structure.

According to our self-consistent calculations, the bulk MAE, determined from accurate total energy differences between configurations with different orientation of the magnetization, corresponds to values of $\text{MAE}_{CFO} = 0.6$ meV Fe^{-1}, in close agreement with experimental values [110, 111, 112] It has been obtained by comparing the three cubic symmetry axes [001], [010], [100], and the [110] and [111] directions of the unit cell, and it identifies the magnetic EA as [001], which coincides with that which has been reported in the literature [110].

We have also calculated the bulk MAE of CFO at the direct spinel structure, following the same procedure as that for the inverse spinel. According to our results, the largest energy variations obtained upon different orientations of the magnetization lead to an $\text{MAE}_{CFO_{direct}} = 0.02$ meV Fe^{-1}, which is in close agreement with the experimental evidence of direct CFO being a

	Fe_A	Fe_B	Co
Fe_A	3.63 (4)	3.47 (6)	3.47 (6)
Fe_B		2.96 (2)	2.96 (4)
Co			2.96 (2)

Table 4.2: Nearest neighbours distances in Å and number of nearest neighbor ions (z_{ij}, in parenthesis), for the three CFO sublattices, obtained for the unrelaxed structure at the experimental lattice constant of the inverse form.

soft magnet. The [001] direction is identified as the magnetic EA, although the MAE range is close to our limiting resolution.

4.1.3 Exchange coupling constants

The magnetic exchange constants have been determined following the procedure detailed in section 2.4. We have considered the exchange coupling between the three magnetic sublattices of CFO: Fe_A, Fe_B and Co. The number of neighbors and distances between them are shown in Table 4.2. As we explained in section 2.4, only the nearest neighbors are considered, as the exchange interaction decreases fast with increasing distance. This leads to 6 exchange constants for this material: the 3 inter-sublattice couplings J_{Co-FeA}, J_{Co-FeB}, $J_{FeA-FeB}$ and the intra-sublattice exchange constants J_{Co-Co}, $J_{FeA-FeA}$ and $J_{FeB-FeB}$. These exchange coupling constants have been calculated using eq. (2.37) for different U values. They have also been evaluated using three different lattice parameters around the experimental value in order to see how they are influenced by lattice distortions. Besides, the *static* and *dynamic* limits, defined in section 3.2, have been considered and compared to the values using an ideal unit cell with no ionic relaxation (we call this the *ideal* case) in order to test the robustness of this procedure to extract the Js at CFO. The magnetic configurations considered are shown in Table 4.1, where c0-c3 are used to get the inter-sublattice exchange interactions and c4-c9 are defined splitting the sublattices in order to get the intra-sublattice interactions.

Figure 4.7 shows the dependence of the calculated exchange coupling constants on the value of the Hubbard parameter U obtained for the *static* case using the experimental lattice parameter a=8.38Å. As we mentioned in section 2.4, positive (negative) sign of J represents antiferromagnetic (ferromagnetic) interaction. U$\leq$1eV results in very different J values as compared to larger U values, even finding a change of sign in the intra-sublattice Fe_A-Fe_A

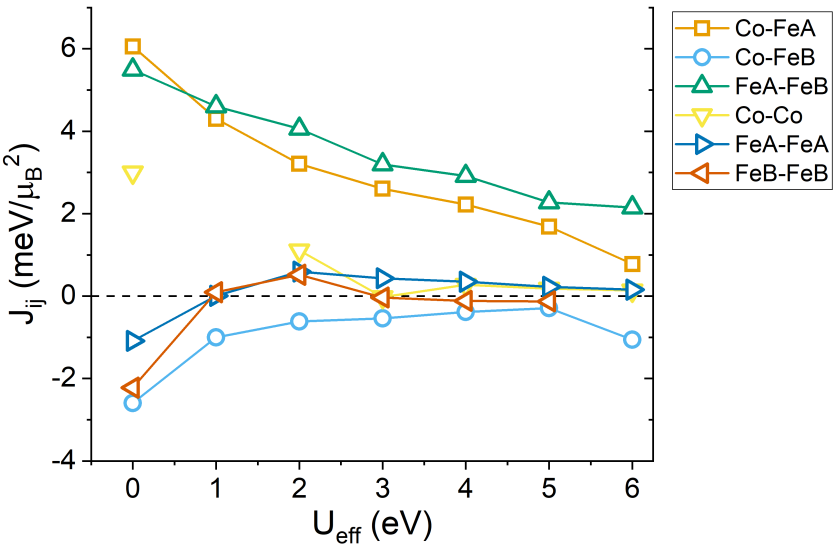

Figure 4.7: J_{ij} dependence on the Hubbard U for the *static* case with lattice parameter a=8.38Å.

and Fe_B-Fe_B interactions. The fact that U=0eV and 1eV represent a metal state of CFO, as shown in Figure 4.4, is indicating that these values are somewhat fictitious, as the exchange interaction occurs between localized electrons in insulators and not between itinerant electrons as found in metals. Thus, we will rely only on the values for U≥2eV, which describe CFO as an insulator. All Js decrease with increasing U, specially the dominant ones, as we found for SFO in section 3.3.2 and in good agreement with the literature [48, 63]. This is again explained by the localization of the Fe and Co *d*-electrons with increasing Hubbard U, which ultimately reduces the interaction between neighboring atoms. The dominant Js are the exchange coupling between tetrahedral and octahedral coordinated atoms J_{Co-FeA} and $J_{FeA-FeB}$. This again can be linked to the Goodenough-Kanamori-Anderson (GKA) rules [21, 22] which states that the superexchange interaction with partially filled *d* orbitals, as it happens to be the case for Co and Fe atoms, leads to a strong anti-ferromagnetic coupling when the bonding angle is 180°, while a bonding angle of 90° usually leads to weaker ferromagnetic behaviour. This is indeed the case, as the octahedral-tetrahedral (J_{Co-FeA}, $J_{FeA-FeB}$) bondings angles are around 124°, while octahedral-octahedral (J_{Co-Co}, J_{Co-FeB}, $J_{FeB-FeB}$) are around 90°. The $J_{FeA-FeA}$ exchange coupling value is close to zero for the whole range of U considered, which relates to the fact that it is not described by the superexchange interaction as there is no oxygen atom mediating, and the distance Fe_A-Fe_A is the largest considered (see Table 4.2).

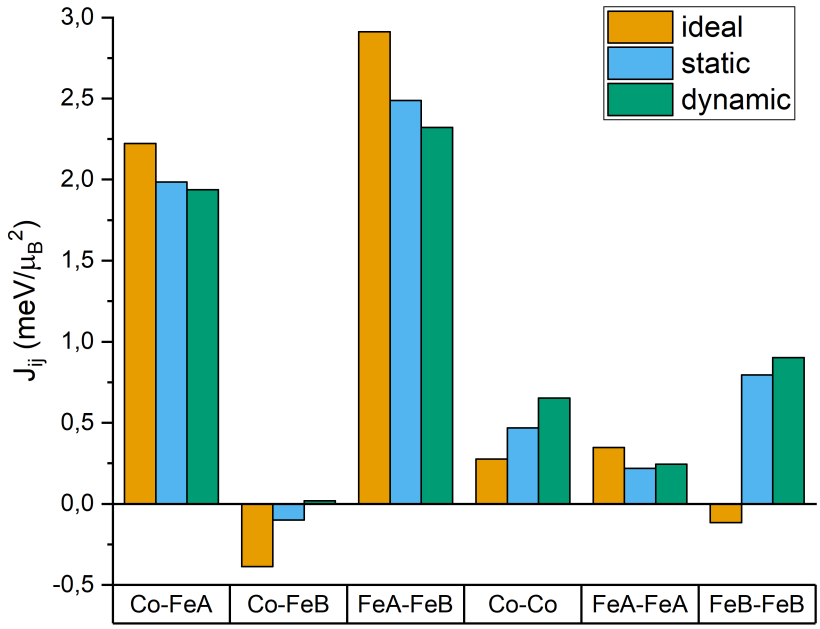

Figure 4.8: Comparison between the exchange constants obtained under the *static* and *dynamic* limits. It is also included the case where the atoms occupy the *ideal* cubic positions.

The results of the comparison between the *ideal*, *static* and *dynamic* cases are shown in Figure 4.8. Here, *ideal* is a specific *static* calculation where we used ideal atomic positions. The dominant exchange couplings are stronger when the atoms are placed in these *ideal* positions, where the Fe_A-Fe_B bond distance is slightly smaller (3.90 Å) than that obtained relaxing the atomic positions (3.92 Å), which, either in a *static* or a *dynamic* way, leads to lower values, with only a slight difference of around 5% for the dominant exchange coupling constants between *dynamic* and *static* limits. But, in general, the hierarchy and relative strengths of all Js are not significantly affected by the detailed atomic structure, supporting the robustness of our approach.

4.1.4 Néel temperature T_N

In the same multi-scale spirit as in section 3.3.3 for SFO, we performed Monte-Carlo simulations in order to derive a value of the Néel temperature of cobalt ferrite at the inverse structure. In this micro-magnetic simulations we employed uniquely the exchange constants and MMs derived from our *static ab-initio* calculations, using a (5×5×5) supercell with only the Fe and Co sublattices. Similarly, the temperature of the system was slowly

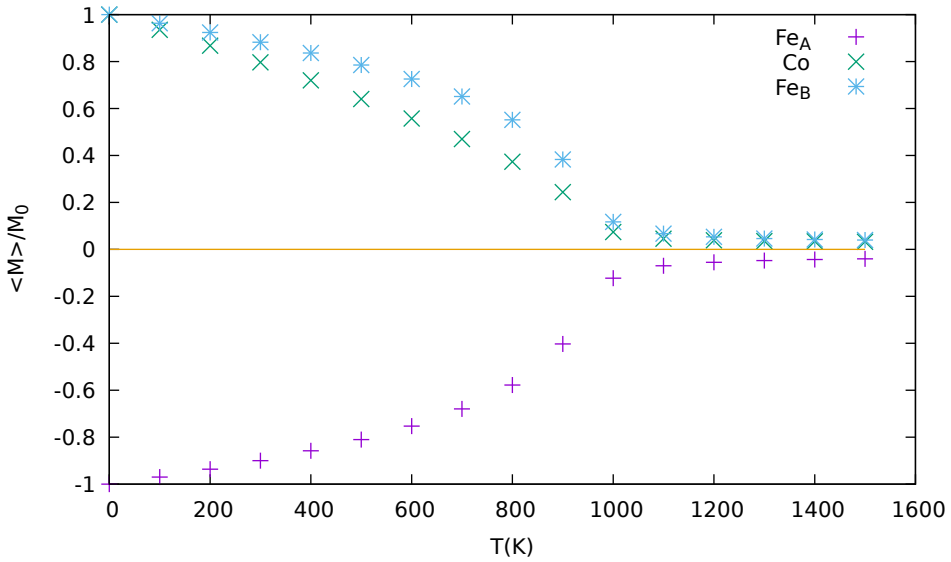

Figure 4.9: Magnetic moments of each sublattice in CFO normalized to those at 0K, as a function of the temperature.

increased from 0K up to 1500K in 20K steps, each of which included 50,000 equilibration cycles followed by another 50,000 time steps. The magnetic moments for U=4eV of each sublattice are shown in Figure 4.9, where we can see that a change from ferrimagnetic to paramagnetic behavior is occurring around 1000K which is larger than the experimental value found around 790K [113]. We also used the Generalized Molecular Field Theory to estimate a Néel temperature of 1042K, which is even larger than the Monte-Carlo prediction, thus concluding that Monte Carlo provides better estimates than GMFT. It is expected that larger U values would be needed in order to recover the experimental Néel temperature value for this system.

4.2 $NiFe_2O_4$ (NFO) and $MnFe_2O_4$ (MFO)

From the point of view of our simulations, NFO and MFO are very similar to CFO. Here we summarize our results, the details of the procedure being explained in the previous section.

As already mentioned, NFO and MFO have been largely studied based on DFT, and the optimized conditions to reproduce the experimental features are well known [88, 89, 100, 114, 115]. In Figure 4.10 we show the evolution of the spin-resolved total DOS of our 28 atoms NFO unit cell as a function of the effective U value applied to the Ni and Fe d orbitals, that we always

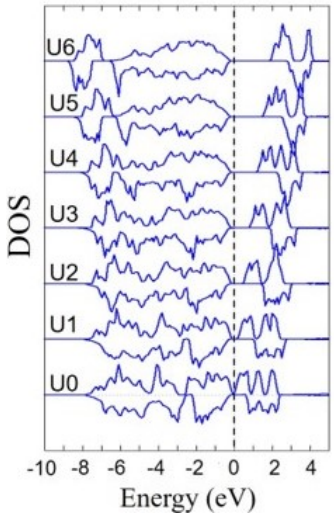

Figure 4.10: Total spin-resolved DOS of NFO for different U(Ni_d, Fe_d) values. Positive (negative) DOS corresponds to majority (minority) spin states.

assign to be same (as mentioned in the introduction of this chapter), the results for MFO being similar. It is evident that the lack of inclusion of a Hubbard term fails to describe the oxide as an insulator, the experimental gap of 1.64 eV [116] being obtained for U= 4-5 eV. Figure 4.11 provides the detailed atomic projections of the NFO and MFO DOS, evidencing the large overlap of the Ni(Mn) and O states, and the localization of the Fe d orbitals at the bottom valence and conduction bands. MFO shows a nearly half-metallic state, in close agreement with previous DFT studies [114], the small gap (close to zero) in agreement with the value of $\approx 0.30eV$ found experimentally [117].

Figure 4.12 shows the evolution of different structural and electronic features of NFO as a function of U, using the experimental cubic lattice parameter a=8.34 Å[118]. We explore different magnetic configurations detailed in Table 4.1 (c0-c3), with Ni instead of Co atoms, following the procedure explained in [119]. The total energies in the top panel evidence that, no matter the value of U, the ground state magnetic order always corresponds to c0, with moderate variations in the energy barriers between configurations. Neither the net magnetization (intermediate panel) has a significant dependence on U for each selected configuration, even though the local magnetic moments (not shown) are enhanced as U increases, reflecting the impact of U on the localization of the d states. Regarding the atomic structure, the bottom panel provides the internal pressure, that goes to zero at the equilibrium volume. The graph shows two features: first, the (non-linear) dependence

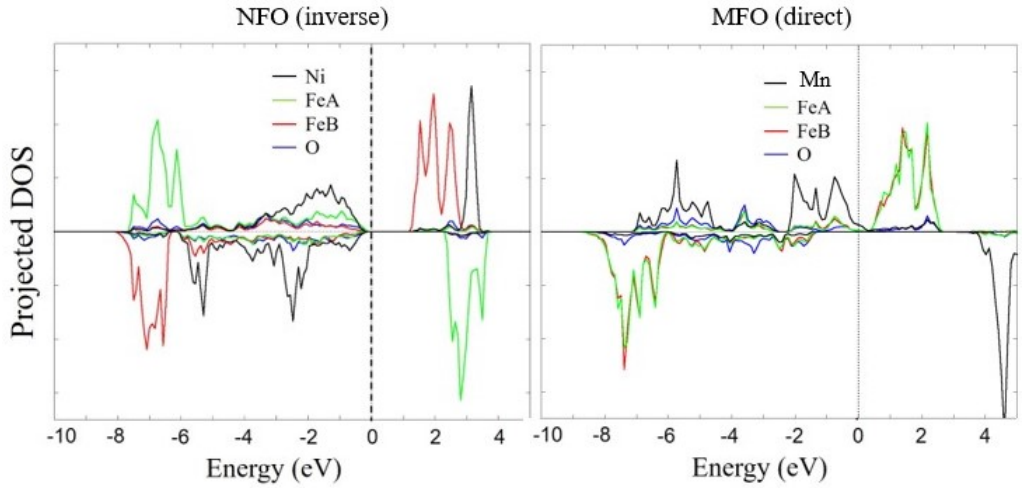

Figure 4.11: Atomic resolved DOS with U=4 eV for the inverse form of NFO (left) and direct form of MFO (right).

of the lattice parameter on U is different at each configuration; this alters the energy barrier between different magnetic orders, that is, the magnetic exchange constants, pointing to the crucial role of U(Ni_d, Fe_d) on the description of the ferrite. Second, restricting to the equilibrium magnetic order c0, our model provides a slightly compressed structure (negative pressure), that better approaches the experimental solution for U values $\geq$ 4 eV. Further relaxation of the structure at U=4 eV under c0 serves us to determine our reference theoretical cubic lattice parameter to be a=8.30 Å for NFO. The inverse spinel structure is also favored over the direct one with an energy difference of $0.26eV/f.u.$ at the optimized lattice structure, which is larger than that obtained for CFO in the previous section. This is in close agreement with the experiments, as NFO shows full inversion [120].

It is worth to remark that a similar study of NFO based on the PBE exchange correlation functional instead of PBEsol, as we did in section 4.1, provides a significantly expanded lattice (a=8.43 Å), evidencing that each GGA parametrization has an opposite effect on the equilibrium volume of the ferrites, while the robust stability of the c0 magnetic order is preserved under all functional forms.

The situation for MFO is very similar. Generally, manganese ions show a high-spin state in which they contribute with $4 - 4.50\mu_B$ to the magnetic moment, close to the $5\mu_B$ moment predicted by the ionic model for Mn^{2+} ions. We have used a Hubbard-like on-site Coulomb repulsion $U_{eff} = 4eV$ for both Fe and Mn ions. Our results are in close agreement to previous

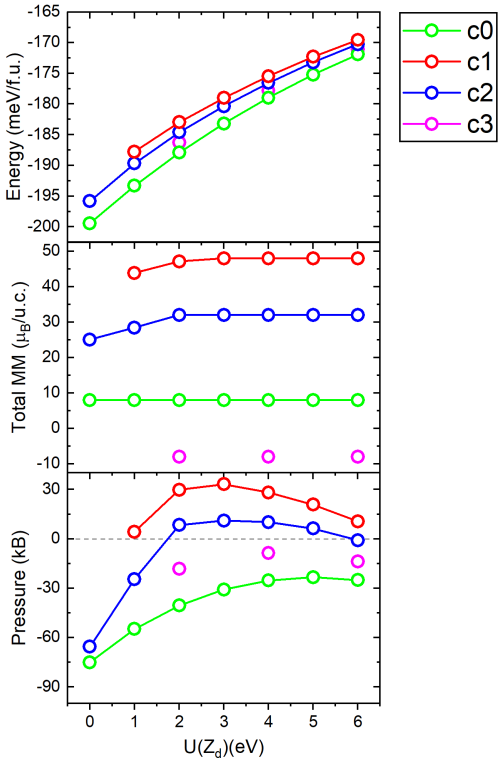

Figure 4.12: Evolution of the total energy (top) and net magnetization per formula unit (middle), together with the internal pressure (bottom) as a function of U(Ni_d,Fe_d) for NFO at the experimental lattice parameter.

theoretical calculations where MFO at direct spinel structure always show a high-spin state, independently of the U_{eff} used in the calculations, and where inverse spinel structure show also a high-spin state for values of U_{eff} greater than 4 eV and a low-spin state for lower values [114, 115, 121]. The lattice parameter at U = 4 eV under relaxation is a = 8.51 Å, close to the experimental value a = 8.50 Å[122]. The degree of inversion of the manganese ferrite found in literature varies depending on the scale of the system: from $\lambda \approx 0.2$ in bulk MFO [123] up to $\lambda \approx 0.8$ in nanoparticles [124]. We obtained an energy difference of $0.12eV/f.u.$, favoring the direct lattice over the inverse one, very close to values found in other theoretical works, $0.13eV/f.u.$ [114]. We should remark here that, when ionic relaxations are not allowed, we found a preference for the inverse lattice with an energy difference of $0.68eV/f.u.$. This will have implications in Chapter 6.

The MAE, determined from accurate total energy differences in configurations with different orientation of the magnetization, corresponds to a value

MAE_{NFO} = 0.001 meV Fe^{-1} for inverse NFO and lower than MAE_{MFO} = 0.005 meV Fe^{-1} for MFO both at inverse and direct spinel structures. These values are close to our resolution. Both NFO and MFO, just as CFO, has the magnetic EA at [001]. The actual EA of bulk NFO has been identified along [111] [125], our result being a consequence of the restriction to a fixed cation distribution; however, we correctly determine the order of magnitude of the MAE, that is negligible compared to that of CFO. These values indicate that both NFO and MFO behave as soft magnets, as it is found experimentally.

We have also calculated an estimation of the exchange coupling constants of both NFO and MFO at inverse spinel structure. Again, the dominant Js are those between tetrahedral and octahedral coordinated atoms, *i.e.* $J_{Ni-FeA} = 3.75meV/\mu_B^2$, $J_{FeA-FeB} = 2.75meV/\mu_B^2$ for NFO and $J_{Mn-FeA} = 1.80meV/\mu_B^2$, $J_{FeA-FeB} = 2.19meV/\mu_B^2$ for MFO, the rest of exchange interactions being below 1 eV. Besides, we looked at the A-B coupling at the direct form of MFO, finding a value of $J_{Mn-FeB} = 2.81meV/\mu_B^2$.

4.3 $ZnFe_2O_4$ (ZFO)

ZFO usually crystallizes in the direct spinel structure, with a cubic lattice parameter of 8.52 Å according to the most accurate experimental determination [126], though values around 8.45 Å are commonly reported [127, 128, 129]. In this ferrite, the lack of magnetic atoms at A sites triggers the competition between different B-B magnetic exchange interactions, leading to a complex magnetic phase diagram where spin-glass behavior, magnetic frustration, and the coexistence of long-range and short-range orders have been proposed [97, 126]. Though recent works support the dominant antiferromagnetic nature of the exchange interactions [94, 98], anomalous ferromagnetism has often been measured, its origin being mainly attributed to the partial inversion reported in ZFO [96, 98, 130, 131], particularly in thin films [132, 133, 134, 135, 136, 137, 138] and nanoparticles [139, 140, 141, 142], and also in other Zn substituted cubic spinel ferrites [143, 144]. In this section, we address the previously unexplored effect of U(Zn_d) on the description of ZFO. In this respect, previous DFT simulations of ZFO [94, 95, 96, 97, 98, 99] have considered different values, from 0 to 5 eV, but without performing a detailed study of its influence on the obtained properties.

Previous *ab initio* calculations of direct ZFO have determined the ground state magnetic configuration, identified as the antiferromagnetic AF2 order represented in Figure 4.13 [97]. Alternative solutions, such as the AF1 also shown in the figure, are very close in energy, justifying the complex magnetic phase diagram and low magnetic ordering temperature. As we mentioned

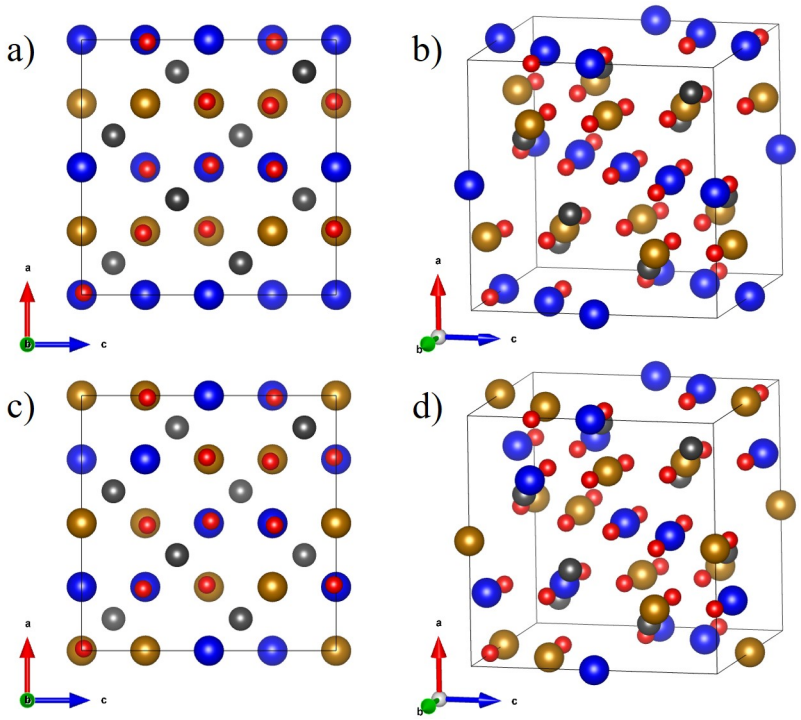

Figure 4.13: Schematic representation of the two different magnetic configurations considered for the direct spinel ZFO, based on a cubic unit cell of 56 atoms: a) and b) correspond to AF1 and c) and d) to AF2. Blue and golden spheres represent Fe atoms with opposite spin orientation, grey spheres Zn atoms, and small red spheres O atoms.

in the introduction of this chapter, the degree of inversion is defined by the parameter λ, that describes the number of B sites occupied by Zn as: $(Zn_{1-\lambda}Fe_{\lambda})[Zn_{\lambda}\ Fe_{2-\lambda}]O_4$, where round and square brackets denote A and B sites, respectively. All previous theoretical results claim the stability of the direct form over the inverse one [94, 96, 98]. Partial inversion favors the local emergence of the ferrimagnetic order typical of CFO and NFO, c0, that becomes the ground state under full inversion. The case λ=1 is also characterized by the sparse distribution of Zn_B atoms, together with the slight contraction below 0.02Å of the lattice parameter as compared to the ZFO direct spinel form [96]. Experiments confirm a higher volume reduction under inversion, with a cubic lattice parameter a=8.38Å for λ=0.5 [142]. Contrary to the large effect on the magnetic order, the band gap and local magnetic moments of ZFO are hardly affected by inversion.

Here we consider the two extreme situations, λ=0 and λ=1, and explore the influence of U(Zn_d) on the structural, electronic and magnetic properties of ZFO. We restrict to the cubic lattice, as we have checked that full lattice relaxation leads to a negligible distortion from cubic symmetry, but the atomic positions are always relaxed. To take into account the magnetic configurations of the direct form, a large cubic unit cell of 56 atoms is used. Figure 4.14 shows the spin-resolved DOS of the direct and inverse spinel structures, each one at the corresponding equilibrium magnetic configuration, under the two limiting U(Zn_d) of 0 eV and 10 eV. We will focus on these extreme U values, after considering intermediate ones that confirm a gradual evolution of the properties of ZFO as a function of U(Zn_d). The figure evidences that the Zn *d* states locate far from the top VB even under U=0 eV, gradually shifting to the core region as U increases. Consequently, the Zn *d* band plays a minor role in the determination of the gap and the distribution of states at the top VB. The moderate variation of the DOS upon inversion, that we obtain for all U(Zn_d), is also in good agreement with previous calculations [96, 98].

Next we explore the energy barrier to ferromagnetism of the different magnetic orders, c0 for inverse ZFO and AF1, AF2 for the direct spinel, based on the experimental lattice parameter of 8.52 Å. The results are shown in Figure 4.15. It is evident that, no matter the U value, the magnetic energy barriers keep essentially unaffected, the ground state magnetic configuration corresponding to the inverse c0 and direct AF2 orders. We have checked that the equilibrium volume is only moderately dependent on the magnetic order, so that the magnetic energy differences are not expected to change upon relaxation of the structures. This low influence of U(Zn_d) on the magnetic properties is also reflected on the local magnetic moments, that keep constant across all U values for each magnetic configuration. The Fe, Zn, O

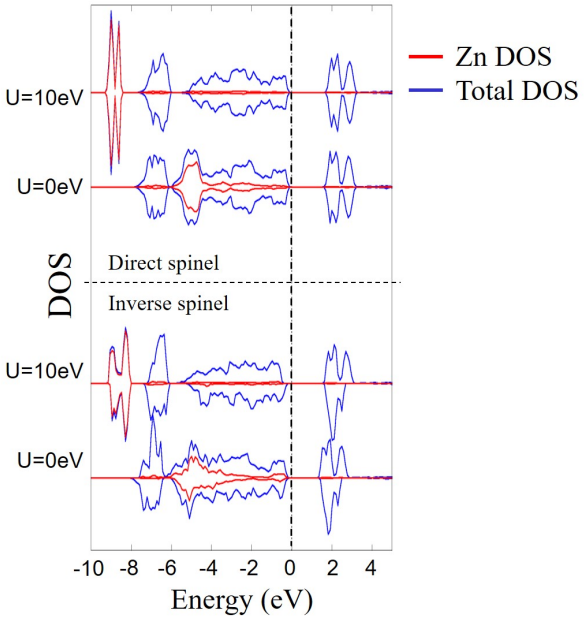

Figure 4.14: Spin-resolved DOS of the direct and inverse spinel forms of ZFO for different U(Zn_d).

magnetic moments in μ_B are respectively 4.21, 0.00 and 0.11 for the direct AF2 structure, and 4.15, 0.05 and 0.02 for the inverse c0 one. These values compare well with both previous calculations and the experimental evidence [96, 128].

On the contrary, the figure reflects that the relative stability of the direct structure over the inverse one gradually reduces as U increases. This result might be further affected by the different equilibrium volumes of both forms, as we are using the experimental lattice of the direct structure. To explore this aspect, we determine the equilibrium lattice parameter of the inverse and direct structures as a function of U(Zn_d), the results are shown in Figure 4.16. From the figure it is clear that the stability of the inverse structure is reinforced when both forms are compared at their equilibrium volume, an effect enhanced the larger the value of U(Zn_d). The figure also evidences that our approach largely underestimates the experimental lattice parameter, particularly under large U(Zn_d). We have performed preliminary calculations without relaxing the atomic positions based on the PBE functional, and as shown in Table 4.3, the agreement with the experimental information is considerably improved. Noticeably, while the volume reduction from λ=0 to λ=1 is lower than experimentally observed, it improves under U(Zn_d)=10 eV, following a similar trend under both exchange correlation functionals.

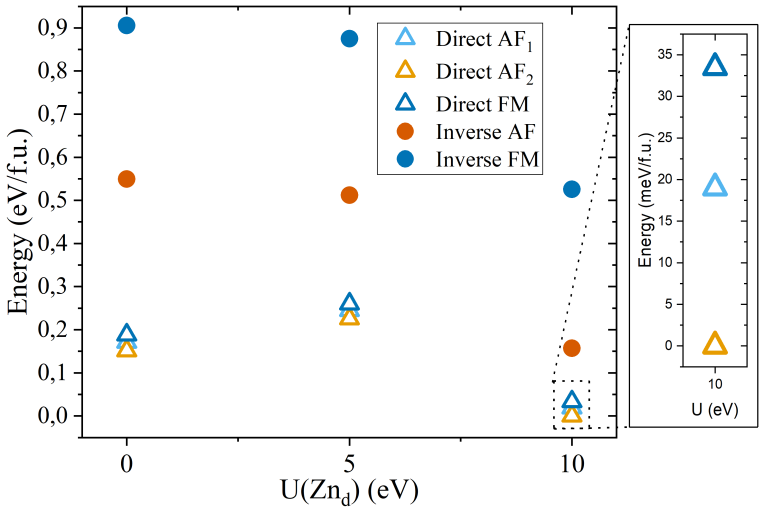

Figure 4.15: Relative stability of the direct and inverse ZFO forms under different magnetic configurations for different U(Zn_d) values. At each fixed U(Zn_d), the energy zero is set at the structure with minimum energy.

λ	PBEsol		PBE	
	U0	U10	U0	U10
0	8.40	8.27	8.50	8.40
1	8.38	8.24	8.49	8.36

Table 4.3: Equilibrium lattice parameter (in Å) of the direct ($\lambda = 0$) and inverse ($\lambda = 1$) forms of ZFO under different exchange correlation functionals for U(Zn_d) = 0 eV (U0) and 10 eV (U10).

But the important point here is that the trend of relative stabilities as a function of U(Zn_d) is not altered by the choice of either PBE or PBEsol. This is proved in Table 4.4, that compiles the excess energy of the inverse structure over the direct one for the different exchange correlation functionals and under different structural conditions. The positive value indicates that the direct spinel is the ground state, and this is the situation in all cases considered. However, the inverse form becomes closer in energy as U(Zn_d) increases, particularly when the structure is allowed to relax.

In Chapter 7, where we are interested in the description of Zn impurities on NFO, a material better described by PBEsol, we will keep the choice of this exchange correlation functional.

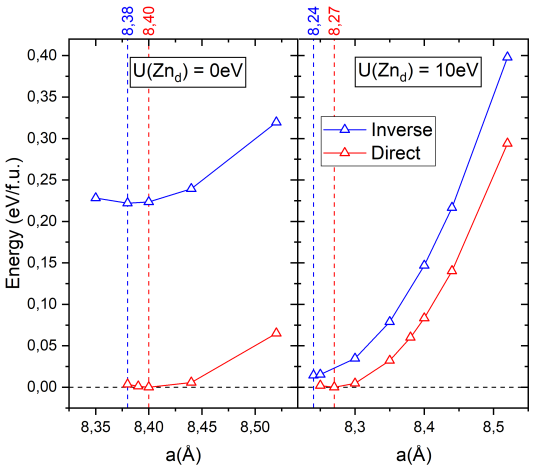

Figure 4.16: Evolution of the total energy as a function of the cubic lattice parameter for the inverse (blue) and direct (red) forms of ZFO at their respective magnetic ground states for U(Zn$_d$)=0 eV (left panel) and 10 eV (right panel). At fixed U(Zn$_d$), the energy zero is set at the structure with minimum energy. In all cases, the atomic positions have been fully relaxed. The vertical dotted red (blue) lines indicate the equilibrium lattice parameter of the direct (inverse) structure.

a	Relax	PBEsol		PBE	
		U0	U10	U0	U10
Exp.	No	0.40	0.16	0.41	0.17
Th.	No	0.39	0.04	0.40	0.11
Th.	Yes	0.22	0.02	-	-

Table 4.4: Energy difference (in eV/f.u.) between the inverse and direct forms under different choices of the exchange correlation functional (PBE or PBEsol), the lattice parameter a (the experimental value of 8.52 Å or the equilibrium values in Table 4.3) and the structural conditions (relaxation or not of the atomic positions) for U(Zn$_d$) = 0, 10 eV.

4.4 Conclusions

We have revisited the electronic structure of cubic spinel ferrites, focusing on the influence of the Hubbard U term on the description of their structural, electronic and magnetic properties. In good agreement with previous knowledge, the choice of U has a large influence on the final results, while a

value around 4 eV applied to the d band of the magnetic cations describes satisfactorily the main features of these oxides: a band gap close to experiments, a balance between the inverse and direct structures that matches the experimental evidence, and a reasonable description of the lattice volume.

Concerning the magnetic properties, the robust stability of the ferrimagnetic ground state and the high magnetization of CFO, NFO and MFO are much less dependent on U, provided it is over a threshold value of 2 eV. We have also determined the magnetic exchange constants based on a mapping to a simple Heisenberg Hamiltonian, as described in section 2.4. Again the choice of U has a large influence of the exchange interactions, but values over 2 eV guarantee the correct hierarchy of the exchange constants and certain stabilization of the individual values. Also important is the cation distribution, particularly for CFO, that further affects the computed magnetocrystalline anisotropy. On the other hand, neglecting variations of the atomic positions and magnetic moments at the different magnetic configurations has a minor influence on the determination of the exchange constants. As observed for SFO, the Néel temperature derived from these exchange interactions is more accurately described by Monte Carlo simulations than by simpe GMFT methods.

Regarding ZFO, we have made a pioneering study of the influence of U on the Zn d band. While it plays a minor role in the description of the electronic features at the top valence band, it is crucial to determine the relative stability between the inverse and direct spinel forms, which has important consequences on the magnetism of the final system. On the other hand, the description of the structure and magnetism of each of the spinel forms is not significantly affected by this value of U, with a unique definition of the magnetic ground state and moderate variations of the lattice parameter. Except for the lattice volume, these conclusions are also independent of the choice of the particular GGA parametrization. However, the choice of PBEsol that better describes the magnetic cubic ferrites considered here provides a low lattice volume for ZFO, that improves upon use of PBE.

Chapter 5

CFO/NFO interface

5.1 Introduction

Hard and soft spinel ferrites are used in bicomponent systems for permanent magnet applications. In these mixed systems, important effects such as strain or structural defects usually arise. Core/shell CFO/NFO nanoparticles of high structural quality have already been prepared by hydrothermal methods [145], the magnetic measurements evidencing a coherent interface and a good exchange coupling between both components, while the saturation magnetization and the magnetic anisotropy of the entire system lie between those of the individual materials. This has its origin in the similarity between the electronic properties, magnetic order and lattice structure of these two specific oxides, which allows us to isolate the effect of ideal interface formation on the magnetism of the combined system based on density functional theory. Here we address the detailed description of the magnetic properties of the (001) and (111) interfaces between CFO and NFO.

As already shown, CFO and NFO share the same crystal structure with close lattice parameters, reducing mismatch and strain effects, and thus provide an ideal model to explore intrinsic features linked to the formation of the interface. These ferrites also share the same ferrimagnetic order, with tetrahedral and octahedral cation sublattices coupled antiferromagnetically, preserving high values of the local magnetic moments. Also, their electronic features are quite similar, with insulating band gaps and akin orbital distributions. As expected from the relative stability between the inverse and direct spinel structures of the bulk counterparts [100], already shown in Chapter 4, NFO is completely inverted, while some Co cations occupy tetrahedral sites. This is relevant as CFO in the direct spinel lattice behaves as a soft magnet. Thus, in this chapter we will consider CFO/NFO interfaces combining

inverse NFO and both direct and inverse CFO.

5.2 Methods

Following Chapter 4, we have performed *ab initio* simulations based on the DFT using VASP. Here, the PBEsol parametrization has been chosen as the generalized gradient approximation for the exchange–correlation functional, as it was concluded in Chapter 4 that this gives in general a better description of these materials. Similarly, a Hubbard U=4 eV is used at the *d* bands of the three cations: Fe, Co and Ni. The rest of the calculation conditions, *i.e.* the cutoff for the plane waves basis set, the k-mesh for sampling the Brillouin zone and the convergence of the electronic relaxation are those already indicated in the previous chapter. We should mention here that the 3D periodic boundary conditions are not perfectly suitable to describe the interface: we are restricted to a fixed 2D lattice parameter, and the infinite periodicity along the normal to the interface leads to the modeling of a superlattice instead of an isolated interface. There are several ways to circumvent these problems. To compensate the common 2D lattice, we fix it to the bulk value of one of the oxides, and explore for the other the out-of-plane lattice parameter that compensates the volume minimizing the energy. In the present case of CFO/NFO interfaces, with close lattice parameters, it is enough to fix the lattice to one of the oxides. When more dissimilar materials are combined, as shown in the next chapter, different 2D lattices corresponding to the extreme cases need to be considered. Regarding the super-periodicity along the normal to the surface, we can avoid its influence on the local interface properties by choosing thick enough oxide slabs. Care needs to be taken when considering integrated quantities such as the total energy, that contains information from multiple interfaces.

We have also explored the magnetic anisotropy of the combined system, calculating the MAE from both methods described in section 2.3: total energy differences with the magnetization along high symmetry directions, and the magnetic constraints method. In this method we included configurations with the magnetization along the relevant symmetry directions of the systems considered (bulk easy axis (EA), interface normal and in-plane directions). As we already mentioned, this method departs from the accurate calculation of an initial configuration, forcing the local magnetic moments to rotate at subsequent steps by imposing a penalty contribution to the total energy that keeps the moments at the desired orientation. Thus, subsequent steps may suffer from cumulative accuracy loss, leading to final results dependent on the choice of the starting configuration. This can be controlled through

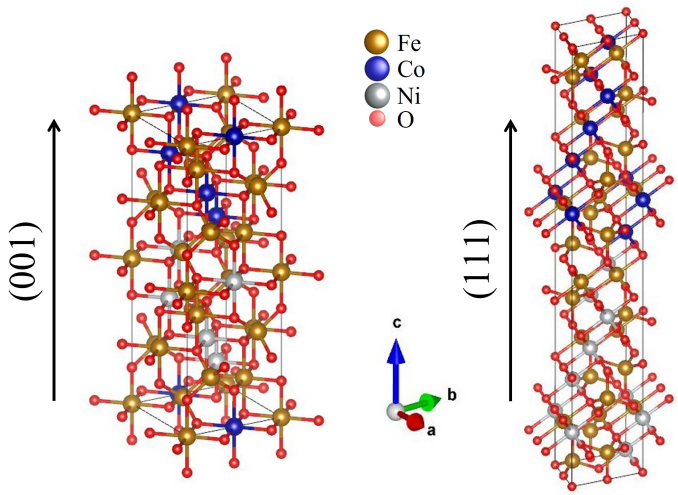

Figure 5.1: Unit cells of the CFO/NFO interface for the two different high-symmetry directions [001] and [111].

the careful choice of the penalty contribution. Figure 5.2 proves the independence of our results on the choice of the initial magnetization direction at the [111]c interface, showing the path with the worse reversibility among all considered by us. Our ability to perform this check also relies on the negligible magnetic chirality of the systems under study. In chiral systems, additional differences may emerge depending on the rotation sense, either clockwise or counterclockwise.

Figure 5.1 shows the ideal CFO/NFO under study along two high-symmetry directions [001] and [111]. As CFO and NFO have close lattice parameters, the in-plane mismatch is <0.5%, well below the threshold to introduce any noticeable strain effect in the electronic, optical or magnetic properties of any of the oxides [88, 89, 146, 147, 148]. We have considered the case in which NFO adopts the in-plane CFO lattice (that is, $a_{NFO} = a_{CFO}$ and $b_{NFO} = b_{CFO}$), optimizing the corresponding c_{NFO} from bulk calculations of NFO at fixed in-plane CFO lattice parameters. We have also restricted our study to uniform distributions of Co and Ni, as this is known to be the most stable solution for both oxides [100]. In all cases, the atoms around the interface have been allowed to relax until the forces were below 0.004 eVÅ^{-1}. This includes two Fe planes on each side of the (001) interface and two planes (one formed by Fe and one by O) on each side of the (111) interface, as can be seen in figure 5.3.

Along the [001] direction, a natural interface emerges at the plane defined by the tetrahedral Fe cations. We have considered this situation using a

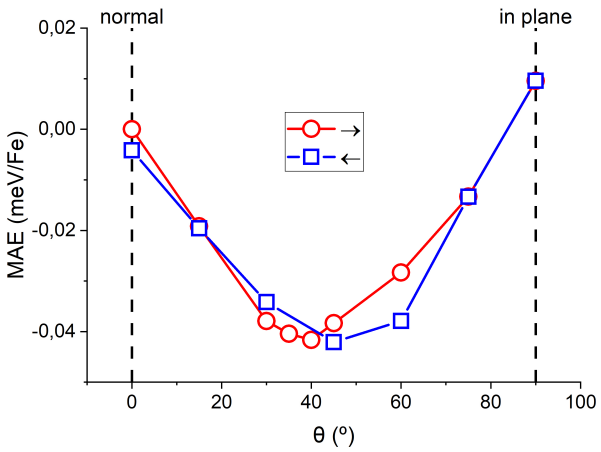

Figure 5.2: Evolution of the MAE under stepwise rotation of the magnetization for the CFO/NFO [111]c interface, starting either from $\theta = 0°$ (red circles) or from the in-plane [-101] axis (blue squares).

minimum unit cell with 56 atoms that corresponds to eight atomic layers of each oxide, and the CFO lattice parameters, a = b = 5.93 Å, and values of c_{CFO} = 8.38 Å and c_{NFO} = 8.21 Å. When we increase the unit cell to 84 atoms the interface properties do not change and the conclusions reported here remain valid. Along the [111] direction we have employed a unit cell with 84 atoms, six planes for each oxide, again choosing the in-plane lattice parameters of CFO, a = b = 5.94 Å, and values of c_{CFO} = 14.40 Å and c_{NFO} = 14.25 Å. Here, as shown in figure 5.3(b), the choice of the terminations that match at the interface is not unique. The three inequivalent interfaces that emerge can be understood regarding the inverse spinel structure as an ABC stack of oxygen layers, each one with a different environment of cation neighbors.

The relative stability of the different interfaces has been estimated from the work of separation (W_{sep}), defined as the energy needed to break the interface and separate the two oxides [149]. We have calculated it from the energy difference between the isolated oxides, obtained by introducing a vacuum region of 10 Å in our slabs at the interface between the two materials, and the bicomponent system after relaxing the atoms around the interface, normalized to the surface area of the unit cell. Thus, positive values of W_{sep} correspond to stable interfaces.

A final remark is deserved about the partial conversion of CFO to the direct spinel lattice. As seen in section 4.1 and 4.2, NFO is found to be purely at the inverse spinel structure, while CFO can be only partially inverted.

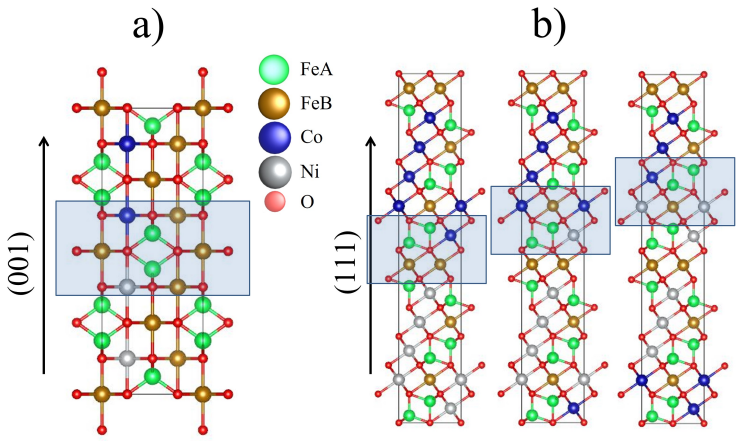

Figure 5.3: Interfaces considered along a) (001) and b) (111) orientations. The blue boxes indicate the interface region where atoms are allowed to relax. Fe_A (Fe_B) distinguishes tetrahedral (octahedral) Fe sites.

Table 5.1: The energy difference in eV/f.u. between ferromagnetism and the ferrimagnetic ground state for bulk NFO, bulk CFO and the NFO/CFO (001) and (111) interfaces, both under the inverse and direct spinel structures of CFO.

System	NFO	CFO	(001)	(111)
Inverse	0.87	0.75	0.82	0.85
Direct	–	0.24	0.68	0.65

In our interfaces, we have modeled the extreme situation where the entire CFO is considered as a direct spinel structure, with all Co atoms replacing Fe_A. This provides a limiting case that maximizes the effect of inversion of CFO. The equilibrium lattice parameters of bulk CFO under the direct spinel structure (a = b = 5.94 Å and c = 8.40 Å using a (001) cell) are close to those of the inverse spinel. Thus, we do not expect any strain effect induced by the incomplete inversion of CFO, and we have used the inverse spinel lattice parameters in our calculations.

5.3 Results and discussion

5.3.1 Magnetic order and magnetization

Interface formation alters the bonds between atoms, modifying both the local magnetic moments and the balance of magnetic energies. As a result, it may lead to changes in the magnetic order and the net magnetization of the system. We have addressed these issues first by simulating different magnetic configurations at the interfaces under study. We explore possible deviations from the bulk ferrimagnetic order in both oxides, and relate them to the exchange constants determined from mapping our ab initio total energies to a Heisenberg Hamiltonian [48]. It is worth mentioning that some of the proposed configurations do not even converge to a selfconsistent ground state within our accuracy limits, providing a hint of their instability. Our final results indicate that in all cases the bulk-like ferrimagnetic order is preserved. As an example, table 5.1 compiles the energy differences between the ferrimagnetic ground state and the ferromagnetic configuration, comparing the isolated bulk oxides to the interface systems under study. The quoted values for (111) interfaces correspond to the average of the different terminations; the ferromagnetic case did not converge to a ground state in all cases, but differences between the converged solutions remain below ± 0.05 meV Fe^{-1}. All these results indicate a good exchange coupling between both oxides, that favors avoidance of spring magnets. The partial inversion of CFO will not change this scenario, as the same ferrimagnetic order is stabilized in bulk CFO under the direct spinel structure.

Regarding the exchange constants between the different magnetic sublattices (J_{ij}), the magnetic configurations necessary to determine them in the bulk forms of CFO and NFO are described in Table 4.1. The number of configurations required in the bicomponent systems is much larger, even at the (001) interfaces, due to their reduced symmetry. Only the magnetic exchange between Fe_A and Fe_B sublattices can be determined from the configurations c0-c3 used at the bulk, allowing us to compare the interface value, $J_{Fe_A-Fe_B} = 2.8$ meV$\mu_B{}^{-2}$, to those obtained in the bulk forms of both CFO and NFO: $J_{Fe_A-Fe_B} = 2.5$ meV$\mu_B{}^{-2}$.

As an additional proof of the minor influence of the interface on the exchange interactions, in Figure 5.4 we compare the energies of configurations c0-c3 at the bulk and the (001) interface. It is clear that the energy barriers between configurations follow identical trends in all cases. Moreover, the interface values are approximately the average of the bulk ones, evidencing that the energy contributions to the magnetic exchange interactions are hardly affected by the presence of the interface. The other relevant terms

taking part in the determination of the J_{ij} are the sublattice magnetizations. Our calculations indicate that, for each specific configuration, similar values of the local magnetic moments are obtained at the bulk and interface systems.

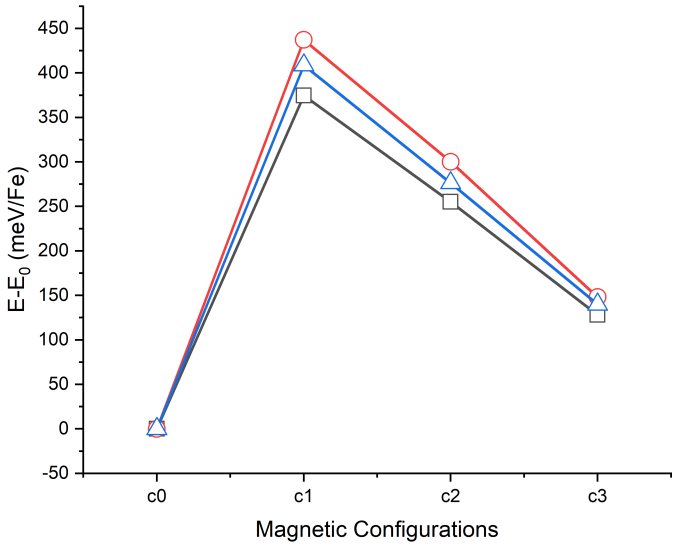

Figure 5.4: Total energy of the magnetic configurations c0-c3, described in Table 4.1, for the bulk forms of CFO and NFO, and the (001) interface. Pink squares accounts for bulk CFO, red circles for bulk NFO and blue triangles for CFO/NFO interface energies. The energy zero for each system is set at the ground state magnetic order, c0.

In the following we will thus restrict to the bulk-like ferrimagnetic order of the oxides. Table 5.2 provides the total magnetization and the cation magnetic moments corresponding to all interfaces under study. Both the inverse and direct forms of CFO are considered, distinguished labelling with a prime systems containing direct spinel CFO. As a reference, also bulk values are provided. Though not shown in the Table, the Ni moments are not modified far from the interface, even though NFO adopts the in-plane CFO lattice. Regarding now the upper part of the Table, referred to full inverse spinel structures, the Co and Ni moments hardly show any variation with respect to the bulk, while interface Fe moments are closer to the values at CFO. Still, all interface systems preserve magnetizations that correspond to the sum of the individual bulk components, evidencing that interface formation does not have any impact on it.

Larger variations occur when we consider the direct spinel CFO. As ferrimagnetism in the spinel ferrites emerges from the antiferromagnetic coupling

System	M	Fe_A	Fe_B	Co	Ni
CFO bulk	3	4.06	4.17	2.65	–
NFO bulk	2	4.00	4.12	–	1.60
(001)	5	4.07	4.17	2.66	1.62
$(111)_a$	5	4.06	4.18	2.64	1.61
$(111)_b$	5	4.07	4.18	2.65	1.60
$(111)_c$	5	4.07	4.18	2.65	1.62
CFO' bulk	7	–	4.19-4.32	2.59	–
(001)'	8.5	4.07	4.03-4.19	2.54	1.63
$(111)'_a$	8.8	–	4.20-4.22	2.60	1.64
$(111)'_b$	8.8	4.06	4.17-4.19	–	1.61
$(111)'_c$	8.8	–	4.23	2.59	1.64

Table 5.2: Net magnetization of our slabs (M, in μ_B/f.u.) and absolute value of the magnetic moment (in μ_B) of the interface cations (i.e. those included in the blue boxes of Figure 5.3), for the systems under study. The upper (lower) part of the table refers to the inverse (direct) CFO form.

between octahedral and tetrahedral cations, replacing Fe_A by Co leads to a significant enhancement of the net magnetization. Similarly, the Fe_B moments increase, and show a noticeable dispersion of values. These features observed in the bulk form of direct CFO are also evident at the interfaces. In general, the interface Ni moments tend to slightly increase, but the net magnetization is moderately below the sum of the bulk contributions. We can conclude that interface formation does not modify the magnetization of the oxide components in the absence of defects, but a local enhancement may arise from partial CFO inversion due to the replacement of Fe by Co at tetrahedral sites while preserving the ferrimagnetic order.

5.3.2 Stability

The relative stability of the (111) interfaces under study can be determined from direct comparison of their total energies, as their unit cells share the same composition. This serves to identify case (111)c as the most stable solution, with the (111)a and (111)b ground states higher in energy by 7.18 meV/f.u. and 7.27 meV/f.u., respectively. When direct CFO is considered, the energy differences are enhanced and their relative order is modified: (111)a' becomes the most stable case by 1.9 meV/f.u. over (111)b' and by 23.53 meV/f.u. over (111)c'. On the other hand, regarding the relative stability between direct and inverse spinel structures, the interface does not

introduce any significant difference with respect to the bulk, with energy barriers that oscillate between 0.55 eV/f.u. and 0.49 eV/f.u. Specifically, the energy barrier between (111)c and (111)a', which are the most stable interfaces for inverse and direct CFO respectively, is 0.50 eV/f.u. All this supports that the interface will not favor neither inhibit the occupation of tetrahedral positions by Co atoms.

To compare now all orientations, we resort to the work of separation, shown in Figure 5.5 also including the direct CFO lattice for all cases. The positive value of W_{sep} reflects the stability of all systems, and again identifies the (111)c termination as the most stable situation. Mutual differences between the (111) terminations are slight, and much less than referred to the (001) orientation, as expected from their close-packed structure. When the direct CFO spinel is considered, case (111)c' does not follow the trend of variation obtained from direct comparison of the total energies, although the order of magnitude of the relative stabilities is low and similar under both methods. In summary, the main conclusion from this study is that a coexistence of all the interfaces considered cannot be discarded in most experimental systems where no specific orientation is favoured, as magnetic powders and nanoparticle solutions.

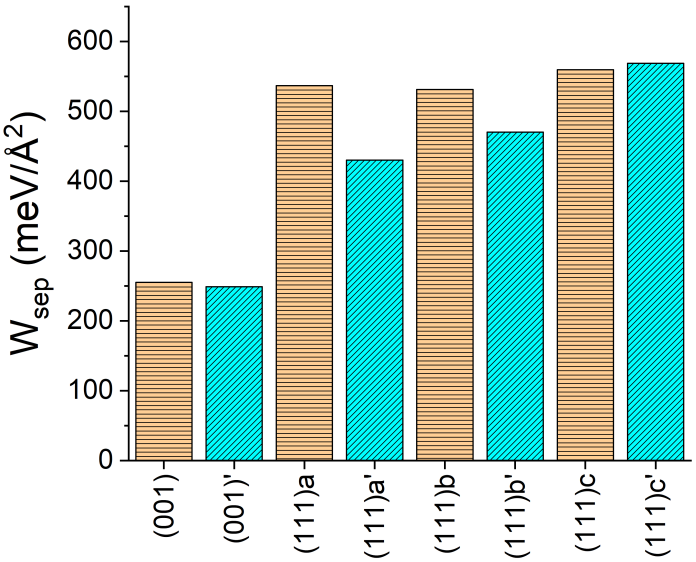

Figure 5.5: Work of separation for the different interfaces considered, including also the direct CFO lattice (cases labelled with a prime).

5.3.3 Magnetic Anisotropy

As shown in sections 4.1 and 4.2, the bulk forms of both CFO and NFO have cubic symmetry, related to a random distribution of cations at the octahedral sites. Considering different Co distributions at the interfaces under study is a formidable computational task. In Section 6.2 we will address a first approach, exploring two different Co cation arrangements that lie among the most frequent distributions. As we will show, the specific Co distribution can change the easy axis direction, although moderately in a non-distorted environment like the one we are dealing with in CFO/NFO case. Our results represent a first approach to explore the global effect of interface formation on the magnetic anisotropy of the combined system. Even though they are necessarily restricted to our choice of a specific model, they are still representative, as the variations introduced by different configurations are expected to lie within the experimental uncertainty [89].

Here, we explore the evolution of the MAE for gradual rotations of the magnetization departing from the bulk EA, based on the magnetic constraints method. Even though this method is less accurate than the total energy differences method, it gives more interesting information as the symmetry of our system is complex and cannot be fully described based on the bulk crystal axes. Following the path indicated in Figure 5.6a, we have first applied the magnetic constraints method to bulk CFO, and the results are shown in figure 5.7. The MAE increases smoothly as the magnetization rotates from the bulk EA to the plane normal to it, where it reaches the same maximum value obtained for the other in-plane high symmetry axis, [010] and [100]. This supports a low magnetic anisotropy in the plane normal to the EA at bulk CFO in our model without cubic symmetry.

The presence of the interface introduces new relevant symmetry directions that depend on the specific termination. In the (001) CFO/NFO system, the interface normal coincides with the CFO bulk EA [001]. If we determine the MAE from direct energy differences between situations where the magnetization is aligned either to the interface normal or to any in-plane direction, we obtain a value of 0.22 meV Fe^{-1}. This is close to a simple additive effect from both oxide components, that would correspond to 0.3 meV Fe^{-1}, the presence of the interface only slightly weakening the anisotropy.

The situation is different for (111) terminations. Here, besides the interface normal and in-plane directions, we need to consider the bulk EA as a relevant reference. Figure 5.7 shows the evolution of the MAE at the (111) interfaces as the magnetization rotates from the interface normal to an in-plane direction, following the path indicated in Figure 5.6(b). In all cases the bulk EA is preserved, with a MAE around 0.3 meV Fe^{-1} when

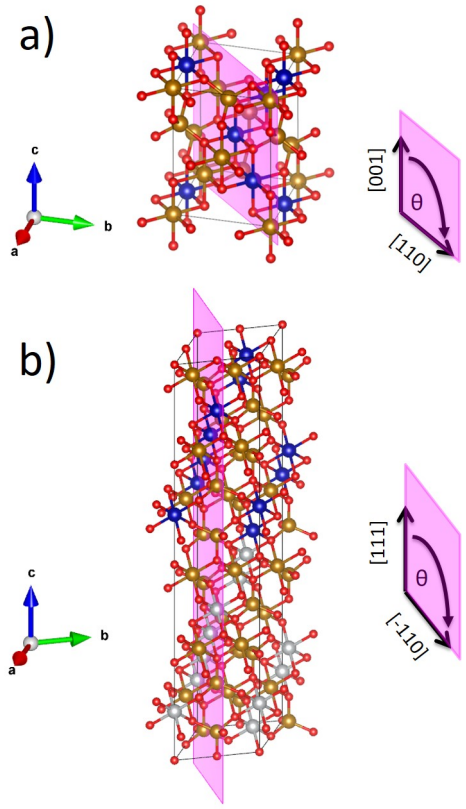

Figure 5.6: Rotation paths followed in Figure 5.7 for: CFO bulk and NFO/CFO (111)a,b,c interfaces. In both cases, the magnetization vector is contained in the depicted planes. At the interface, the [111] and [-110] axis coincide with the normal and in-plane directions, respectively.

comparing the same crystal directions than for the (001) interface (namely, [111] and [-110]). This seems to again reflect a simple additive effect of the bulk contributions, but without any further anisotropy weakening. Figure 5.7(b) also allows us to compare the difference between situations where the magnetization is aligned either in-plane or normal to the interface. Here, significant variations emerge between the different (111) terminations: while for (111)c aligning the magnetization to the normal increases the MAE by 0.1 eV atom^{-1} over the bulk EA, this MAE doubles in the (111)a interface. This effect is related to the choice of the specific in-plane direction, as we will explain now.

Figure 5.8 shows the MAE when comparing different in-plane directions at the (111)c interface, referred to as the in-plane orientation that minimizes the energy. The maximum variations are similar to those encountered between

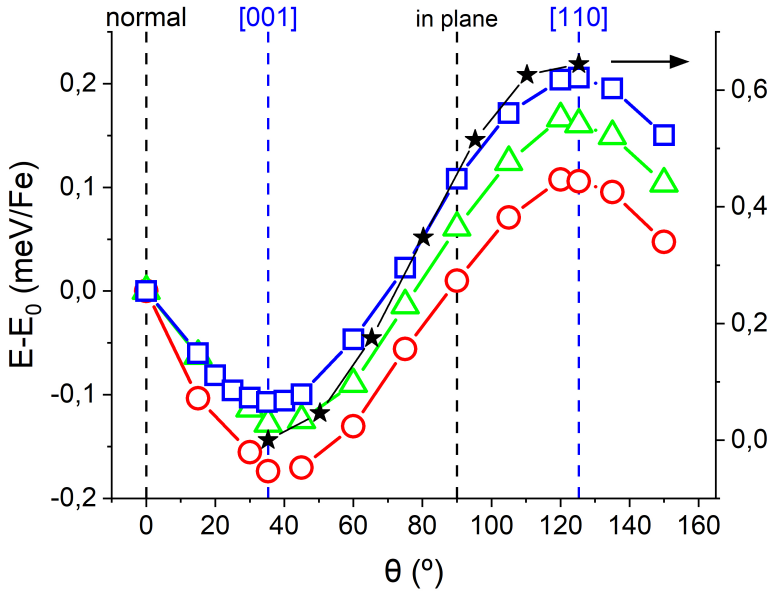

Figure 5.7: Evolution of the MAE under stepwise rotation of the magnetization following the path shown in Figure 5.6 for bulk CFO (black stars), departing from the bulk easy axis [001]; CFO/NFO (111)a,b,c interfaces (red circles, green triangles and blue squares respectively), departing at $\theta = 0°$ from the interface normal. As a reference, the values of θ corresponding to relevant symmetry directions are indicated by dashed lines.

the interface normal and the [-110] axis in figure 5.7. A similar situation arises at the other (111) terminations. The bulk EA always provides the lowest energy.

All these results indicate that interface formation, even for these ideal interfaces lacking mismatch and defects, tends to reduce the MAE of the bicomponent system compared to the isolated hard material: a drawback to improving the energy product of a permanent magnet based on the multicomponent system. But in addition, in samples where multiple terminations coexist, the rotation of the magnetization along a fixed path (i.e. from normal to in-plane directions) faces different energy barriers depending on the termination, complicating the interpretation of experimental results. As interface formation does not introduce any significant changes either in the local charges or in the magnetic moments, the effect seems to be related to crystal-field effects beyond nearest neighbors that are also behind the influence of the particular cation distribution on the magnetic anisotropy.

Finally, we have considered the influence of partial inversion of CFO and

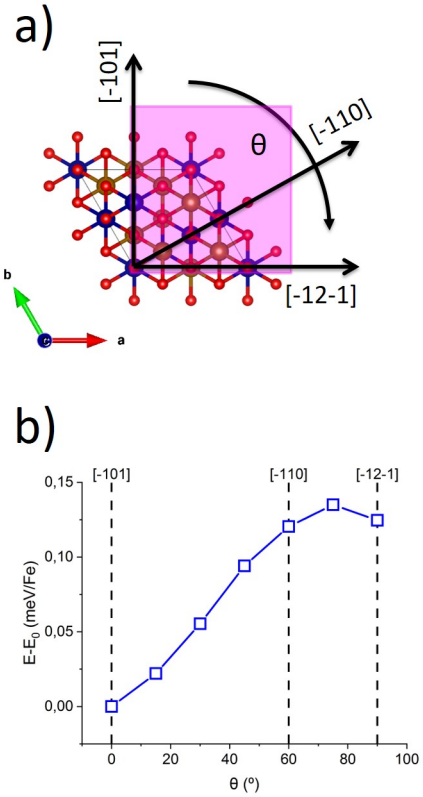

Figure 5.8: (a) The in-plane rotation path of the magnetization and (b) the resulting MAE, for the (111)c interface. The energy zero is set with the magnetization aligned to [-101].

strain in the MAE. As shown in section 4.1, bulk CFO under the direct spinel structure (CFO') is a soft magnet, so that introduction of direct CFO in the interface systems is expected to reduce their magnetic anisotropy. The evolution of the MAE following the path shown in figure 5.6(a) is similar for CFO', though it spans an energy range 30 times lower. Again, the [001] direction is identified as the magnetic EA, but the MAE range is close to our limiting resolution. When replacing CFO with CFO' in our interface systems, we have considered gradual rotations of the magnetization from out-of-plane to in-plane directions, exploring different in-plane orientations. The resulting MAE is very low, close to our accuracy limit, indicating that interface formation does not alter the magnetic softness induced by inversion of CFO.

Regarding strain effects, due to the excellent lattice matching of both oxides, we do not expect any noticeable influence of strain in our CFO/NFO

systems. However, in our calculations NFO adopts the CFO lattice, while, depending on the growth conditions, the reverse situation may be found. Taking into account the large magnetostriction of CFO, even this slight mismatch might be important [89]. We have carried out a preliminary study to address how adopting the NFO lattice parameters modifies the MAE of bulk CFO. The results provide a MAE similar to that obtained under the CFO bulk lattice, 0.61 meV Fe^{-1}, that reduces slightly to 0.58 meV Fe^{-1} after optimization of the c lattice parameter while keeping a_{NFO}, b_{NFO}. In both cases the bulk EA does not change. The slight reduction of the MAE when strain relief is allowed matches the expected trend from the magnetoelastic coefficient of CFO under constriction mismatch [89]. However, the low effect confirms the validity of our approach to neglect the impact of strain in the CFO/NFO interfaces.

5.4 Conclusions

A detailed study of the magnetic properties at ideal CFO/NFO interfaces has been presented, including effects induced by the conversion of CFO to the direct spinel structure. As expected, close-packed structures are more stable, though interfaces along different orientations may coexist. The bulk magnetic order is preserved, without influence from either strain effects in the expected limits induced by mixing NFO and CFO, or from partial conversion of CFO to the direct lattice. Similarly, ideal interface formation does not modify the magnetization, which corresponds to the sum of the individual bulk components. Actually, partial inversion of CFO has a much larger impact on the magnetization, significantly enhancing it. Nevertheless, the presence of the interface does not seem to influence the ratio of Co atoms at tetrahedral sites. A different scenario emerges regarding the magnetic anisotropy. The presence of the interface tends to weaken the net MAE of the bicomponent system, due to an additive effect of contributions from the soft and hard materials. Additionally, the MAE is affected by the particular terminations involved. While the bulk EA is preserved, the cost to rotate the magnetization is significantly reduced with respect to bulk CFO, and depends on the specific termination. Partial inversion of CFO further weakens the MAE. Our study can be considered as a departing point to investigate more realistic interfaces, including the presence of defects (disorder, inter-diffusion, vacancies, etc). Although these particular materials allows us to design ideal interfaces, strains and nonuniform cation distributions may contribute in most experimental situations. In particular, the large magnetostriction of CFO makes its magnetoelastic response sensitive to even moderate strains,

and highly dependent on the specific cation arrangement. This aspect is studied in the next Chapter, that considers the interface between the more dissimilar MFO and CFO structures.

Chapter 6

CFO/MFO interface

6.1 Introduction

We address here the detailed description of the magnetic properties of the (001) and (111) interfaces between the hard $CoFe_2O_4$ (CFO) and soft $MnFe_2O_4$ (MFO) spinel ferrites, used in bicomponent systems for permanent magnet applications [150, 151, 152]. This work is part of a research project in collaboration with the University of Sydney, where we explore nanoparticles with multiple interfaces in order to reinforce ferromagnetism and gain versatility through manipulation of the multishell structure. Opposite to the CFO/NFO interface, the lattice mismatch between the two components leads now to a non-ideal situation in which the strain cannot be neglected. This chapter is organized as follows: first, we identify pure strain effects studying the bulk properties of both materials. The need to consider strained structures confers importance to the large magnetoelastic effect observed in CFO, which is crucially dependent on the cation distribution within the unit cell. Thus, next we explore different Co distributions and their effect on the magnetic properties. Then, the stability of different interface orientations is studied, identifying also their magnetic properties. Finally, we perform a study of the exchange interactions and how they are affected by the interface, including the magnetic coupling between Co/Mn ions.

6.2 (Pure) Strain effects

We have considered the interface formed by cobalt ferrite (CFO) and manganese ferrite (MFO) along the two different high-symmetry directions [001] and [111], depicted in Figure 5.1. Unless otherwise stated, the theoretical conditions are the same as those described in the previous chapter to model

c_{MFO}(Å)($\Delta Volume$)	[001]	[111]
Non-distorted [154]	8.51	14.73
Direct	8.56(-2.5%)	14.73(-1.7%)
Inverse	8.56(-2.5%)	14.78(-1.4%)
c_{CFO}(Å)($\Delta Volume$)	[001]	[111]
Non-distorted [155]	8.38	14.51
Direct	8.17($+0.5\%$)	14.32($+1.7\%$)
Inverse	8.16($+0.4\%$)	14.29($+1.5\%$)

Table 6.1: Optimized out-of-plane lattice parameters (c) for: (top) MFO adapting to (*inverse*) CFO in-plane lattice parameters; (bottom) CFO adapting to (*inverse*) MFO in-plane lattice parameters. The percentage of variation of the total volume with respect to the ideal bulk is shown in red, positive (negative) values corresponding to expansion (contraction).

ideal CFO/NFO interfaces. Again, we have employed a reduced unit cell of 56 atoms (28 for each material) for the [001] orientation, and 84 atoms (42 for each material) for the [111] orientation. The lattice parameter, unlike at CFO/NFO, is a bit larger for MFO, leading to an in-plane mismatch of $\sim$1.5% at the heterostructure, which ultimately affects the structural, electronic and magnetic properties of the oxides [88, 89, 90, 153]. Two different scenarios have been recreated: manganese ferrite growing on top of cobalt ferrite (CFO/MFO), and vice versa (MFO/CFO), where we consider the oxide below as the substrate imposing the 2D lattice, forcing the oxide on top to adapt to it, *e.g.* $a_{MFO} = a_{CFO}$ and $b_{MFO} = b_{CFO}$ in the CFO/MFO situation. The corresponding out-of-plane lattice parameter (c_{MFO} or c_{CFO}) is optimized from energy minimization at bulk calculations with the corresponding fixed in-plane lattice parameters, obtaining the values shown in Table 6.1. The oxide considered as substrate is always in the *inverse* form, while we explore both *direct* and *inverse* structures for the on top oxide. The percentages in parenthesis indicate the shrinkage (negative) or expansion (positive) of the volume relative to the non-distorted lattice. The structural changes are not homogeneous and depend on the orientation. MFO undergoes the largest volume changes, but they mostly come from the in-plane contraction. Oppositely, CFO tends to compensate more homogeneously the in-plane expansion with a perpendicular contraction. The effect is more prominent along [001], a less compact orientation with more room to structural changes.

We now explore how the local magnetic moments are affected by these lattice distortions. The corresponding values for the inverse structure at (001) orientation, in Table 6.2, show a general decrease, specially at cobalt ferrite,

$MM_{CFO}(\mu_B)$	Fe_A	Fe_B	Co	Total
CFO_{exp}^{Direct}		4.17-4.26	-2.57	27.79
$CFO_{adapted}^{Direct}$		4.13	-2.37	27.98
$CFO_{exp}^{Inverse}$	-4.06	4.17	2.65	12.00
$CFO_{adapted}^{Inverse}$	-3.97	4.11	2.63	12.00
$MM_{MFO}(\mu_B)$	Fe_A	Fe_B	Mn	Total
MFO_{exp}^{Direct}		4.06	-4.08	20.00
$MFO_{adapted}^{Direct}$		4.05	-4.04	20.00
$MFO_{exp}^{Inverse}$	-3.94	4.13	4.47	19.98
$MFO_{adapted}^{Inverse}$	-3.92	4.11	4.44	19.81

Table 6.2: Total magnetization and partial cation magnetic moments of bulk CFO (top) and MFO (bottom) at (001) orientation for: direct and inverse structure; corresponding experimental bulk lattice parameters (*exp*) and distorted lattice parameters (*adapted*). Last column shows total magnetization per unit cell.

for both inverse and direct structures while maintaining the total magnetization, shown at the last column. Values for the (111) orientation, not shown, exhibit a similar behavior. In Figure 6.1, we show the charge and spin density differences when comparing distorted and undistorted CFO along (001) at the inverse structure. The charge density evidences the charge accumulation along the z axis at the cost of depleting the xy plane, since we are shortening the z-bonding distance as a response to the epitaxial expansion. The spin density follows the same pattern for octahedral cations, and the opposite for tetrahedral ones. The figure evidences that, besides the change in the integrated spin charge, strain is introducing a spatial redistribution of the spin density.

As commented previously, the presence of strain introduces an additional ingredient to be considered, since CFO shows large magnetoelastic coefficients that are known to be highly sensitive to the specific cobalt distribution within the unit cell. Thus we have analyzed the impact of different cation arrangements on the electronic and magnetic properties of bulk CFO in the presence of lattice distortions. The choice of the different distributions relies on a previous thorough study of bulk CFO [88], and led us to consider the three structures shown in Figure 6.2: CFO^{rand} with cobalt atoms placed maximizing the distance between them, that corresponds to the structure used in all previous models of CFO in this thesis; CFO^{x-axis} where Co atoms order in chains along the x axis; and $CFO^{xyz-axis}$, in which the cobalt atoms arrange in chains along the (111) direction. In Table 6.3 we compare the

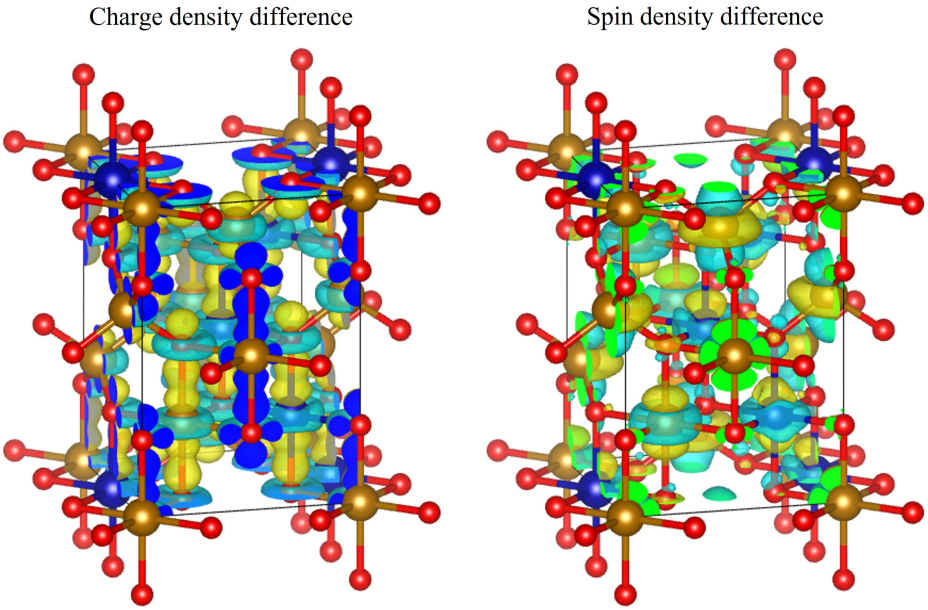

Figure 6.1: Charge density difference between CFO adopting the MFO in-plane lattice parameters and non-distorted CFO. Positive (negative) difference is plotted in yellow (light blue).

relative stability of all these distributions at the undistorted and strained CFO, restricting to CFO(001) for the sake of simplicity. First we notice that the energy differences are three orders of magnitude below that between direct and inverse structure, evidencing the plausibility of finding all of these configurations in real samples. Second, the distortion of the lattice has a different impact on the relative stability of each specific cation distribution. The degeneracy between CFO^{x-axis} and $CFO^{xyz-axis}$ at the undistorted lattice emerges as in fact both distributions are equivalent when no distortion is applied, the difference coming only from the orientation of the cation planes: one of them can be recovered starting from the other applying two consecutive 45 degrees rotations around the cubic crystal axes. When the (001) epitaxial constraint is applied, though, these equivalency breaks down. Last, the table also evidences that the distortion enhances the stability of the random distribution, even though the energy differences are low enough for all distributions to coexist. On the other hand, and importantly, we have checked that neither the magnetic moments of each atomic species nor the relative stability between different magnetic configurations (c0-c4 in Table 4.1) are affected by the specific cobalt distributions. Though we have not studied in detail different Co distributions under (111) epitaxial strains, the

$E(meV/f.u.)$	Non-distorted	Distorted
Random	0	0
x-axis	6	13
xyz-axis	6	20

Table 6.3: Energy differences with respect to the most stable case (random) of the different cobalt distributions considered for both, distorted and non-distorted unit cell.

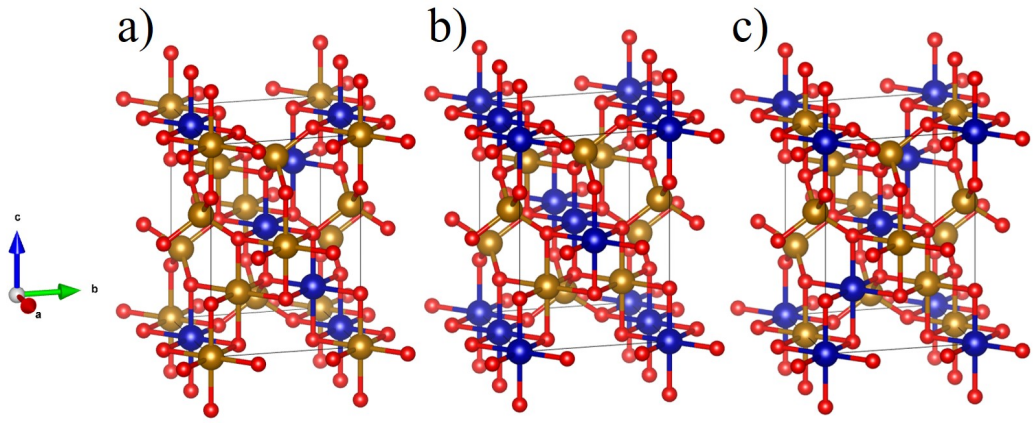

Figure 6.2: Unit cells of *bulk* CFO with three different cobalt distributions: a) random, b) x-axis and c) xyz-axis.

results are expected to be similar.

A different scenario emerges when we consider how the magnetocrystalline anisotropy energy (MAE) of bulk CFO is affected by the cobalt distribution and the distortion of the lattice. In Figure 6.3 we compare the energy of the system with the magnetization along different crystal axes, using as reference the case with (001) orientation of the magnetization. The results indicate that the cobalt distribution affects severely the magnetic anisotropy, and may change the easy axis direction, even in the absence of distortions: it lies along [001] (or its symmetrically equivalent cubic axis) under random and x-axis distributions, while it is contained at the xy-plane under xyz-axis distributions. The distortions considered by us do not alter the hierarchy of easy and hard axes associated to each cation arrangement, but significantly modify the value of the MAE. Following the expected trends already pointed out by Ederer *et al* [88], tensile strains tend to favor magnetization orientation along [001], either reinforcing its stability as easy axis, or softening other easy axes relative to [001].

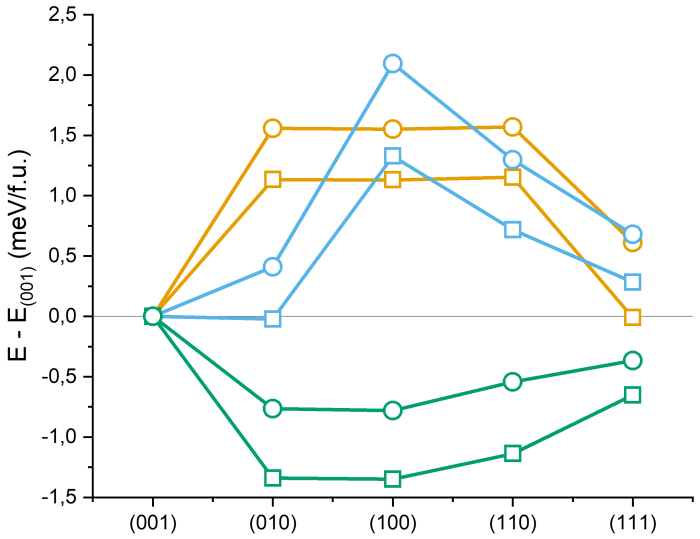

Figure 6.3: CFO total energy for different orientations of the magnetization relative to the (001) direction. Yellow, blue and green lines correspond to *random*, *x-axis* and *xyz-axis* cobalt distributions respectively; open squares (circles) indicate the non-distorted (epitaxially strained) lattice.

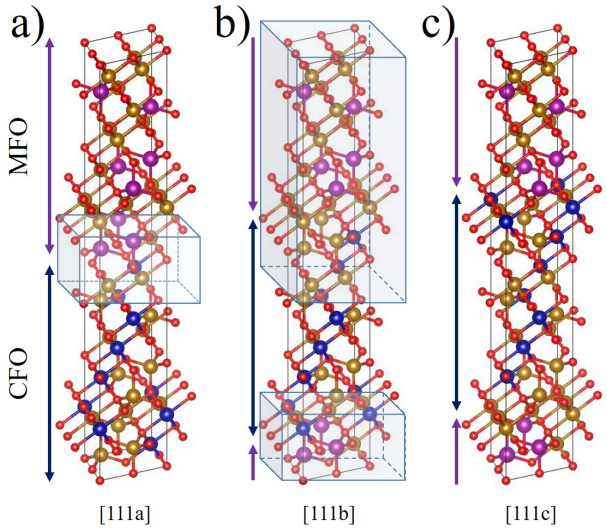

Figure 6.4: The three different terminations considered in [111] orientation. Blue boxes indicate the two different ionic relaxations considered: *interface* shown at a) and *slab* shown at b). Both relaxation methods are studied on the three terminations, although they are not shown for the sake of clarity.

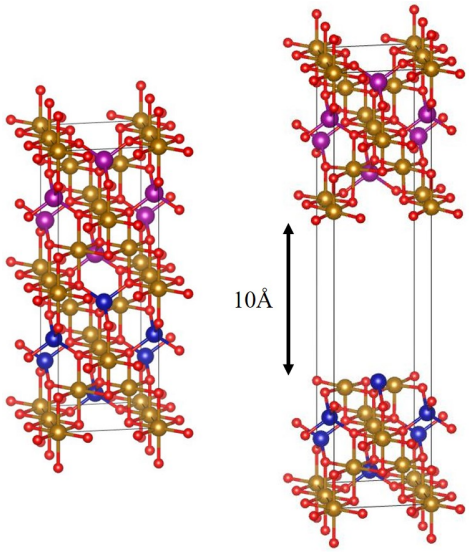

Figure 6.5: The two unit cells involved in the method for calculating the work of separation of the [001] orientation interface.

6.3 Structural stability

After identifying the influence of strain on the isolated materials, we consider now the interface properties. Similarly to the CFO/NFO system, the (001) orientation only admits one possible interface between both components, the rest of them being rotationally equivalent, while the (111) orientation leads to three different terminations as shown in Figure 6.4: [111a], [111b] and [111c], which correspond to the $C \mid A$, $A \mid B$ and $B \mid C$ interfaces respectively. For all of them, we keep ideal cubic positions at the undistorted oxide. We remark that, as explained in the previous section, at each interface model both oxides share a common in-plane lattice but have different out-of-plane lattice parameters.

First, we address the relative stability of all these possible interfaces, including the inverse and direct forms, and based on two different methods:

1. A direct comparison of their total energies, normalized per formula unit to enable comparison of the different orientations [001] and [111]. We also explored two different relaxation methods at the interface:

   (a) *interface* relaxation, where only the atoms from layers close to the interface are relaxed as shown in Figure 6.4 a). The corresponding results are shown in the top panels of Figure 6.6 for CFO/MFO (top left) and MFO/CFO (top right).

(b) *slab* relaxation, in which the ionic relaxation is allowed at the entire distorted oxide, as shown in Figure 6.4 b). The corresponding results are shown in Figure 6.6 for CFO/MFO (bottom left) and MFO/CFO (bottom right).

When allowed to relax, the ionic positions change in the three dimensions. We have checked that the specific Co distribution does not play an important role in the relative stability of the different interfaces. This is shown at the right column of Figure 6.6, that evidences similar trends for x and xyz-axis than for the random distribution.

The results in Figure 6.6 evidence that great care needs to be taken when relaxing the interface systems, as different procedures may lead to a different conclusion regarding relative stabilities. This is particularly important as these conclusions affect the presence of the inverse or direct spinel forms, with completely different magnetic responses. The relaxation of CFO (results at the right columns) is less dependent on the relaxation method, and favors a uniform inverse spinel system for all interface orientations. On the contrary, the relative stability of the direct and inverse MFO forms under distortion is highly dependent on the relaxation method. This effect was already observed in the bulk form (section 4.2): the atomic positions at the direct MFO spinel depart from cubic symmetry, and when it is imposed, the inverse form becomes more stable. This is the effect we observe here: when only a portion of the atoms, those close to the interface, are allowed to relax, the inverse MFO is preferred. Though this result might seem artificial, actual constraints limiting the ability of the layers to relax may be present at nanoparticles.

2. Our second method to estimate the relative stabilities of the interfaces is to calculate the work of separation (W_{sep}), which accounts for the energy needed to break the interface between the two oxides. In practice, as mentioned in Chapter 5, to calculate W_{sep} we introduce a 10Å vacuum region between both components exactly at the interface, and compare the energy, normalized per contact surface area, of the resulting system to that of the interface system, as shown in Figure 6.5 for the [001] case. The energy range of W_{sep} is one order of magnitude greater than the energy differences arising from the atomic relaxations or varying cobalt distributions, thus we restrict to the *interface* relaxation case and to *random* cobalt distributions. The results are shown in Figure 6.7, that proves the [111] interface bonds to be stronger than those at the [001] interface, since the energy to break the interface is

larger. On the other hand, the different [111] terminations may coexist, as they show a very similar W_{sep}, in good agreement with the trends shown in Figure 6.6.

Finally, we have also considered the influence of the layer thickness on the structural stability of the bicomponent system. This study is particularly interesting for the design of multishell nanoparticles with tailored properties, and in our case we focus on nanoparticles with CFO at the core. Even restricting to this CFO/MFO interface, considering all possibilities of varying thicknesses is computationally demanding, thus we restrict to the (001) orientation. The unit cells are constructed using the same 56 atoms unit cell employed in previous calculations, but varying the amount of MFO layers from 1 to 4 MFO, as shown in Figure 6.8. The atomic positions of the whole MFO layer are relaxed, thus the case with 4 MFO layers matches the "slab relaxation" (already at the bottom left panel of Figure 6.6). The relative energies of the different structures considered, combining both the inverse and direct spinel forms, is shown in Figure 6.9. The most noticeable result is that the inversion of MFO is favored for ultrathin layers, while the direct lattice is retrieved for thicker layers. However, the energy differences are very low, and coexistence of both forms is expected. On the contrary, the presence of direct CFO implies a significant energy increase, higher as the CFO thickness enlarges. In summary, we can conclude that the MFO thickness is not expected to alter the dominance of inverse CFO, but may favor the relative proportion of direct MFO as the film thickens.

6.4 Magnetic order and Magnetization

Now, we provide a detailed analysis of the magnetic properties at the interface, focusing in the ground state magnetic configuration and the evolution of the magnetic moments close to the interface. Including all possible variations (*i.e.* different terminations, Co distributions, lattice inversion, etc.) is an endeavoring task, thus we will restrict to specific conditions at the (001) termination, discussing how much representative they are of a more general scenario. First, the energy differences between magnetic configurations are several orders of magnitude smaller than that between [001] and [111] terminations, thus we do not expect that the magnetic configurations affect the stability between both orientations. Here, we focus on CFO/MFO interfaces with both materials at full inversion, which have been shown in Figure 6.6 to be the most stable configurations. Besides, this choice allows us to define the same magnetic configuration over the entire structure, hence easing the

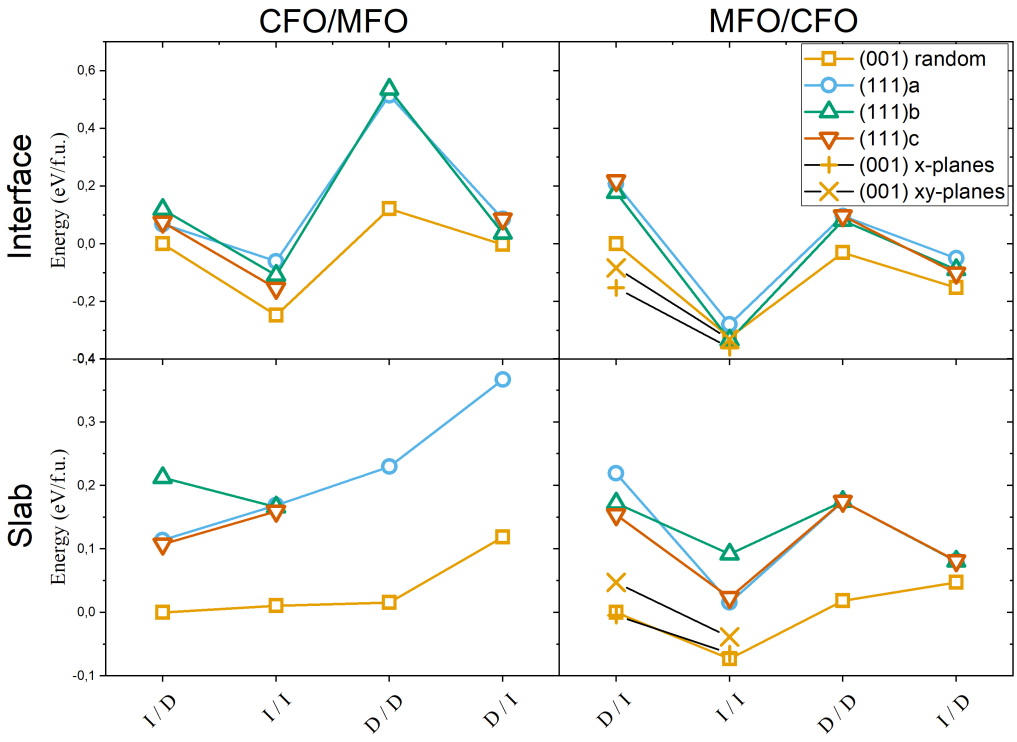

Figure 6.6: Relative stability of the different CFO/MFO and MFO/CFO interface orientations for different combinations of the direct (D) and inverse (I) forms (for bottom/top oxides) and different cobalt distributions. The top (bottom) row includes cases under *interface* (*slab*) relaxation. The left column corresponds to the CFO lattice (MFO adapting to it), while the MFO lattice has been used for results on the right column. *x-axis* and *xyz-axis* cobalt distributions are included in MFO/CFO figures. The zero energy of each figure is set as the energy of the (001) *random* termination.

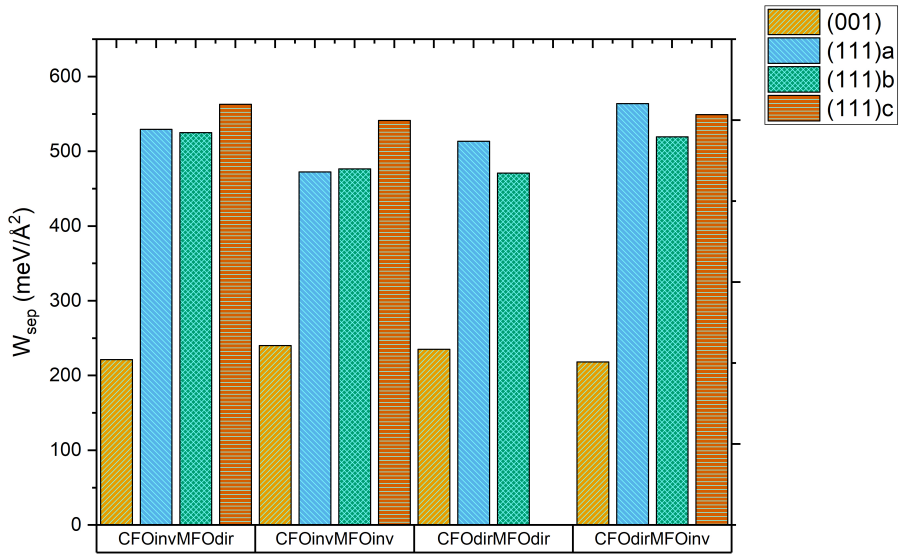

(a)

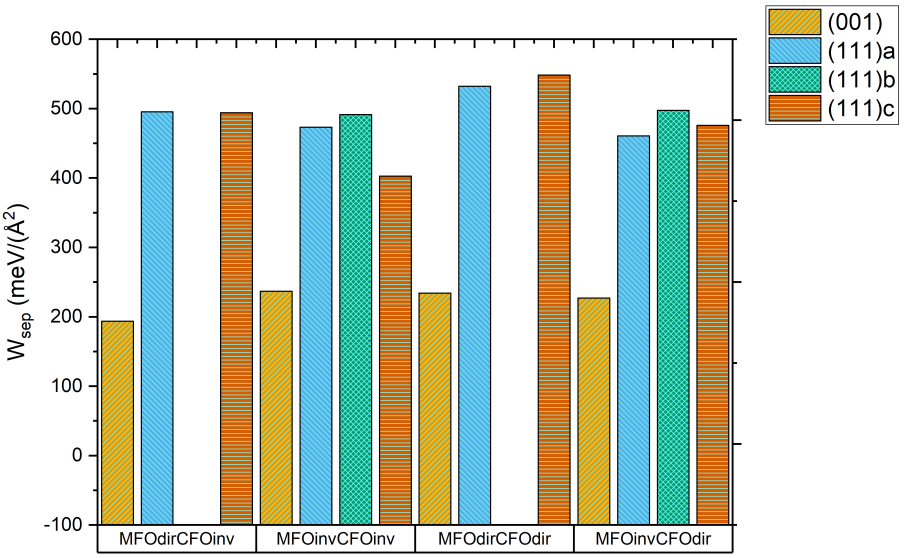

(b)

Figure 6.7: Work of separation for a) CFO/MFO and b) MFO/CFO interfaces. The empty columns symbolizes calculations that could not converge properly, reflecting the instability of the interface.

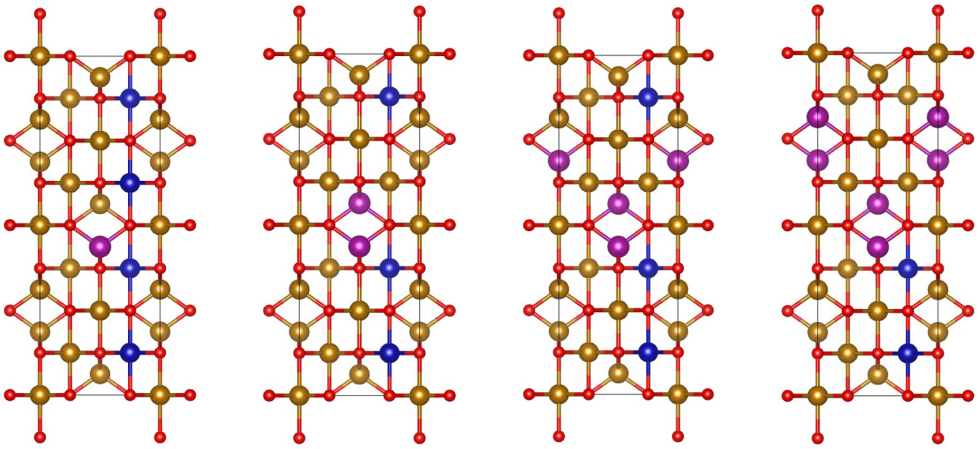

(a) (b) (c) (d)

Figure 6.8: Unit cells of [001] CFO/MFO interface for different MFO thickness from a) 1 layer to d) 4 layers. Cobalt atoms are represented in blue while manganese atoms in purple.

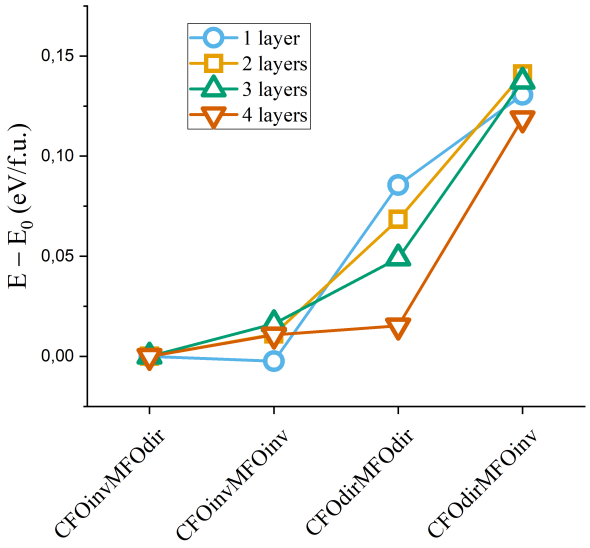

Figure 6.9: Relative stability of different MFO layer thickness. The energies are compared to the corresponding CFO at inverse / MFO at direct case energy.

Structure	-Δ(AF-FM) (eV/f.u.)
Bulk CFO	0.749
Bulk MFO	0.813
1 layer	0.752
2 layers	0.781
3 layers	0.811
4 layers	0.840

Table 6.4: Energy difference between AF and FM configurations for the different MFO layer thickness.

analysis of the role of the interface. CFO and MFO, as shown in Chapter 4, show a ferrimagnetic state, where ions at A and B positions are antiparallel to one another for both inverse and direct lattice. We explored different spin arrangements of the relevant magnetic sublattices, that is, configurations c0-c3, defined for inverse structures in Table 4.1. The values obtained for CFO/MFO, both at the inverse spinel form, are shown in Figure 6.10, where we also show bulk CFO and MFO for comparison. It evidences that the interface does not alter the bulk-like ferrimagnetic order, neither the *interface* relaxation affects the trend of the energies given by the two components. Yet, *slab* relaxation does affect this trend. This will affect the values of the exchange coupling constants that are derived from the energies of these different magnetic configurations as we will show in Section 6.5. We also explored the energy difference between c0 and c1 (-Δ(AF-FM)) for the different MFO layer thickness considered in the previous section. The results, shown in Table 6.4, indicate that the ferrimagnetic configuration is always favored over the ferromagnetic one, and that the interface just contributes with an additive effect. Specifically, we found a trend in which adding more layers enlarges this energy difference, till the point of surpassing bulk values. The rest of the cases (CFO and/or MFO at direct spinel form) have not been studied in detail, although we have checked that the ferrimagnetic configuration is always favored over the ferromagnetic one.

The values of the local magnetic moments for each atomic species and how they are affected by the interface have been studied rigorously for CFO/MFO case at the groundstate c0. We explored the values within and outside of the actual interface layers for the combinations CFO at inverse / MFO at inverse and CFO at inverse / MFO at direct spinel structure and for the different layer thickness and the terminations considered in Section 6.3. They are shown in Table 6.5 and compared to bulk values. There is a minor enlargement of iron magnetic moments at both CFO and MFO compared to bulk

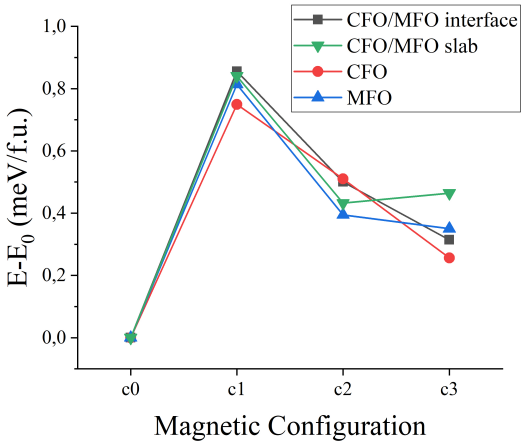

Figure 6.10: Relative stability of CFO at inverse /MFO at inverse system for the different magnetic configurations defined in Table 6.7.

values. Cobalt atoms do not seem affected by the interface, while manganese magnetic moments are only enhanced at direct lattice. The specific cobalt distribution does not modify the local magnetic moments on MFO/CFO interfaces, whose values we do not show explicitly since they show essentially no dispersion. In general, the interface enhances local magnetic moments over those out of the interface.

System	Termination	CFO_{Fe_B}		MFO_{Fe_B}		CFO_{Fe_A}		MFO_{Fe_A}		Co		Mn	
Bulk CFO Inverse		4.11				−3.96				2.63			
Bulk MFO Inverse				4.13				−3.94				4.47	
Bulk MFO Direct				4.06								−4.08	
		Outside	Inside	Outside	Inside	Outside	Inside	Outside	Inside	Outside	Inside	Outside	Inside
CFO inverse / MFO inverse	[001]	4.12	4.13	4.13	4.14	−3.99	−4.02	−3.96	−4.00	2.64	2.64	4.46	4.49
	$[111]_a$	4.06 — 4.12	4.13	4.13		−3.95 — −4.00		−3.92	−3.99	2.58 — 2.68	2.63	4.45	4.47
	$[111]_b$	4.11		4.08 — 4.12	4.14	−3.97	−4.02	−3.92 — −3.98		2.63	2.62	4.44 — 4.48	4.46
	$[111]_c$	4.11	4.14	4.12		−3.94 — −4.03		−3.91	−3.99	2.63	2.63	4.45	4.48
CFO inverse / MFO direct	[001]	4.09	4.12	4.07	4.15	−3.99	−4.04			2.63	2.63	−4.00 — −4.31	−4.48
	$[111]_a$	4.11	4.14	4.02 — 4.13	4.13	−3.98				2.63	2.67	−3.98 — −4.03	−4.47
	$[111]_b$	4.11		4.06	4.12	−3.97	−4.04			2.63	2.62	−3.96 — −4.41	
	$[111]_c$	4.11	4.15	4.02 — 4.13	4.17	−3.97 — −4.01				2.63	2.67	−3.99 — −4.03	−4.47
CFO inverse / MFO direct	1 layer	4.13	4.15		4.15	−4.03	−4.04			2.63	2.65		−4.48
	2 layer	4.13	4.15		4.16	−4.03	−4.04			2.63	2.66		−4.49
	3 layer	4.13	4.14		4.17	−4.03	−4.04			2.63	2.66		−4.50
	4 layer	4.13	4.14		4.17	−4.03	−4.04			2.63	2.65		−4.49

Table 6.5: Local magnetic moments within and outside the interface for different inversion states of MFO and different terminations. Bulk values are also included for comparison purposes. Some magnetic moments show a greater dispersion so they are shown as a range of values. The last set of rows correspond to values for [001] termination of the various layer thickness explored in Section 6.3.

6.5 Exchange Coupling Constants

Finally, we explore how the exchange coupling constants (J_{ij}) are affected by the presence of the interface. As we described in section 2.4, Js can be extracted mapping the energies of different magnetic configurations into a Heisenberg hamiltonian, following equation 2.37. In bulk CFO and MFO we can define magnetic sublattices made of atoms with the same crystal environment (same atomic neighborhood). Here, as we already observed in Chapter 5, the interface is breaking some symmetries of the crystal, making more difficult the definition of the magnetic sublattices. The problem is complex, particularly as now there are more ingredients affecting the symmetry of the system, due to the presence of strains. In this section we will perform a first approach to this problem, trying to identify the main interface effects on the exchange interactions. First, we will focus on the Fe_A and Fe_B sublattices at the dominant inverse spinel structure, that provide the strongest exchange interaction at bulk CFO and MFO as we showed in sections 4.1 and 4.2. The unique difference between the atoms of these sublattices on either side of the interface is the chemical nature of some neighbors, either cobalt or manganese, that in turn occupy the same lattice positions at each side of the interface plane. Additionally, the value of the exchange coupling between Fe_A and Co at bulk inverse CFO, $J_{Co-Fe_A} = 2.222 meV/\mu_B^2$, is close to that between Fe_A and Mn at inverse MFO $J_{Mn-Fe_A} = 1.805 meV/\mu_B^2$, and also the exchange constants associated to the interaction with Fe_B, J_{Co-Fe_B} and J_{Mn-Fe_B}, are of similar order of magnitude and much weaker than the interaction with Fe_A. Thus, in a first rough approach, we can approximately regard all Fe_A as forming the same sublattice through the entire heterostructure, and likewise for Fe_B. Relying on this approach, we follow the aforementioned method to extract an approximate value of the exchange coupling between Fe_A and Fe_B at the CFO/MFO and MFO/CFO systems. The magnetic configurations used to extract $J_{FeA-FeB}$ are those defined in Table 4.1 as c0-c3. Further, we consider different relaxation methods (*interface* or *slab*) and Co distributions, to determine how these features affect the exchange constants.

Table 6.6 shows the values of $J_{Fe_A-Fe_B}$ obtained at the CFO/MFO interface after *interface* and *slab* relaxations, compared to those at the bulk counterparts. Under the *interface* relaxation, we obtain an intermediate value between those of the bulk forms, reflecting that the interface is not modifying the exchange interactions. On the contrary, exchange reduces slightly below the bulk MFO value when a *slab* relaxation is carried out. To understand this effect, we explored the evolution of $J_{Fe_A-Fe_B}$ with the MFO thickness. We found that the thickness of the MFO layer plays a fundamental role in the resulting exchange coupling constant: for thin MFO (1

	CFO	MFO	CFO/MFO *interface*	CFO/MFO *slab*
$J_{Fe_A-Fe_B}$ (meV/μ_B^2)	2.91	2.19	2.61	1.98

Table 6.6: Value of the dominant exchange coupling constants for CFO/MFO, with both oxides at inverse structure, under the different interface relaxation methods. Bulk values are shown for comparison.

to 3 MFO layers) a constant value around 2.36 meV/μ_B^2 is obtained, that drops at 4 layer thickness to 1.98 meV/μ_B^2. Though we cannot extract the individual oxide contributions to the exchange, this result seems to reflect that the weakening of the exchange is mainly coming from MFO, probably arising from the distorted structure. To further explore this idea, $J_{Fe_A-Fe_B}$ has been calculated at MFO/CFO at the various cobalt distributions defined in Section 6.2, showing very similar values of 2.63 and 2.73 meV/μ_B^2 for *x-axis* and *xyz-axis* distributions respectively. First, these values are again intermediate between those of the corresponding bulk oxides, indicating that strain effects are not significant for the CFO exchange interaction. Second, there is a low influence of the Co distribution in the exchange coupling constant, as expected from the fact that the number of magnetic neighbors of each atom is not altered at each specific distribution.

We can conclude that, except for some strain induced modifications at MFO, the interface induces moderate changes in $\mathrm{J}_{Fe_A-JFe_B}$, that furthermore are not expected to alter significantly the hierarchy between exchange constants. As a further proof of this last hypothesis, Figure 6.10 already showed that the scale of energy differences among magnetic configurations is similar at CFO and MFO, and the same occurs at their interfaces including strain effects.

The only additional exchange interaction present at the interface but not at the corresponding bulk oxides is that between Mn and Co ions.In order to explore it, we studied two systems:

1. A substitutional Mn impurity embedded in bulk CFO, that we model in a unit cell of 28 atoms that corresponds to the chemical formula $Mn_{0.25}Co_{0.75}Fe_2O_4$.

2. A substitutional Co impurity at bulk MFO, similarly corresponding to the chemical formula $Co_{0.25}Mn_{0.75}Fe_2O_4$.

For these two systems, we studied the relative stability of introducing the substitutional impurity at octahedral and tetrahedral position, both at the *direct* and *inverse* spinel structure of the corresponding bulk oxide. The

results are shown in Table 6.8. Co impurities replacing Mn atoms at MFO prefer tetrahedral coordination sites at both *inverse* and *direct* spinel structures. On the other hand, Mn impurities at CFO keep the positions already occupied by the substituted Co ions, *i.e.* Mn_B for *inverse* CFO and Mn_A for *direct* CFO. We have explored the exchange interactions at the four different cases in the Table. The impurities reduce the symmetry of the unit cell, hence rendering the equation 2.37 unusable to obtain exchange coupling between A and B positions since they are no longer real sublattices. However, we noticed that a renormalization of the number of neighbors $\tilde{z}_{ij}$ can be used, which now gives an effective exchange constant between i and j-atoms:

$$\tilde{J}_{ij} = \frac{E_{ij} + E_0 - E_i - E_j}{4n_i \tilde{z}_{ij} \vec{S}_i^{\alpha_0} \cdot \vec{S}_j^{\alpha_0}} \tag{6.1}$$

The dispersion of z_{ij} is found to be small, which guarantees that its mean value $\tilde{z}_{ij}$ and thus $\tilde{J}_{ij}$ are representative values of the interaction. All the exchange-coupling constant values obtained through this method are shown in Table 6.9, where we also show bulk CFO and MFO values for comparison. The exchange coupling constants of the direct spinel forms have been derived using the magnetic configurations shown in Table 6.7.

First we focus on the inverse spinel structures, which are expected to be the most abundant at the bicomponent CFO-MFO systems. Already at the undoped bulk forms, the exchange interactions at CFO tend to be higher than at MFO, though the hierarchy between exchange constants is identical. Further, while some ferromagnetic interactions emerge in CFO (that between Co and Fe_B), MFO only admits antiferromagnetic couplings. The octahedral (B) impurities tend to reproduce the situation at their bulk form, thus a Mn_B impurity at inverse CFO slightly weakens most exchange interactions and suppress ferromagnetism, while a Co_B impurity at MFO tends to enhance the exchange constants. In both cases, impurities maintain the hierarchy between exchange constants. The Co-Mn interaction is antiferromagnetic and large as compared to the interaction with Fe_B, but remains one order of magnitude below the coupling between A and B sublattices. In general, this detailed analysis let us conclude that in bicomponent inverse spinel systems (I/I) the magnetic exchange interactions will be bulk-like, with no relevant interface induced modifications.

When the substitutional impurity occupies a tetrahedral position (A) both Co and Mn impurities tend to weaken the dominant coupling between A and B sublattices, that however continues to be the largest exchange interaction. This weakening manifests in two ways: on one hand, the exchange constants with Fe_A of all B cations tend to lower; on the other, the interac-

Magnetic configuration	Fe_{B1}	Fe_{B2}	Co/Mn
c_0 (AF)	+	+	−
c_1 (FM)	+	+	+
c_2	−	+	−
c_3	−	+	+

Table 6.7: Schematic representation of the different magnetic configurations explored in a direct spinel structure. +/− signs indicate different spin orientations.

Energy ($eV/u.c.$)	MFO inverse	MFO direct	CFO inverse	CFO direct
Co at A	−196.04081	−196.69625		
Co at B	−195.50227	−195.91781		
Mn at A			−189.67242	−189.42391
Mn at B			−189.69526	−188.95282

Table 6.8: Energy per unit cell of the different systems for the different impurity positions.

tion of the B cations with the impurity at the A site is considerably weaker than with Fe_A. An exception occurs at the ferromagnetic Mn_A-Fe_B exchange in CFO inverse, which is large and ferromagnetic. This is a surprising result that needs further study, and that might correspond to an artificial local minimum of the magnetic configurations considered. In any case, the net effect of the A impurities at the inverse structures is a weakening of the dominant exchange coupling between A and B sublattices.

A similar conclusion can be extracted analyzing the exchange constants when B impurities are introduced at the oxides in their direct forms. All these results are relevant for interfaces between inverse and direct forms (I/D), where the interface may introduce a weakening of the dominant exchange couplings.

Finally, the presence of tetrahedral impurities at the direct spinel forms lowers significantly the magnetic exchange constants, even though the antiferromagnetic coupling between A and B sublattices is preserved.

J (meV/μ_B^2)	CFO inverse	CFO direct	MFO inverse	MFO direct	$Mn_{0.25}Co_{0.75}Fe_2O_4$				$Co_{0.25}Mn_{0.75}Fe_2O_4$			
					Inverse		Direct		Inverse		Direct	
					Mn at A	Mn at B	Mn at A	Mn at B	Co at A	Co at B	Co at A	Co at B
J_{Co-Mn}					0.998	0.560	0.284	0.931	0.796	x	0.241	0.186
J_{Co-Fe_A}	2.222				2.296	1.860		x	0.331	x		1.685
J_{Co-Fe_B}	−0.387	2.457			−0.029	−0.017	1.345	1.530	1.546	x	1.198	0.499
J_{Co-Co}	0.276	0.385										
J_{Mn-Fe_A}			1.805			2.293		2.403	1.980	1.411		0.367
J_{Mn-Fe_B}			0.232	2.813	−2.009	x	1.516	1.160	0.820	0.735	1.282	1.354
$J_{Fe_A-Fe_B}$	2.912		2.186		2.239	2.431		1.996	2.119	2.292		1.834
J_{Mn-Mn}			0.590									

Table 6.9: Exchange coupling constants for substitutional Mn impurities at CFO ($Mn_{0.25}Co_{0.75}Fe_2O_4$) and Co impurities at MFO ($Co_{0.25}Mn_{0.75}Fe_2O_4$). Values for the *direct* and *inverse* structures of both CFO and MFO at bulk are shown for comparison. Empty values reflect that the exchange coupling constant is not defined atg the corresponding structure or that the ions involved are far neighbors. The value x indicates that one or more magnetic configurations needed to obtain the specific exchange coupling constant has not converged to a ground state.

6.6 Conclusions

A detailed study of the magnetic properties at non-ideal CFO/MFO interfaces has been presented, including effects induced by the degree of inversion λ of both CFO and MFO, the strain arising from the mutual lattice mismatch and the Co distribution. Strain induced effects can be isolated at bulk simulations. This way, we identify a reduction in the local magnetic moments, while maintaining the total magnetization, together with a redistribution of the charge and spin densities. Further, the relative stability of dfferent Co distributions is altered, with important consequences on the magnetic anisotropy, that favors the (001) direction as easy axis. At the interface, we have shown that the relaxation method plays a fundamental role in the structural properties of the system, as the degree of inversion of MFO crucially depends on it, which ultimately leads to large differences in the resulting electronic and magnetic properties. In general, [111] orientation of the interface is favored over [001]. We also show how the layer thickness may affect the direct/inverse ratio of the MFO spinel structure, that is related to the tendency of bulk MFO to break the internal cubic symmetry of the unit cell. In general, local magnetic moments at the interface are enhanced compared to those at bulk, and the bulk magnetic order is preserved in all cases considered. Lastly, exchange coupling interactions are affected by the interface in a different way depending on the MFO thickness. In general, the hierarchy between exchange interactions is presented, and the global exchange tends to be tends to be the sum of the individual contributions of both oxides.

Chapter 7

$\mathbf{Zn}_x\mathbf{Ni}_{1-x}\mathbf{Fe}_2\mathbf{O}_4$ (ZNFO)

7.1 Introduction

Zinc substituted nickel ferrite ($Zn_xNi_{1-x}Fe_2O_4$) for x $\leq$ 0.50, with special attention to the influence of the Zn d band localization on the degree of inversion, the electronic structure and the magnetic properties. This chapter is organized as follows: after introducing the motivation, we consider two different representative concentrations of the Zn doped NFO that can be modelled with moderately large unit cells, namely $Zn_xNi_{1-x}Fe_2O_4$ with x=0.25, 0.50. We explore different Zn distributions, always allowing Zn atoms to occupy A and B sites.

As we saw in Chapter 4, $NiFe_2O_4$ (NFO) and $ZnFe_2O_4$ (ZFO) are important soft magnets with opposite distribution of divalent and trivalent cations: while NFO is an inverse spinel, with Ni^{2+} (Fe^{3+}) at octahedral (tetrahedral) positions, ZFO is usually classified as a direct spinel, where Zn^{2+} cations occupy tetrahedral sites. However, the specific cation distribution at nanostructures depends on the processing parameters and preparation conditions, particularly for mixtures of both oxides [156, 157, 158]. The final atomic arrangement largely depends on the sintering method and the detailed preparation conditions, and importantly, it has consequences on the magnetic properties of the system.

We also proved that the magnetic properties of cubic spinel ferrites are governed by the dominant antiferromagnetic exchange interaction between tetrahedral (A) and octahedral (B) cations, as described by the Néel model [159], with a resulting collinear ferrimagnetic order, c0. Thus, in general, the net magnetization corresponds to the difference between the B sublattice contribution minus that from the A sublattice. This balance alters when non-magnetic elements occupy the A sites, as occurs in ZFO: then, the com-

petition of magnetic exchange interactions between B cations determines the global magnetic order, leading to a rich magnetic phase diagram involving frustration [94, 98, 126].

In the case of NFO, the largest local magnetic moments correspond to Fe^{3+} cations at A sites, thus a route to enhance the net magnetization is to remove these cations introducing a partial substitution of Ni by Zn atoms, that are expected to occupy A sites. For moderate Zn concentrations, these Ni-Zn ferrites usually show higher values of the saturation magnetization as compared to pure NFO [160, 161]. But depending on the preparation conditions, it is possible to tailor the crystal structure and cation distribution [82, 162, 163, 164]. As the Zn concentration increases, a mixed spinel structure with Zn atoms both at A and B sites often emerges [139, 161, 165, 166], together with a low temperature phase rooted in the Yafet-Kittel canting of the local magnetic moments at B sites [120, 167]. Both effects are detrimental to enhance the magnetization, but their consequences are different. Magnetic canting manifests only at low temperatures and evolves to the usual ferrimagnetic collinear order as the temperature increases [168]. While partial Zn inversion is an intrinsic feature of the nanostructure, that furthermore favors the mixing of NFO and ZFO [169].

From a theoretical point of view, the electronic structure of Zn doped NFO has been considered only scarcely. Early density functional theory (DFT) calculations described the full range of concentrations at $Ni_xZn_{1-x}Fe_2O_4$ based on LDA or GGA exchange correlation functionals, that fail to describe the cubic spinels as insulators [170, 171]. Later simulations focused on the solubility of NFO/ZFO mixtures included a local U term to correct this description [169]. The value of U was taken from previous calculations of the corresponding monoxides, and in particular a large value over 7 eV was used for Zn d electrons. This is in contrast to previous DFT works devoted to ZFO, where a moderate or even null $U(Zn_d)$ is claimed to properly capture the experimental features [94, 95]. In this work we revisit the substitution of Ni by Zn at NFO, investigating Zinc substituted nickel ferrite ($Zn_xNi_{1-x}Fe_2O_4$) for $x \leq 0.50$, with special attention to the influence of the Zn d band localization on the degree of inversion, the electronic structure and the magnetic properties. This chapter is organized as follows: after introducing the motivation, we consider two different representative concentrations of the Zn doped NFO that can be modelled with moderately large unit cells, namely $Zn_xNi_{1-x}Fe_2O_4$ with x=0.25, 0.50. We explore different Zn distributions, always allowing Zn atoms to occupy A and B sites.

7.2 Methods

Following chapter 4, the *ab-initio* DFT+U simulations have been performed with VASP under PBEsol, using a Hubbard U(Ni_d, Fe_d)= 4 eV, which we found to be the best choice to properly describe the structural, electronic and magnetic properties of NFO under our theoretical conditions, and also to reproduce the ZFO experimental band gap around 2 eV [172, 173].

All structures considered are allowed to fully relax, including the lattice vectors and the atomic positions, until the forces on the ions are below 0.01 eV/Å. This way we determine both the equilibrium volume and the optimized positions. $Zn_xNi_{1-x}Fe_2O_4$ (ZNFO) is modelled replacing one (x=0.25) or two (x=0.50) Ni atoms of the 28 atoms unit cell by Zn. Substitutional Zn is allowed to occupy both tetrahedral and octahedral cation sites, and different Zn distributions are considered, as detailed in the next sections.

The magnetic configuration of each system is explored comparing different reference magnetic orders that serve to extract exchange interactions using eq.2.37 as we explained in 2.4. The spin-orbit coupling is included only to evaluate the magnetic anisotropy energy, that is determined directly from *ab-initio* total energy differences method mentioned in 2.3.

In the following, we address the properties of $Zn_xNi_{1-x}Fe_2O_4$ with x=0.25, 0.50. In principle, Zn atoms enter as substitutional cations of Ni, that occupies octahedral (B) sites. However, the previous study of ZFO (section 4.3) has evidenced that Zn prefers to fill tetrahedral (A) positions at the spinel ferrite structure. Both situations will then be considered. Again we are particularly interested in understanding the influence of U(Zn_d) on the features of ZNFO. We will analyze separately the different Zn concentrations, starting by x=0.25.

7.3 x=0.25

Within our unit cell of 28 atoms, this concentration is equivalent to replacing one Ni atom by Zn. Figure 7.1 shows the resulting spin-resolved DOS of this unit cell at the magnetic ground state of NFO, c0, with Zn either at A (Zn_A) or B (Zn_B) sites and for the extreme values of U(Zn_d) considered here. Similarly to the case of ZFO, the choice of the largest U(Zn_d) shifts the Zn d band close to the core region. But even for U=0 eV the position of the Zn d states lies at the bottom VB, and the features at the upper VB are not affected by the Zn d states. It is also remarkable the low influence of the A or B position of Zn on the global features of the DOS.

When non-magnetic Zn cations enter NFO replacing Ni, the magnetic

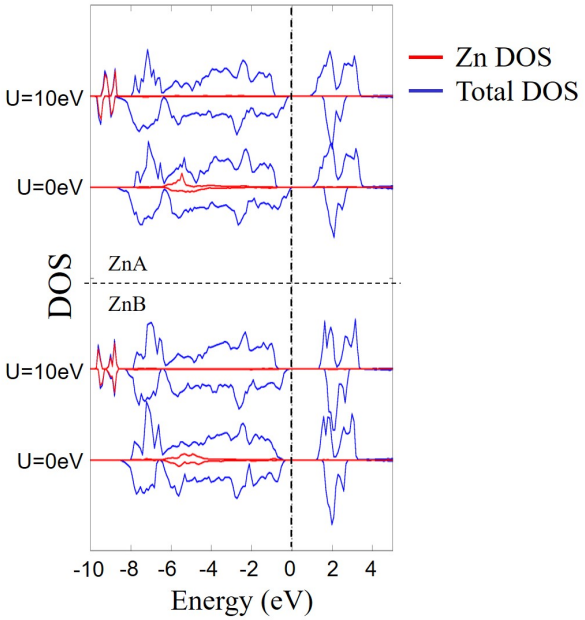

Figure 7.1: Spin-resolved DOS of $Zn_xNi_{1-x}Fe_2O_4$ with x=0.25 under different U(Zn_d) for Zn at A (top curves) and B (bottom curves) sites. The Zn d states are marked in red.

order may be altered. We have considered the possible couplings between the different magnetic sublattices c0-c3 shown in Table 4.1, analyzing their relative stability as a function of U(Zn_d). Combining all these configurations with different U(Zn_d) values implies a considerable number of simulations. To reduce the computational cost, first we have checked the smooth dependence of the system features on U(Zn_d), restricting to the unrelaxed structures. From this evidence, we will restrict the detailed analysis of the relaxed structures to only a few U(Zn_d) values. Relaxation does not modify the cubic symmetry for Zn_A, but it introduces a slight deformation when Zn occupies B sites. In both cases there is also an enlargement of the unit cell volume with respect to NFO, of 0.3% in the case of Zn_A and 0.2% for Zn_B, which is consistent with the experimental evidence [160]. This enlargement of the unit cell can be ascribed to the larger size of Zn ions as compared to Ni. In addition, and similarly to the situation at ZFO, U(Zn_d) = 0 eV stabilizes a volume larger by 0.15Å^3/atom than U(Zn_d) = 10 eV.

Figure 7.2 shows the relative stability of the different magnetic orders after relaxing the structure at each magnetic configuration for different U(Zn_d). We can see that U(Zn_d) has a negligible effect on the magnetic energy barriers at a fixed Zn site, with c0 always as the ground state. Also, the presence

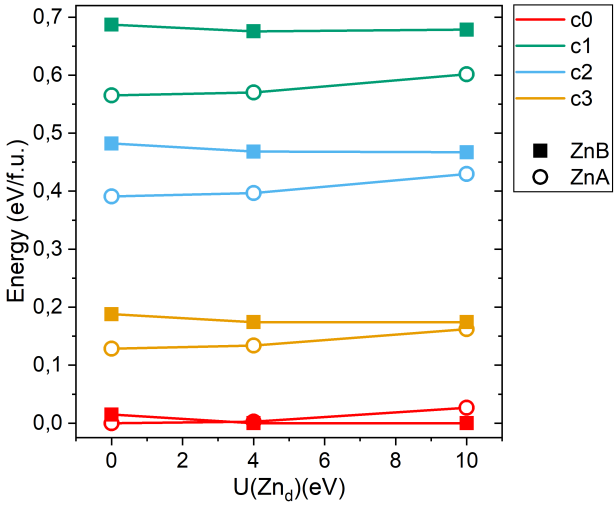

Figure 7.2: Evolution with U(Zn_d) of the relative stability of different magnetic configurations for ZNFO at x = 0.25, considering Zn at A (empty circles) or B (filled squares) sites.

of Zn does not seem to alter significantly the hierarchy between magnetic orders observed at pure NFO. However, an important conclusion from Figure 7.2 is the low energy difference between Zn_A and Zn_B, particularly at c0. Moreover, the choice of U(Zn_d) influences which position becomes more stable: Zn_A (Zn_B) is favored at the lowest (highest) U(Zn_d). These results support the diversity of experimental evidences, claiming the presence of Zn atoms both at octahedral and tetrahedral sites [139, 140, 141, 142, 160, 174].

In Figure 7.3 we show the evolution with U(Zn_d) of the spin-resolved DOS of unrelaxed $Zn_xNi_{1-x}Fe_2O_4$ at x=0.25 under the magnetic configurations c0-c3 shown in Table 4.1, considering Zn both at tetrahedral and octahedral sites. The results prove the smooth shift of the Zn *d* band with U(Zn_d), and the independence of the global electronic features from the position of the Zn *d* states, as described in figure 7.2 for the relaxed structures.

Figure 7.4 shows the evolution with U(Zn_d) of the total energy and internal pressure of these systems, the upper panel being equivalent to Figure 7.2, but referred to the unrelaxed structures. Again the figure reflects a smooth dependence on U(Zn_d). It is also evident the robust stability of the ground state magnetic configuration of NFO, c0, no matter the Zn position or the U(Zn_d) value. The most notable difference with respect to the relaxed structures is the relative stability of Zn_A and Zn_B, although with and without relaxation Zn_A tends to be favored as U(Zn_d) increases.

The internal pressure at the lower panel of Figure 7.4 is a measure of how

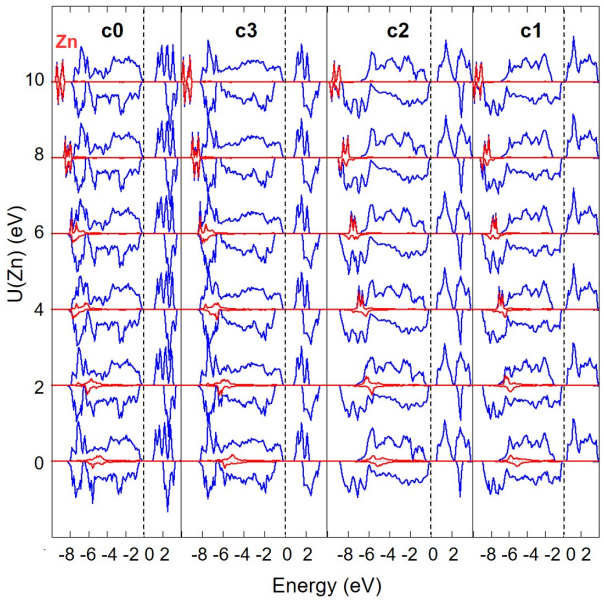

(a)

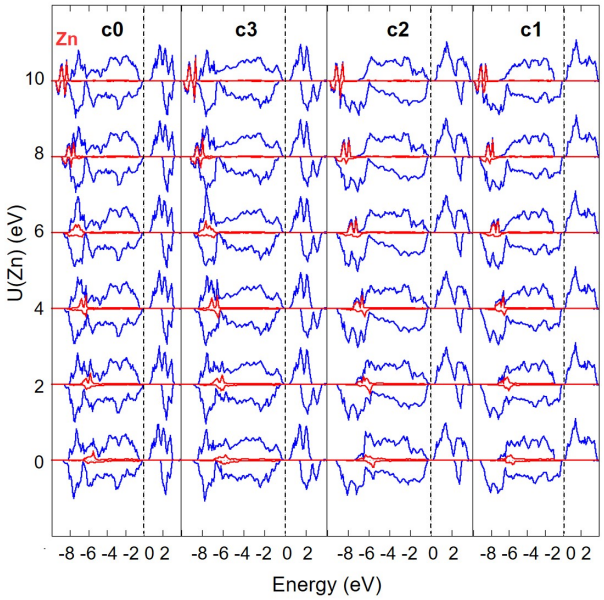

(b)

Figure 7.3: Evolution with U(Zn_d) of the spin-resolved DOS of unrelaxed ZNFO under x=0.25. Majority (minority) spin contributions are shown as positive (negative) values. a) and b) correspond to Zn at octahedral and tetrahedral sites respectively, while each column refers to a different magnetic order. The projection of the Zn states is represented by the red line.

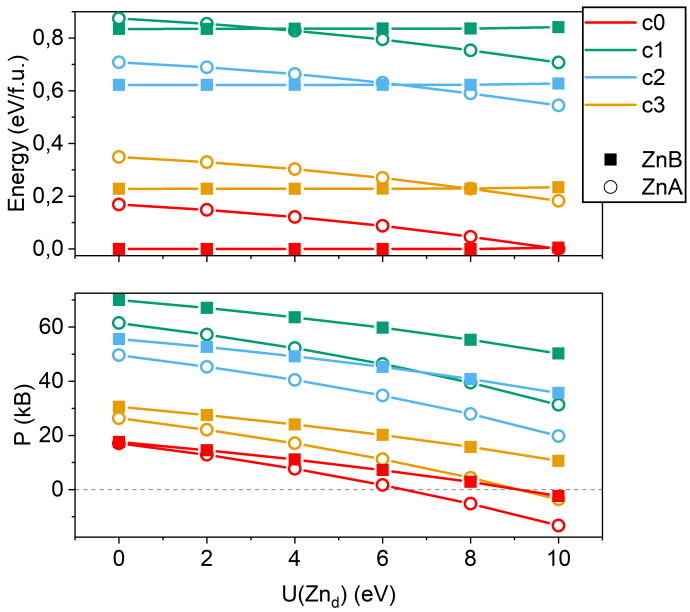

Figure 7.4: Evolution with U(Zn_d) of the total energy (top) and the internal pressure (bottom) of unrelaxed ZNFO at x = 0.25 under the magnetic configurations in Table 4.1. Structures with Zn at A (B) positions are represented by an empty circles (filled squares). The energy zero at each U(Zn_d) has been set at the most stable structure.

comfortable is the system at the lattice parameter used in the calculation (that of NFO in our case). It goes to zero at the equilibrum volume. Figure 7.4 reflects the same results shown in the main text for the relaxed structures: the lattice contracts as U(Zn_d) increases, something already observed at ZFO. In addition, there is a different dependence with U(Zn_d) of the equilibrium volume for Zn_A and Zn_B, which correlates with the relative stabilities observed in the upper panel. This justifies why the relative stability of Zn_A and Zn_B varies with U(Zn_d) when the NFO lattice is kept fixed, while they become almost degenerate when the structure is allowed to relax.

This study of the energetics enables a detailed analysis of the magnetic exchange interactions. Following the procedure explained in 2.4, we map our *ab initio* total energy differences to a Heisenberg model of the form given in equation 2.33. The procedure requires the simulation of different magnetic couplings, sometimes far away from equilibrium. As we will see, if such configurations do not lie in a local energy minimum, it may become impossible to find convergence, and thus to extract the corresponding J_{ij}. As our system is formed by three different magnetic sublattices, Ni, Fe_A and

	Fe_A	Fe_B	Ni
Fe_A	J_{AA}	J_{AB}	J_{NA}
Fe_B		J_{BB}	J_{NB}
Ni			J_{NN}

Table 7.1: Magnetic exchange interactions between magnetic sublattices at ZNFO. As $J_{XY} = J_{YX}$, for clarity we only show the upper part of the Table.

Fe_B, we again end up with six different exchange coupling constants, shown in Table 7.1. We will refer to this set of six J_{ij} as Js from now on.

The influence on the Js of the Zn distribution for different values of $U(Zn_d)$ is represented in Figure 7.5. We could not converge values for J_{NA} and J_{NN} at Zn_A under $U(Zn_d) = 10$ eV. As could be inferred from the robust stability of c0 shown in Figure 7.2, the dominance of the antiferromagnetic exchange interactions between cations at octahedral and tetrahedral sites (J_{AB}, J_{NA}) is maintained, no matter the Zn position or the value of $U(Zn_d)$. There are also some changes of sign of the weakest interactions, but their low values make negligible their influence on the magnetic order. Under $U(Zn_d)$=10 eV, apart from the slight reduction of the dominant exchange constants J_{AB}, J_{NA}, the most relevant effect is the noticeable increase of J_{BB}, that starts to compete with J_{AB}, J_{NA}. The antiferromagnetic alignment of Fe_B cations due to the reduction of the exchange coupling between A and B sublattices has already been suggested at ZFO [96]. Here, though this altered balance of antiferromagnetic interactions could destabilize c0, it also deteriorates the magnetic order at c1, c2, c3, and the result is the low influence of $U(Zn_d)$ on the energy barrier between the different magnetic configurations observed in Figure 7.2

Restricting now to the ground state magnetic order c0, we have found no significant influence of $U(Zn_d)$ neither on the Bader charges nor in the local magnetic moments. This becomes evident at Table 7.2, that compiles the average magnetic moment of each atomic species for different $U(Zn_d)$, both for Zn_A and Zn_B. As a reference, ZFO and NFO are also shown. Some values are marked with a plus/minus sign, indicating that each half of the corresponding atoms of the sublattice take a different orientation (leading to a null mean value). We focus on case x=0.25. Only the Zn position, either Zn_A and Zn_B, introduces some minor differences in the local magnetic moments, the largest effect emerging at the hybridized moments acquired by the non-magnetic atoms. However, the net magnetization of the entire system is significantly modified depending on the Zn site, because the balance between magnetic A and B sublattices is altered by the presence of non-

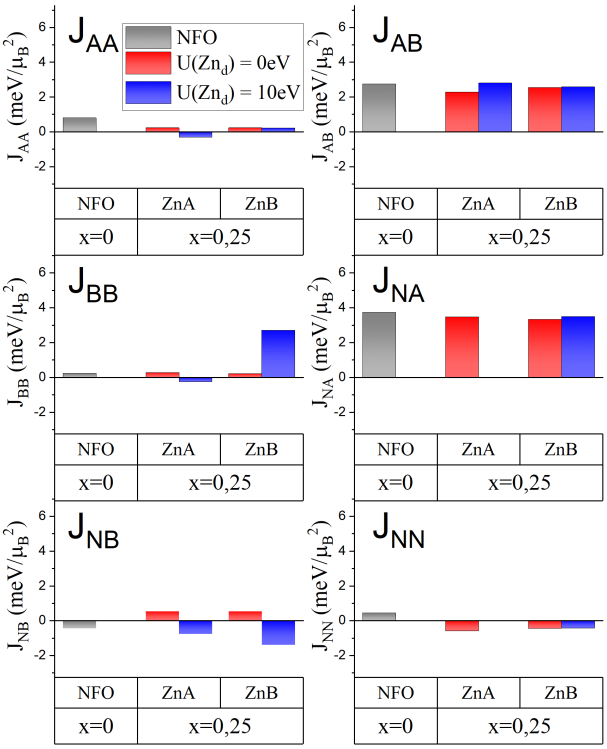

Figure 7.5: Exchange coupling constants at ZNFO under x=0.25 with Zn either at A or B sites. As a reference, the Js of NFO are also provided.

Structure	Zn position	U(Zn_d) (eV)	O	Fe_B	Fe_A	Ni	Zn	Total
NFO			0.07	4.12	-3.97	1.60		2.0
ZFO	Inverse	0	±0.05	4.17	-4.14		-0.02	0.0
		10	±0.05	4.17	-4.12		-0.03	0.0
	Direct	0	±0.11	±4.21			0.00	0.0
		10	±0.11	±4.22			0.00	0.0
ZNFO x=0.25	Zn_A	0	0.15	4.16	-4.02	1.61	0.06	4.0
		10	0.15	4.15	-4.02	1.61	0.06	4.0
	Zn_B	0	0.06	4.13	-4.04	1.59	-0.03	1.5
		10	0.06	4.13	-4.04	1.58	-0.02	1.5
ZNFO x=0.50	Zn_A	0	0.15	4.16	-4.02	1.61	0.06	4.0
		10	0.15	4.15	-4.02	1.61	0.06	4.0
	Zn_B	0	0.06	4.13	-4.04	1.59	-0.03	1.5
		10	0.06	4.13	-4.04	1.58	-0.02	1.5
	Zn_{AB}	0	0.06	4.13	-4.04	1.59	-0.03	1.5
		10	0.06	4.13	-4.04	1.58	-0.02	1.5

Table 7.2: Local magnetic moments of the different chemical species at NFO, ZFO and $Zn_xNi_{1-x}Fe_2O_4$ with x=0.25, 0.50, for Zn at octahedral (B) or tetrahedral (A) sites, and different U(Zn_d). The total magnetization per formula unit is also shown in the last column.

magnetic Zn atoms. As a result, Zn_A doubles the magnetization of NFO, while Zn_B reduces it by 25%.

Finally, we have determined the magnetic anisotropy energy computing the total energy of configurations with the magnetization oriented along the [001], [010], [100], [110] and [111] axes. The resulting MAE is somewhat reduced compared to the value of 0.021 meV/Fe at pure NFO, lying around 0.017 meV/Fe and 0.016 meV/Fe for Zn_A and Zn_B respectively, which is close to our accuracy limit in the determination of the MAE. In all cases the easy axis at [110] is maintained. This is in good agreement with experimental results, where the coercivity of the material reduces with the increase of Zn content [139, 160].

7.4 x=0.50

Substituting two Zn cations at our unit cell of 28 atoms is equivalent to a concentration x=0.50. Now there are more possible atomic arrangements, with both Zn cations at A sites (Zn_A), both at B sites (Zn_B), or each one at a different coordination site (Zn_{AB}). In addition, each situation admits dif-

ferent Zn-Zn interatomic distances and different Ni distributions. Addressing a detailed study of diverse magnetic configurations under all these possibilities is a computational challenge out of the scope of this study. Instead, we analyze the most stable conditions for configurations Zn_A, Zn_B and Zn_{AB}.

Figure 7.6 shows the different atomic arrangements considered for ZNFO at x=0.50, named according to the distribution of Zn atoms at A and B sites. The corresponding relative distance between Zn-Zn closest neighbours is also provided. Modifying the distribution of Zn at B sites necessary alters that of Ni, and different combinations have been taken into account. Our calculations do not pretend to cover exhaustively all possibilities, but to identify the most stable structures, and the existence or not of a competition between configurations Zn_A, Zn_B and Zn_{AB} that may affect the magnetic properties of the system.

The relative stability of each of these relaxed structures is shown in figure 7.7a as a function of $U(Zn_d)$. The most relevant feature is the strong dependence of the atomic distribution on $U(Zn_d)$, that affects mainly the hierarchy between configurations Zn_A and Zn_B. But in general the energy differences are low, evidencing that all these structures may be found at real samples. The results also indicate a tendency to favor sparse Zn distributions, even though the interatomic distance between Zn neighbours is not determinant. Other factors, as the distribution of Ni atoms, also influence the final energy of the system.

It is known that the arrangement of Ni atoms does not have relevant consequences on the magnetism of NFO. Here, we have confirmed that, for each selected configuration (Zn_A, Zn_B or Zn_{AB}), nor the local moments neither the net magnetization of the different structures in Figure 7.6 show any variation. In addition, both values of $U(Zn_d)$ identify the same structure as the most stable for each configuration, allowing us to restrict our detailed study of the magnetic properties to three representative cases, namely, 2ZnA-3, 2ZnB-1 and ZnAB-1.

According to this choice, Figure 7.7b shows the relative stability of Zn_A, Zn_B and Zn_{AB}, after full structural relaxation and at the magnetic ground state, c0. The figure is just a simplification of Figure 7.7a, and thus it again evidences that different Zn distributions may coexist, and $U(Zn_d)$ has a large influence on the identification of the most stable one. Similarly to x=0.25, Zn_B is favoured over Zn_A under large $U(Zn_d)$. Further, independently of $U(Zn_d)$, the simultaneous presence of Zn atoms at both A and B sites cannot be discarded, and it corresponds to the most stable situation under $U(Zn_d)$= 0 eV.

The structural features after relaxation keep trends similar to those observed at x=0.25 and ZFO. Always $U(Zn_d) = 0$ eV leads to higher volumes

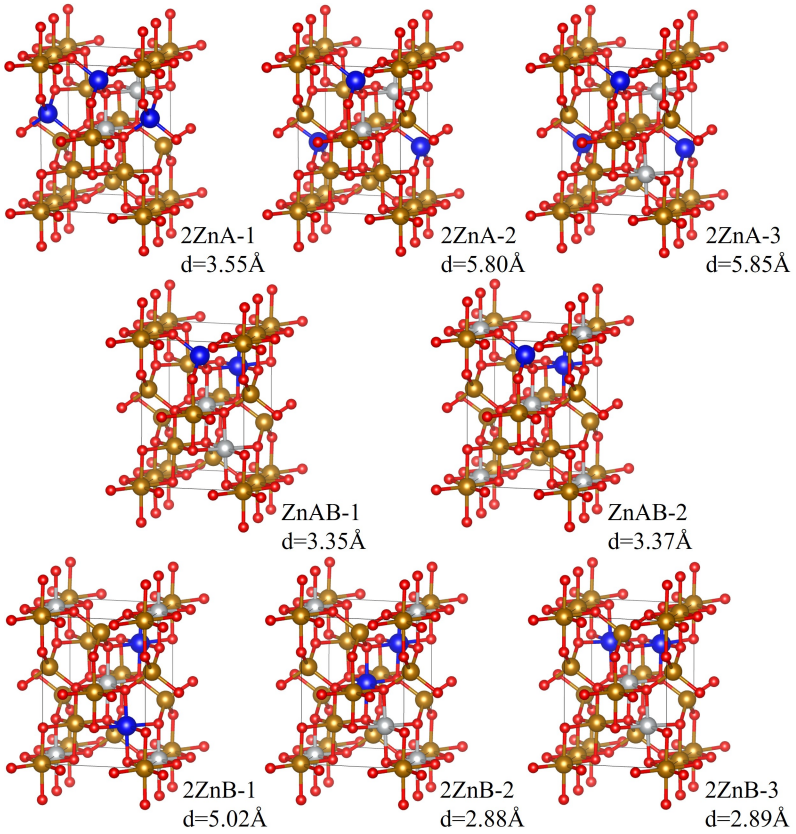

Figure 7.6: Structure of the different atomic distributions considered for ZNFO at x=0.50 under configurations Zn_A, Zn_B and Zn_{AB}, indicating at each one the shortest Zn-Zn interatomic distance after relaxation. Zn, Ni, Fe and O atoms are represented respectively by blue, white, golden and red spheres.

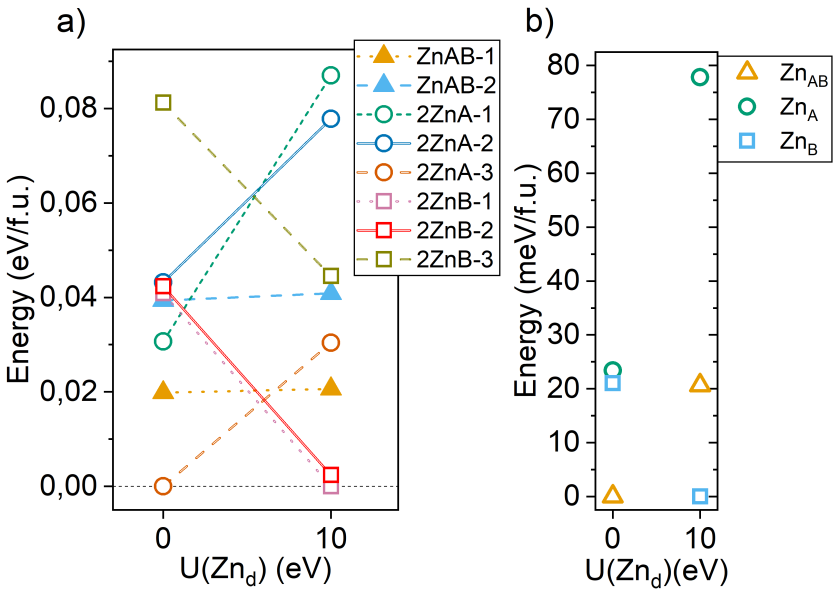

Figure 7.7: a) Total energy of relaxed ZNFO with x = 0.5 at the magnetic ground state c0 for the different Zn distributions shown in Figure 7.6. The energy zero at each U(Zn_d) has been set at the most stable structure. The line is a guide to the eye. b) Total energy of the most stable Zn distribution of ZNFO at x=0.50 under configurations Zn_A, Zn_B and Zn_{AB}.

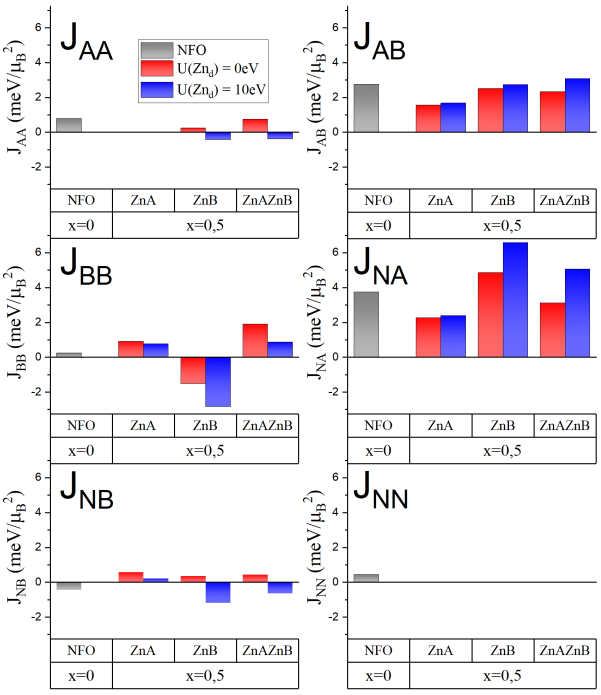

Figure 7.8: Same as Figure 7.5 for x=0.50 under the different Zn distributions at Figure 7.7b.

than U(Zn_d) = 10 eV (about 0.3 Å^3/atom above), while Zn_A tends to slightly expand the lattice over Zn_B (by 0.05 Å^3/atom). The volume of the unit cell is enlarged by 0.4% with respect to pure NFO, again consistent with the experimental evidence [160], and as expected from the increase in the number of Zn atoms in the structure.

Regarding the energy barrier between different magnetic configurations, here the trends are similar to those observed at lower Zn concentrations: c0 is a robust magnetic ground state, and the presence of Zn cations at B sites reinforces its stability. Figure 7.8 shows the magnetic exchange constants, obtained following the procedure explained in the previous subsection. It is evident the dominance of the antiferromagnetic exchange between cations at A and B sites, supporting the stability of c0. Further, there is a strong dependence of the Js on the Zn distribution, though in general the hierarchy between the relative J_{ij} strengths is preserved. The only exception is the enhancement and sign reversal of J_{BB} when Zn occupies only B sites. This result is affected by the specific structure used to extract the Js, 2ZnB-1, where Fe_B atoms are not nearest neighbors. This result puts a word of caution before extracting conclusions about the detailed balance of exchange

interactions without a more thorough consideration of different atomic distributions. However, the general trends evidenced in Figure 7.8 suggest that still at x=0.50 the antiferromagnetic coupling between A and B sublattices is the dominant magnetic interaction, that guarantees the stability of c0. Last, it is also noticeable the tendency to increase the Js under U(Zn_d) = 10 eV, not observed at x=0.25, and that here manifests as more relevant when there are Zn atoms at B positions.

The magnetization and local magnetic moments at c0 are in the lower part of Table 7.2. In general, the net magnetization is again enlarged under Zn_A, as more Fe atoms are forced to move to octahedral positions, with a record enhancement of $4.0\mu_B$/f.u. over pure NFO. However, the individual magnetic moments do not vary noticeably depending on the Zn position. There is only a slight reduction of the moments of the B cations under Zn_B, and more dispersed values for the non-magnetic atoms depending on the Zn distribution.

Finally, our results for the MAE indicate a further reduction as the Zn content increases, with values between 0.010 - 0.014 meV/Fe depending on the Zn positions. This is consistent with the experimental evidence of a reduction of the coercive field as the Zn content increases.

7.5 Conclusions

We have addressed the study of Zn substituted NFO $Zn_xNi_{1-x}Fe_2O_4$ for x=0.25, 0.50. As observed for ZFO, the position of the Zn *d* states at the VB, tuned by the U(Zn_d) value, has a negligible effect on the global magnetic properties and the electronic structure. Its main effect relies on the relative stability of the A or B site for Zn substitution. However, no matter U(Zn_d), in all cases there is evidence of the low energy barrier between both situations, supporting the coexistence of Zn_A and Zn_B. This explains the diversity of experimental results. Further, such coexistence has consequences on the lattice volume, as Zn_A favors a larger expansion over the NFO lattice. Also, the magnetic properties are largely dependent on the Zn distribution. While the ferrimagnetic ground state c0 is preserved up to x=0.50 for all atomic arrangements, differences emerge regarding the competition between local exchange interactions. The dominance of the antiferromagnetic exchange between A and B magnetic sublattices seems robust, but the detailed atomic distribution may alter significantly the strength and sign of other exchange interactions. Regarding the partial substitution of Ni by Zn atoms as a route to enhance the net magnetization, our results indicate that it is severely limited by the coexistence of Zn_A and Zn_B. Finally, the magnetocrystalline

anisotropy is weakened with the increase of the Zn content, ensuring ZNFO as a robust soft magnet, in good agreement with the experimental evidence.

Chapter 8

Conclusions

A comprehensive study at the DFT+U level of the electronic, magnetic and structural properties of ferrite systems relevant for permanent magnet applications has been addressed. For some materials, as cubic spinel ferrites, there were previous accurate DFT+U calculations in the literature, while for others such as bulk SFO, NZFO or the interface structures, our simulations are pioneer and provide the first fundamental determination of properties such as the electronic band gap, local magnetic moments or magnetic anisotropy. On one hand, we have identified the relevant theoretical conditions to describe each system, demonstrating in particular the crucial role of the choice of U not only in the resulting electronic band gap, but also on the magnetism of the systems, either directly or through the influence on the structural features. On the other hand, we provide an accurate description of the magnetic properties at the atomic level, that helps in the design of improved rare-earth free permanent magnets and can be further used as starting point in multiscale magnetic simulations.

In the following we provide a more detailed list of conclusions specific for each system considered. First, regarding the bulk materials, the main outcome of our work is the following:

- We provide the first accurate fundamental description of SFO at the DFT+U level, identifying U$\approx$ 2-3 eV as the most adequate value to capture the physical properties of SFO. In contrast to previous works on other hexaferrites, our approach includes all magnetic properties as targets to identify the appropriate U value, to demonstrate their importance in order to avoid inconsistencies and the need of artificially high U values in the description of these materials.

- In the same spirit, we revisit the DFT+U description of ZFO paying special attention to the value of U at the Zn d band. Our results

demonstrate its relevance on the magnetism of the system through an indirect effect: the relative stability of the direct and inverse forms of ZFO. Both forms show completely different magnetic behaviors, ranging from the stable ferrimagnetism of the inverse form to the complex antiferromagnetism of direct ZFO. Thus, their relative presence in a sample has a determinant role in its magnetic response.

- We have set the accuracy limits imposed by the different approximations (*i.e.* static vs. dynamical limits, structural effects, etc.) inherent to the mapping of *ab initio* total energies into a Heisenberg model to extract fundamental exchange constants, both for cubic ferrites and SFO. We conclude the validity of a Heisenberg-like behavior in these systems.

- We determine the relevance of beyond-mean-field approximations to extract accurate magnetic ordering temperatures from *ab initio* inputs in the ferrites under consideration. Monte Carlo simulations have been used here to estimate T_N values close to experiment in the case of SFO, and slightly overestimated for CFO.

Concerning modifications of the bulk forms intended to improve the performance of nanostructured permanent magnets based on these materials, we have focused on the substitution of Ni by Zn at NFO, and in the determination of the interface contribution to the magnetic properties at bicomponent systems based on CFO and a soft cubic spinel (NFO, MFO).

- Our results demonstrate that inclusion of substitutional Zn replacing Ni at NFO alters the ferrimagnetic configuration, limiting the ability of Zn to increase the magnetization of the system over undoped NFO. First, and most importantly, Zn has similar tendencies to occupy tetrahedral or octahedral positions, with opposite effects on the net magnetization. Further, the presence of Zn alters the strength and sign of the local exchange interactions, even though the antiferromagnetic exchange between A and B sublattices keeps dominant.

- The similar structure of NFO and CFO allows to build ideal interfaces free from mismatch and strain effects. We show that this way the role of the interface on the magnetism of the combined system is low, with essentially no influence on the local features. In turn, the combination of both oxides contributes with an additive effect to the net magnetization, limiting the use of the bicomponent system as an improved spring magnet. On the other hand, the magnetic anisotropy is significantly

altered by the presence of the interface, and though the bulk easy axis is preserved, the cost to rotate the magnetization is reduced with respect to bulk CFO, and depends on the specific terminations present at the interface.

- The presence of strain at bicomponent CFO/MFO introduces larger modifications, even though the net magnetization and stability of the bulk-like ferrimagnetism are preserved. However, local spin distributions are significantly altered, and the magnetic moments are slightly enhanced at the interface. The coexistence of different Co distributions summed to strain effects at CFO tend to harden the [001] as easy axis, while strained MFO tends to weaken exchange interactions at the direct form.

- Finally, at all interface systems considered, the degree of inversion of CFO plays an essential role in the efficiency of the bicomponent systems as permanent magnets. This is an expected result as inverse and direct CFO behave respectively as hard and soft magnets. Our results serve to quantify the modification of the magnetic properties induced by the presence of direct CFO, that can be used as an indirect evidence to detect its presence in real samples.

Bibliography

[1] Jeotikanta Mohapatra and Jia Ping Liu. Chapter 1 - rare-earth-free permanent magnets: The past and future. volume 27 of *Handbook of Magnetic Materials*, pages 1–57. Elsevier, 2018.

[2] J. M. D. Coey. Hard magnetic materials: A perspective. *IEEE Transactions on Magnetics*, 47(12):4671–4681, 2011.

[3] J.M.D. Coey. Permanent magnets: Plugging the gap. *Scripta Materialia*, 67(6):524–529, 2012. Viewpoint Set No. 51: Magnetic Materials for Energy.

[4] D Goll, R Loeffler, J Herbst, R Karimi, and G Schneider. High-throughput search for new permanent magnet materials. *Journal of Physics: Condensed Matter*, 26(6):064208, jan 2014.

[5] Francisco Javier Pedrosa Ruiz. *Towards ferrite based rare-earth free permanent magnets: from model systems to new technological applications*. PhD thesis, 2017.

[6] Alexander King. 1 - what happened to the rare earths? monopoly, price shock, and the idea of a critical material. In Alexander King, editor, *Critical Materials*, Materials Today, pages 1–17. Elsevier, 2021.

[7] European Commission. *Critical raw materials for the EU: Report of the Ad-hoc Working Group on defining critical raw materials*, June 2010.

[8] E. A. Périgo, B. Weidenfeller, P. Kollár, and J. Füzer. Past, present, and future of soft magnetic composites. *Applied Physics Reviews*, 5(3):031301, 2018.

[9] Alberto López-Ortega, Marta Estrader, German Salazar-Alvarez, Alejando G. Roca, and Josep Nogués. Applications of exchange coupled bi-magnetic hard/soft and soft/hard magnetic core/shell nanoparticles. *Physics Reports*, 553:1–32, 2015. Applications of exchange coupled bi-magnetic hard/soft and soft/hard magnetic core/shell nanoparticles.

[10] C. Della Pina, E. Falletta, A. M. Ferretti, A. Ponti, G. G. Gentili, V. Verri, and R. Nesti. Microwave characterization of magnetically hard and soft ferrite nanoparticles in k-band. *Journal of Applied Physics*, 116(15):154306, 2014.

[11] J.H. Lee, Jt. Jang, and Js. *et al* Choi. Exchange-coupled magnetic nanoparticles for efficient heat induction. *Nature Nanotechnology*, 6:418–422, 2011.

[12] Rostislav V. Lapshin. An improved parametric model for hysteresis loop approximation. *Review of Scientific Instruments*, 91(6):065106, 2020.

[13] E.F. Kneller and R. Hawig. The exchange-spring magnet: a new material principle for permanent magnets. *IEEE Transactions on Magnetics*, 27(4):3588–3560, 1991.

[14] Ralph Skomski and J. M. D. Coey. Giant energy product in nanostructured two-phase magnets. *Phys. Rev. B*, 48:15812–15816, Dec 1993.

[15] W. Rodewald, B. Wall, M. Katter, and K. Uestuener. Top nd-fe-b magnets with greater than 56 mgoe energy density and 9.8 koe coercivity. *IEEE Transactions on Magnetics*, 38(5):2955–2957, 2002.

[16] Qian Zhang, Idoia Castellanos-Rubio, Rahul Munshi, Iñaki Orue, Beatriz Pelaz, Katharina Ines Gries, Wolfgang J. Parak, Pablo del Pino, and Arnd Pralle. Model driven optimization of magnetic anisotropy of exchange-coupled core–shell ferrite nanoparticles for maximal hysteretic loss. *Chemistry of Materials*, 27(21):7380–7387, 2015.

[17] Qing Song and Z. John Zhang. Controlled synthesis and magnetic properties of bimagnetic spinel ferrite cofe2o4 and mnfe2o4 nanocrystals with core–shell architecture. *Journal of the American Chemical Society*, 134(24):10182–10190, 2012. PMID: 22621435.

[18] D. Polishchuk, N. Nedelko, S. Solopan, A. Slawska-Waniewska, V. Zamorskyi, A. Tovstolytkin, and A. Belous. Profound interfacial effects in $cofe_2o_4/fe_3o_4$ and $fe_3o_4/cofe_2o_4$ core/shell nanoparticles. *Nanoscale Research Letters*, 13(67), 2018.

[19] Samuel D. Oberdick, Ahmed Abdelgawad, Carlos Moya, Samaneh Mesbahi-Vasey, Demie Kepaptsoglou, Vlado K. Lazarov, Richard F. L. Evans, Daniel Meilak, Elizabeth Skoropata, Johan van Lierop, Ian Hunt-Isaak, Hillary Pan, Yumi Ijiri, Kathryn L. Krycka, Julie A.

Borchers, and Sara A. Majetich. Spin canting across core/shell $fe_3o_4/mn_xfe_{3x}o_4$ nanoparticles. *Scientific Reports*, 8(1):3425, Feb 2018.

[20] Chapter 7 - exchange mechanisms. In *Correlated Electrons: From Models to Materials*, Handbook of Magnetic Materials. Jülich.

[21] John B. Goodenough. Theory of the role of covalence in the perovskite-type manganites $[\mathrm{La}, m(\mathrm{II})]\mathrm{Mno}_3$. *Phys. Rev.*, 100:564–573, Oct 1955.

[22] Junjiro Kanamori. Superexchange interaction and symmetry properties of electron orbitals. *Journal of Physics and Chemistry of Solids*, 10(2):87 – 98, 1959.

[23] Natalya S. Fedorova, Claude Ederer, Nicola A. Spaldin, and Andrea Scaramucci. Biquadratic and ring exchange interactions in orthorhombic perovskite manganites. *Phys. Rev. B*, 91:165122, Apr 2015.

[24] M. Born and R. Oppenheimer. Zur quantentheorie der molekeln. *Annalen der Physik*, 389(20):457–484, 1927.

[25] R. P. Feynman. Forces in molecules. *Phys. Rev.*, 56:340–343, Aug 1939.

[26] L. H. Thomas. The calculation of atomic fields. *Mathematical Proceedings of the Cambridge Philosophical Society*, 23(5):542–548, 1927.

[27] E. Fermi. Un metodo statistico per la determinazione di alcune prorieta dell'atomo. *Rend Accad Naz Lincei*, 6:602–607, 01 1927.

[28] P. Hohenberg and W. Kohn. Inhomogeneous electron gas. *Phys. Rev.*, 136:B864–B871, Nov 1964.

[29] W. Kohn and L. J. Sham. Self-consistent equations including exchange and correlation effects. *Phys. Rev.*, 140:A1133–A1138, Nov 1965.

[30] U von Barth and L Hedin. A local exchange-correlation potential for the spin polarized case. i. *Journal of Physics C: Solid State Physics*, 5(13):1629–1642, jul 1972.

[31] A. K. Rajagopal and J. Callaway. Inhomogeneous electron gas. *Phys. Rev. B*, 7:1912–1919, Mar 1973.

[32] R. O. Jones. Density functional theory: Its origins, rise to prominence, and future. *Reviews of Modern Physics*, 87:897–923, 2015.

[33] John P. Perdew, Kieron Burke, and Matthias Ernzerhof. Generalized gradient approximation made simple. *Phys. Rev. Lett.*, 77:3865–3868, Oct 1996.

[34] John P. Perdew, Adrienn Ruzsinszky, Gábor I. Csonka, Oleg A. Vydrov, Gustavo E. Scuseria, Lucian A. Constantin, Xiaolan Zhou, and Kieron Burke. Restoring the density-gradient expansion for exchange in solids and surfaces. *Physical Review Letters*, 100(13), Apr 2008.

[35] S. L. Dudarev, G. A. Botton, S. Y. Savrasov, C. J. Humphreys, and A. P. Sutton. Electron-energy-loss spectra and the structural stability of nickel oxide: An lsda+u study. *Phys. Rev. B*, 57:1505–1509, Jan 1998.

[36] M. Springer and F. Aryasetiawan. Frequency-dependent screened interaction in ni within the random-phase approximation. *Phys. Rev. B*, 57:4364–4368, Feb 1998.

[37] W Tang, E Sanville, and G Henkelman. A grid-based bader analysis algorithm without lattice bias. *Journal of Physics: Condensed Matter*, 21(8):084204, jan 2009.

[38] H. Hellmann. A new approximation method in the problem of many electrons. *The Journal of Chemical Physics*, 3(1):61–61, 1935.

[39] P. E. Blöchl. Projector augmented-wave method. *Phys. Rev. B*, 50:17953–17979, Dec 1994.

[40] J. Cerdá, M. A. Van Hove, P. Sautet, and M. Salmeron. Efficient method for the simulation of STM images. i. generalized green-function formalism. *Physical Review B*, 56(24):15885–15899, December 1997.

[41] E. T. R. Rossen, C. F. J. Flipse, and J. I. Cerdá. Lowest order in inelastic tunneling approximation: Efficient scheme for simulation of inelastic electron tunneling data. *Physical Review B*, 87(23), June 2013.

[42] Soner Steiner, Sergii Khmelevskyi, Martijn Marsmann, and Georg Kresse. Calculation of the magnetic anisotropy with projected-augmented-wave methodology and the case study of disordered $\mathrm{fe}_{1-x}\mathrm{co}_x$ alloys. *Phys. Rev. B*, 93:224425, Jun 2016.

[43] Peitao Liu, Sergii Khmelevskyi, Bongjae Kim, Martijn Marsman, Dianzhong Li, Xing-Qiu Chen, D. D. Sarma, Georg Kresse, and Cesare Franchini. Anisotropic magnetic couplings and structure-driven

canted to collinear transitions in sr_2iro_4 by magnetically constrained noncollinear dft. *Phys. Rev. B*, 92:054428, Aug 2015.

[44] R Cuadrado and J I Cerdá. Fully relativistic pseudopotential formalism under an atomic orbital basis: spin–orbit splittings and magnetic anisotropies. *Journal of Physics: Condensed Matter*, 24(8):086005, jan 2012.

[45] Alberto García, Nick Papior, Arsalan Akhtar, Emilio Artacho, Volker Blum, Emanuele Bosoni, Pedro Brandimarte, Mads Brandbyge, J. I. Cerdá, Fabiano Corsetti, Ramón Cuadrado, Vladimir Dikan, Jaime Ferrer, Julian Gale, Pablo García-Fernández, V. M. García-Suárez, Sandra García, Georg Huhs, Sergio Illera, Richard Korytár, Peter Koval, Irina Lebedeva, Lin Lin, Pablo López-Tarifa, Sara G. Mayo, Stephan Mohr, Pablo Ordejón, Andrei Postnikov, Yann Pouillon, Miguel Pruneda, Roberto Robles, Daniel Sánchez-Portal, Jose M. Soler, Rafi Ullah, Victor Wen zhe Yu, and Javier Junquera. Siesta: Recent developments and applications. *The Journal of Chemical Physics*, 152(20):204108, May 2020.

[46] M. Weinert, R. E. Watson, and J. W. Davenport. Total-energy differences and eigenvalue sums. *Physical Review B*, 32(4):2115–2119, August 1985.

[47] M Blanco-Rey, J I Cerdá, and A Arnau. Validity of perturbative methods to treat the spin-orbit interaction: application to magnetocrystalline anisotropy. *New Journal of Physics*, 21(7):073054, jul 2019.

[48] Chuanjian Wu, Zhong Yu, Ke Sun, Jinlan Nie, Rongdi Guo, Hai Liu, Xiaona Jiang, and Zhongwen Lan. Calculation of exchange integrals and curie temperature for la-substituted barium hexaferrites. *Scientific Reports*, 6:36200 EP –, Oct 2016. Article.

[49] R F L Evans, W J Fan, P Chureemart, T A Ostler, M O A Ellis, and R W Chantrell. Atomistic spin model simulations of magnetic nanomaterials. *Journal of Physics: Condensed Matter*, 26(10):103202, feb 2014.

[50] Nicholas Metropolis, Arianna W. Rosenbluth, Marshall N. Rosenbluth, Augusta H. Teller, and Edward Teller. Equation of state calculations by fast computing machines. *The Journal of Chemical Physics*, 21(6):1087–1092, 1953.

[51] D. Ter Haar and M. E. Lines. A molecular-field theory of anisotropic ferromagnetica. *Philosophical Transactions of the Royal Society A*, 254, 1962.

[52] J.S. Smart. *Effective Field Theories of Magnetism.* Studies in physics and chemistry, 216. Saunders, 1966.

[53] W.R. Buessem B.T. Shirk. Temperature dependence of ms and k_1 of $bafe_{12}o_{19}$ and $srfe_{12}o_{19}$ single crystals. *AIP Journal of Applied Physics*, 40, 11 1969.

[54] Hiroaki Ueda, Yasuaki Tanioku, Chishiro Michioka, and Kazuyoshi Yoshimura. Magnetocrystalline anisotropy of la- and co-substituted M-type strontium ferrites: Role of co^{2+} and fe^{2+}. *Phys. Rev. B*, 95:224421, Jun 2017.

[55] Vivek Dixit, Seong-Gon Kim, Jihoon Park, and Yang-Ki Hong. Effect of ionic substitutions on the magnetic properties of strontium hexaferrite: A first principles study. *AIP Advances*, 7(11):115–209, 2017.

[56] Matilde Saura-Múzquiz, Cecilia Granados-Miralles, Henrik L. Andersen, Marian Stingaciu, Maxim Avdeev, and Mogens Christensen. Nanoengineered high-performance hexaferrite magnets by morphology-induced alignment of tailored nanoplatelets. *ACS Appl. Nano Mater*, 1:6938–6949, 2018.

[57] Cecilia Granados-Miralles, Matilde Saura-Múzquiz, Espen D. Bøjesen, Kirsten M. Ø. Jensen, Henrik L. Andersen, and Mogens Christensen. Unraveling structural and magnetic information during growth of nanocrystalline $srfe_{12}o_{19}$. *J. Mater. Chem. C*, 4:10903–10913, 2016.

[58] Ehsan Naderi, Mahmoud Naseri, and Dariush Souri. The effect of sio_2 and tio_2 nanoparticles on physical properties of $srfe_{12}o_{19}$ nanoparticle. *Current Applied Physics*, 18(4):469 – 476, 2018.

[59] Guiomar Delgado Soria, Petra Jenus, J. Marco, Anna Mandziak, María Sánchez Arenillas, F. Moutinho, J. Prieto, P. Prieto, Jorge Cerdá, C. Tejera-Centeno, Silvia Gallego, M. Foerster, Lucia Aballe, S. Valvidares, H. Vasili, Eva Pereiro, Adrian Quesada, and Juan de la Figuera. Strontium hexaferrite platelets: a comprehensive soft x-ray absorption and mössbauer spectroscopy study. *Scientific Reports*, 9, 12 2019.

[60] C M Fang, F Kools, R Metselaar, G de With, and R A de Groot. Magnetic and electronic properties of strontium hexaferrite $srfe_{12}o_{19}$ from

first-principles calculations. *Journal of Physics: Condensed Matter*, 15(36):6229–6237, aug 2003.

[61] E.W. Gorter. Saturation magnetization of some ferrimagnetic oxides with hexagonal crystal structures. *Proceedings of the IEE - Part B: Radio and Electronic Engineering*, 104:255–260(5), January 1957.

[62] P. Novak, K. Knizek, M. Küpferling, R. Grössinger, and M.W. Pieper. Magnetism of mixed valence (LaSr) hexaferrites. *The European Physical Journal B*, 43(4):509–515, feb 2005.

[63] P. Novák and J. Rusz. Exchange interactions in barium hexaferrite. *Physical Review B*, 71(18), may 2005.

[64] Laalitha S.I. Liyanage, Sungho Kim, Yang-Ki Hong, Ji-Hoon Park, Steven C. Erwin, and Seong-Gon Kim. Theory of magnetic enhancement in strontium hexaferrite through zn–sn pair substitution. *Journal of Magnetism and Magnetic Materials*, 348:75–81, dec 2013.

[65] Jihoon Park, Yang-Ki Hong, Seong-Gon Kim, Sungho Kim, Laalitha S.I. Liyanage, Jaejin Lee, Woncheol Lee, Gavin S. Abo, Kang-Heon Hur, and Sung-Yong An. Maximum energy product at elevated temperatures for hexagonal strontium ferrite (SrFe12o19) magnet. *Journal of Magnetism and Magnetic Materials*, 355:1–6, apr 2014.

[66] Vojtěch Chlan, Karel Kouřil, Kateřina Uličná, Helena Štěpánková, Jörg Töpfer, and Daniela Seifert. Charge localization and magnetocrystalline anisotropy in la, pr, and nd substituted sr hexaferrites. *Physical Review B*, 92(12), sep 2015.

[67] Vivek Dixit, Chandani N. Nandadasa, Seong-Gon Kim, Sungho Kim, Jihoon Park, Yang-Ki Hong, Laalitha S. I. Liyanage, and Amitava Moitra. Site occupancy and magnetic properties of al-substituted m-type strontium hexaferrite. *Journal of Applied Physics*, 117(24):243904, 2015.

[68] Wenming Sun, Liang Zhang, Jing Liu, Hong Wang, Yan Zuo, and Yuxiang Bu. First-principle study of the electronic structures and optical properties of six typical hexaferrites. *Computational Materials Science*, 105:27–31, jul 2015.

[69] A. Lyogenkaya, G. Grechnev, O. Kotlyar, A. Panfilov, and V. Gnezdilov. Electronic structure and magnetic properties of fete,

bifeo$_3$, srfe$_{12}$o$_{19}$ and srcotife$_{10}$o$_{19}$ compounds. *Ukrainian Journal of Physics*, 61(6):523, Jan. 2019.

[70] K. Momma and F. Izumi. Vesta 3 for three-dimensional visualization of crystal, volumetric and morphology data. *Journal of Applied Crystallography*, 44:1272–1276, 2011.

[71] S. L. Dudarev, G. A. Botton, S. Y. Savrasov, C. J. Humphreys, and A. P. Sutton. Electron-energy-loss spectra and the structural stability of nickel oxide: An lsda+u study. *Phys. Rev. B*, 57:1505–1509, Jan 1998.

[72] Sarah A. Tolba, Kareem M. Gameel, Basant A. Ali, Hossam A. Almossalami, and Nageh K. Allam. *The DFT+U: Approaches, Accuracy, and Applications*. InTech, May 2018.

[73] Matteo Cococcioni and Stefano de Gironcoli. Linear response approach to the calculation of the effective interaction parameters in the LDA+U method. *Phys. Rev. B*, 71:035105, Jan 2005.

[74] Yu Meng, Xing-Wu Liu, Chun-Fang Huo, Wen-Ping Guo, Dong-Bo Cao, Qing Peng, Albert Dearden, Xavier Gonze, Yong Yang, Jianguo Wang, Haijun Jiao, Yongwang Li, and Xiao-Dong Wen. When density functional approximations meet iron oxides. *Journal of Chemical Theory and Computation*, 12(10):5132–5144, September 2016.

[75] S. Lebègue, S. Pillet, and J. G. Ángyán. Modeling spin-crossover compounds by periodic dft+u approach. *Physical Review B*, 78(2), July 2008.

[76] Marçal Capdevila-Cortada, Zbigniew Łodziana, and Núria López. Performance of dft+u approaches in the study of catalytic materials. *ACS Catalysis*, 6(12):8370–8379, November 2016.

[77] Patrick Bruno. Tight-binding approach to the orbital magnetic moment and magnetocrystalline anisotropy of transition-metal monolayers. *Phys. Rev. B*, 39:865–868, Jan 1989.

[78] Gerrit van der Laan. Microscopic origin of magnetocrystalline anisotropy in transition metal thin films. *Journal of Physics: Condensed Matter*, 10(14):3239–3253, 1998.

[79] Juarez L. F. Da Silva, M. Verónica Ganduglia-Pirovano, Joachim Sauer, Veronika Bayer, and Georg Kresse. Hybrid functionals applied to rare-earth oxides: The example of ceria. *Physical Review B*, 75(4), January 2007.

[80] Michael Nolan, Stephen C. Parker, and Graeme W. Watson. The electronic structure of oxygen vacancy defects at the low index surfaces of ceria. *Surface Science*, 595(1-3):223–232, December 2005.

[81] Tribhuwan Pandey and David S. Parker. Magnetic properties and magnetocrystalline anisotropy of nd_2fe_{17}, $nd_2fe_{17}x_3$, and related compounds. *Scientific Reports*, 8(1), feb 2018.

[82] Daliya S. Mathew and Ruey-Shin Juang. An overview of the structure and magnetism of spinel ferrite nanoparticles and their synthesis in microemulsions. *Chemical Engineering Journal*, 129(1):51–65, 2007.

[83] Santi Maensiri, Chivalrat Masingboon, Banjong Boonchom, and Supapan Seraphin. A simple route to synthesize nickel ferrite (nife2o4) nanoparticles using egg white. *Scripta Materialia*, 56(9):797–800, 2007.

[84] Kontad (formerly Suriya) Ounnunkad and Sukon Phanichphant. Cellulose-precursor synthesis of nanocrystalline co0.5cu0.5fe2o4 spinel ferrites. *Materials Research Bulletin*, 47(2):473–477, 2012.

[85] Chao Wei, Zhenxing Feng, Murat Baisariyev, Linghui Yu, Li Zeng, Tianpin Wu, Haiyan Zhao, Yaqin Huang, Michael J. Bedzyk, Thirumany Sritharan, and Zhichuan J. Xu. Valence change ability and geometrical occupation of substitution cations determine the pseudocapacitance of spinel ferrite xfe2o4 (x = mn, co, ni, fe). *Chemistry of Materials*, 28(12):4129–4133, 2016.

[86] Dereje H. Taffa, Ralf Dillert, Anna C. Ulpe, Katharina C.L. Bauerfeind, Thomas Bredow, Detlef W. Bahnemann, and Michael Wark. Photoelectrochemical and theoretical investigations of spinel type ferrites (mxfe3-xo4) for water splitting: a mini-review. *Journal of Photonics for Energy*, 7(1):1 – 25, 2016.

[87] Mozhdeh Peiravi, Hossein Eslami, Mojtaba Ansari, and Hadi Zare-Zardini. Magnetic hyperthermia: Potentials and limitations. *Journal of the Indian Chemical Society*, 99(1):100269, 2022.

[88] Daniel Fritsch and Claude Ederer. Epitaxial strain effects in the spinel ferrites cofe$_2$o$_4$ and nife$_2$o$_4$ from first principles. *Phys. Rev. B*, 82:104117, Sep 2010.

[89] Daniel Fritsch and Claude Ederer. First-principles calculation of magnetoelastic coefficients and magnetostriction in the spinel ferrites cofe$_2$o$_4$ and nife$_2$o$_4$. *Phys. Rev. B*, 86:014406, Jul 2012.

[90] Horng-Tay Jeng and G.Y. Guo. First-principles investigations of the magnetocrystalline anisotropy in strained co-substituted magnetite (cofe2o4). *Journal of Magnetism and Magnetic Materials*, 239(1):88–90, 2002. International Symposium on Physics of Magnetic Materials/Internat ional Symposium on Advanced Magnetic Technologies.

[91] V. N. Antonov, B. N. Harmon, and A. N. Yaresko. Electronic structure and x-ray magnetic circular dichroism in fe$_3$o$_4$ and mn-, Co−, or ni-substituted fe$_3$o$_4$. *Phys. Rev. B*, 67:024417, Jan 2003.

[92] Z. Szotek, W. M. Temmerman, D. Ködderitzsch, A. Svane, L. Petit, and H. Winter. Electronic structures of normal and inverse spinel ferrites from first principles. *Phys. Rev. B*, 74:174431, Nov 2006.

[93] Xu Zuo and Carmine Vittoria. Calculation of exchange integrals and electronic structure for manganese ferrite. *Phys. Rev. B*, 66:184420, Nov 2002.

[94] Ching Cheng. Long-range antiferromagnetic interactions in znfe$_2$o$_4$ and cdfe$_2$o$_4$: Density functional theory calculations. *Phys. Rev. B*, 78:132403, Oct 2008.

[95] S. Soliman, A. Elfalaky, Gerhard H. Fecher, and Claudia Felser. Electronic structure calculations for znfe$_2$o$_4$. *Phys. Rev. B*, 83:085205, Feb 2011.

[96] Daniel Fritsch. Electronic and optical properties of spinel zinc ferrite:ab initiohybrid functional calculations. *Journal of Physics: Condensed Matter*, 30(9):095502, feb 2018.

[97] J.J. Melo Quintero, C.E. Rodríguez Torres, and L.A. Errico. Ab initio calculation of structural, electronic and magnetic properties and hyperfine parameters at the fe sites of pristine znfe2o4. *Journal of Alloys and Compounds*, 741:746–755, 2018.

[98] J.J. Melo Quintero, K.L. Salcedo Rodríguez, C.E. Rodríguez Torres, and L.A. Errico. Ab initio study of the role of defects on the magnetic response and the structural, electronic and hyperfine properties of znfe2o4. *Journal of Alloys and Compounds*, 775:1117–1128, 2019.

[99] J. Melo Quintero, K.L. Salcedo Rodríguez, F.A. Gómez Albarracín, H.D. Rosales, P. Mendoza Zélis, S.J. Stewart, L.A. Errico, and C. Rodríguez Torres. On the deviation from a curie–weiss behavior of the znfe2o4 susceptibility: A combined ab-initio and monte-carlo approach. *Heliyon*, 5(1):e01170, 2019.

[100] Daniel Fritsch and Claude Ederer. Effect of epitaxial strain on the cation distribution in spinel ferrites cofe2o4 and nife2o4: A density functional theory study. *Applied Physics Letters*, 99(8):081916, 2011.

[101] G. A. Sawatzky, F. Van Der Woude, and A. H. Morrish. Mössbauer study of several ferrimagnetic spinels. *Phys. Rev.*, 187:747–757, Nov 1969.

[102] L. Braicovich, A. Tagliaferri, G. van der Laan, G. Ghiringhelli, and N. B. Brookes. Sum rules in x-ray resonant raman scattering: Recovering the co ground state information in $cofe_2o_4$ as a test case. *Phys. Rev. Lett.*, 90:117401, Mar 2003.

[103] B. Lakshmi, Babitto Joe Thomas, and Pramod Gopinath. Accurate band gap determination of chemically synthesized cobalt ferrite nanoparticles using diffuse reflectance spectroscopy. *Advanced Powder Technology*, 32(10):3706–3716, 2021.

[104] B. S. Holinsworth, D. Mazumdar, H. Sims, Q.-C. Sun, M. K. Yurtisigi, S. K. Sarker, A. Gupta, W. H. Butler, and J. L. Musfeldt. Chemical tuning of the optical band gap in spinel ferrites: Cofe2o4 vs nife2o4. *Applied Physics Letters*, 103(8):082406, 2013.

[105] H.M. El-Sayed and W.R. Agami. Controlling of optical energy gap of co-ferrite quantum dots in poly (methyl methacrylate) matrix. *Superlattices and Microstructures*, 83:651–658, 2015.

[106] Cameliu Himcinschi, Ionela Vrejoiu, Georgeta Salvan, Michael Fronk, Andreas Talkenberger, Dietrich R. T. Zahn, David Rafaja, and Jens Kortus. Optical and magneto-optical study of nickel and cobalt ferrite epitaxial thin films and submicron structures. *Journal of Applied Physics*, 113(8):084101, 2013.

[107] D. Carta, M. F. Casula, A. Falqui, D. Loche, G. Mountjoy, C. Sangregorio, and A. Corrias. A structural and magnetic investigation of the inversion degree in ferrite nanocrystals mfe2o4 (m = mn, co, ni). *The Journal of Physical Chemistry C*, 113(20):8606–8615, 2009.

[108] Qi C. Sun, Christina S. Birkel, Jinbo Cao, Wolfgang Tremel, and Janice L. Musfeldt. Spectroscopic signature of the superparamagnetic transition and surface spin disorder in cofe2o4 nanoparticles. *ACS Nano*, 6(6):4876–4883, 2012. PMID: 22540958.

[109] Maurizio De Santis, Aude Bailly, Ian Coates, Stéphane Grenier, Olivier Heckmann, Karol Hricovini, Yves Joly, Véronique Langlais, Aline Y. Ramos, Christine Richter, Xavier Torrelles, Stéphanie Garaudée, Olivier Geaymond, and Olivier Ulrich. Epitaxial growth and structure of cobalt ferrite thin films with large inversion parameter on Ag(001). *Acta Crystallographica Section B*, 75(1):8–17, Feb 2019.

[110] R. M. Bozorth, Elizabeth F. Tilden, and Albert J. Williams. Anisotropy and magnetostriction of some ferrites. *Phys. Rev.*, 99:1788–1798, Sep 1955.

[111] Henry Shenker. Magnetic anisotropy of cobalt ferrite ($co_{1.01}fe_{2.00}o_{3.62}$) and nickel cobalt ferrite ($ni_{0.72}fe_{0.20}co_{0.08}fe_2o_4$). *Phys. Rev.*, 107:1246–1249, Sep 1957.

[112] A.C. Lima, M.A. Morales, J.H. Araújo, J.M. Soares, D.M.A. Melo, and A.S. Carriço. Evaluation of (bh)max and magnetic anisotropy of cobalt ferrite nanoparticles synthesized in gelatin. *Ceramics International*, 41(9, Part B):11804–11809, 2015.

[113] Jiabao Yi Jianhua Yin Binghai Liu, Jun Ding and Zhili Dong. Magnetic anisotropies in cobalt-nickel ferrites (nixco1-xfe2o4). *J. Korean Phy. Soc.*, 52, 2008.

[114] Jhih-Rong Huang and Ching Cheng. Cation and magnetic orders in mnfe2o4 from density functional calculations. *Journal of Applied Physics*, 113(3):033912, 2013.

[115] O. Mounkachi, R. Lamouri, E. Salmani, M. Hamedoun, A. Benyoussef, and H. Ez-Zahraouy. Origin of the magnetic properties of mnfe2o4 spinel ferrite: Ab initio and monte carlo simulation. *Journal of Magnetism and Magnetic Materials*, 533:168016, 2021.

[116] Q. C. Sun, H. Sims, D. Mazumdar, J. X. Ma, B. S. Holinsworth, K. R. O'Neal, G. Kim, W. H. Butler, A. Gupta, and J. L. Musfeldt. Optical band gap hierarchy in a magnetic oxide: Electronic structure of $nife_2o_4$. *Phys. Rev. B*, 86:205106, Nov 2012.

[117] F.K. Lotgering. Semiconduction and cation valencies in manganese ferrites. *Journal of Physics and Chemistry of Solids*, 25(1):95–103, 1964.

[118] Rashmi Tiwari, Manojit De, H.S. Tewari, and S.K. Ghoshal. Structural and magnetic properties of tailored nife2o4 nanostructures synthesized using auto-combustion method. *Results in Physics*, 16:102916, 2020.

[119] Cesar Tejera-Centeno and Silvia Gallego. Interface effects in combined soft/hard ferrite permanent magnets. *Journal of Physics D: Applied Physics*, 54(26):264001, apr 2021.

[120] W. F. Pong, Y. K. Chang, M. H. Su, P. K. Tseng, H. J. Lin, G. H. Ho, K. L. Tsang, and C. T. Chen. Magnetic orientation of ni in zn-ni ferrites studied by soft-x-ray magnetic circular dichroism. *Phys. Rev. B*, 55:11409–11413, May 1997.

[121] Min Feng, Xu Zuo, Carmine Vittoria, Vincent G. Harris, and Jian Wu. Ab initio study on manganese doped cadmium ferrite ($Cd_{1-x}Mn_xFe_2O_4$), 2011.

[122] Clara Pereira, André M. Pereira, Carlos Fernandes, Mariana Rocha, Ricardo Mendes, María Paz Fernández-García, Alexandra Guedes, Pedro B. Tavares, Jean-Marc Grenèche, João P. Araújo, and Cristina Freire. Superparamagnetic mfe2o4 (m = fe, co, mn) nanoparticles: Tuning the particle size and magnetic properties through a novel one-step coprecipitation route. *Chemistry of Materials*, 24(8):1496–1504, Apr 2012.

[123] Julius M. Hastings and Lester M. Corliss. Neutron diffraction study of manganese ferrite. *Phys. Rev.*, 104:328–331, Oct 1956.

[124] Khairul Islam, Manjurul Haque, Arup Kumar, Amitra Hoq, Fahmeed Hyder, and Sheikh Manjura Hoque. Manganese ferrite nanoparticles (mnfe2o4): Size dependence for hyperthermia and negative/positive contrast enhancement in mri. *Nanomaterials*, 10(11), 2020.

[125] B.D. Cullity and C.D. Graham. *Introduction to magnetic materials*. John Wiley & Sons, Ltd, 2008.

[126] K. Kamazawa, Y. Tsunoda, H. Kadowaki, and K. Kohn. Magnetic neutron scattering measurements on a single crystal of frustrated $znfe_2o_4$. *Phys. Rev. B*, 68:024412, Jul 2003.

[127] Yu G Chukalkin and VR Shtirts. Characteristics of the magnetic state of znfe2o4. *Sov. Phys. Solid State*, 30:1683–1686, 1988.

[128] W. Schiessl, W. Potzel, H. Karzel, M. Steiner, G. M. Kalvius, A. Martin, M. K. Krause, I. Halevy, J. Gal, W. Schäfer, G. Will, M. Hillberg, and R. Wäppling. Magnetic properties of the $znfe_2o_4$ spinel. *Phys. Rev. B*, 53:9143–9152, Apr 1996.

[129] U. König, E.F. Bertaut, Y. Gros, M. Mitrikov, and G. Chol. Models of the magnetic structure of zinc ferrite. *Solid State Communications*, 8(10):759–764, 1970.

[130] S.-H. Lee, C. Broholm, T. H. Kim, W. Ratcliff, and S-W. Cheong. Local spin resonance and spin-peierls-like phase transition in a geometrically frustrated antiferromagnet. *Phys. Rev. Lett.*, 84:3718–3721, Apr 2000.

[131] B. Jeyadevan, K. Tohji, and K. Nakatsuka. Structure analysis of coprecipitated znfe2o4 by extended x-ray-absorption fine structure. *Journal of Applied Physics*, 76(10):6325–6327, 1994.

[132] Lisha Raghavan, Geetha Pookat, Hysen Thomas, Sunil Ojha, D.K. Avasthi, and M.R. Anantharaman. Room temperature ferrimagnetism and low temperature disorder effects in zinc ferrite thin films. *Journal of Magnetism and Magnetic Materials*, 385:265–271, 2015.

[133] B. N. Sahu, K. G. Suresh, N. Venkataramani, Shiva Prasad, and R. Krishnan. Temperature and field dependent magnetization studies on nano-crystalline znfe2o4 thin films. *AIP Advances*, 8(5):056118, 2018.

[134] Y F Chen, D Spoddig, and M Ziese. Epitaxial thin film ZnFe2o4: a semi-transparent magnetic semiconductor with high curie temperature. *Journal of Physics D: Applied Physics*, 41(20):205004, sep 2008.

[135] Murtaza Bohra, Shiva Prasad, Naresh Kumar, D. S. Misra, S. C. Sahoo, N. Venkataramani, and R. Krishnan. Large room temperature magnetization in nanocrystalline zinc ferrite thin films. *Applied Physics Letters*, 88(26):262506, 2006.

[136] T. Böntgen, K. Brachwitz, R. Schmidt-Grund, M. Lorenz, and M. Grundmann. Vacuum ultraviolet dielectric function of znfe2o4 thin films. *Journal of Applied Physics*, 113(7):073503, 2013.

[137] Chao Jin, Peng Li, Wenbo Mi, and Haili Bai. Structure, magnetic, and transport properties of epitaxial znfe2o4 films: An experimental and first-principles study. *Journal of Applied Physics*, 115(21):213908, 2014.

[138] E. Lišková-Jakubisová, Š. Višňovský, P. Široký, D. Hrabovský, J. Pištora, Subasa C. Sahoo, Shiva Prasad, N. Venkataramani, Murtaza Bohra, and R. Krishnan. Nanocrystalline zinc ferrite films studied by magneto-optical spectroscopy. *Journal of Applied Physics*, 117(17):17B726, 2015.

[139] D. V. Kurmude, C. M. Kale, P. S. Aghav, D. R. Shengule, and K. M. Jadhav. Superparamagnetic behavior of zinc-substituted nickel ferrite nanoparticles and its effect on mossbauer and magnetic parameters. *Journal of Superconductivity and Novel Magnetism*, 27(8):1889–1897, Aug 2014.

[140] Jeong Hyun Shim, Soonchil Lee, Jung Hye Park, Seung-Jin Han, Y. H. Jeong, and Young Whan Cho. Coexistence of ferrimagnetic and antiferromagnetic ordering in fe-inverted zinc ferrite investigated by nmr. *Phys. Rev. B*, 73:064404, Feb 2006.

[141] S. Ayyappan, S. Philip Raja, C. Venkateswaran, John Philip, and Baldev Raj. Room temperature ferromagnetism in vacuum annealed znfe2o4 nanoparticles. *Applied Physics Letters*, 96(14):143106, 2010.

[142] Jiangtao Wu, Nan Li, Jun Xu, Yaqi Jiang, Zuo-Guang Ye, Zhaoxiong Xie, and Lansun Zheng. Partially inverse spinel znfe2o4 with high saturation magnetization synthesized via a molten salt route. *Applied Physics Letters*, 99(20):202505, 2011.

[143] Chandana Rath, N. C. Mishra, S. Anand, R. P. Das, K. K. Sahu, Chandan Upadhyay, and H. C. Verma. Appearance of superparamagnetism on heating nanosize mn0.65zn0.35fe2o4. *Applied Physics Letters*, 76(4):475–477, 2000.

[144] Shengqiang Zhou, K. Potzger, D. Bürger, K. Kuepper, M. Helm, J. Fassbender, and H. Schmidt. Inverse spinel znfe2o4 nanoparticles synthesized by ion implantation and post-annealing: An investigation using x-ray spectroscopy and magneto-transport. *Nuclear Instruments and Methods in Physics Research Section B: Beam Interactions with Materials and Atoms*, 267(8):1620–1622, 2009. Proceedings of the 16th International Conference on Ion Beam Modification of Materials.

[145] A.A. Sattar, H.M. EL-Sayed, and Ibrahim ALsuqia. Structural and magnetic properties of cofe2o4/nife2o4 core/shell nanocomposite prepared by the hydrothermal method. *Journal of Magnetism and Magnetic Materials*, 395:89–96, 2015.

[146] Y.L. Huang, W.B. Fan, Y.H. Hou, K.X. Guo, Y.F. Ouyang, and Z.W. Liu. Effects of intrinsic defects on the electronic structure and magnetic properties of cofe2o4: A first-principles study. *Journal of Magnetism and Magnetic Materials*, 429:263–269, 2017.

[147] Diego Gutiérrez, Michael Foerster, Ignasi Fina, Josep Fontcuberta, Daniel Fritsch, and Claude Ederer. Dielectric response of epitaxially strained $cofe_2o_4$ spinel thin films. *Phys. Rev. B*, 86:125309, Sep 2012.

[148] F. Rigato, J. Geshev, V. Skumryev, and J. Fontcuberta. The magnetization of epitaxial nanometric cofe2o4(001) layers. *Journal of Applied Physics*, 106(11):113924, 2009.

[149] M.C. Muñoz, S. Gallego, J.I. Beltrán, and J. Cerdá. Adhesion at metal–zro2 interfaces. *Surface Science Reports*, 61(7):303–344, 2006.

[150] Marco Sanna Angotzi, Valentina Mameli, Claudio Cara, Davide Peddis, Huolin L. Xin, Claudio Sangregorio, Maria Laura Mercuri, and Carla Cannas. On the synthesis of bi-magnetic manganese ferrite-based core–shell nanoparticles. *Nanoscale Adv.*, 3:1612–1623, 2021.

[151] Zichun Yan, Sara FitzGerald, Thomas M Crawford, and O Thompson Mefford. Manganese and cobalt substituted ferrite nanoparticles synthesized via a seed-mediated drip method. *Journal of Physics: Materials*, 4(3):034013, may 2021.

[152] Valentin Nica, Carlos Caro, Jose Maria Páez-Muñoz, Manuel Pernia Leal, and Maria Luisa Garcia-Martin. Bi-magnetic core-shell cofe2o4@mnfe2o4 nanoparticles for in vivo theranostics. *Nanomaterials*, 10(5), 2020.

[153] Takeshi Tainosho, Jun-ichiro Inoue, Sonia Sharmin, Masaki Takeguchi, Eiji Kita, and Hideto Yanagihara. Large negative uniaxial magnetic anisotropy in highly distorted co-ferrite thin films. *Applied Physics Letters*, 114(9):092408, 2019.

[154] H. Landolt and R. Börnstein. *Numerical data and functional relationships in science and technology: Crystal and solid state physics. New series. Group 3.* Zahlenwerte und Funktionen aus Naturwissenschaften

und Technik: Kristall- und Festkörperphysik. Gruppe 3. Springer., 1969.

[155] C. R. Stein, M. T. S. Bezerra, G. H. A. Holanda, J. André-Filho, and P. C. Morais. Structural and magnetic properties of cobalt ferrite nanoparticles synthesized by co-precipitation at increasing temperatures. *AIP Advances*, 8(5):056303, 2018.

[156] S Nasir and M Anis ur Rehman. Structural, electrical and magnetic studies of nickel–zinc nanoferrites prepared by simplified sol–gel and co-precipitation methods. *Physica Scripta*, 84(2):025603, aug 2011.

[157] A Sutka, K A Gross, G Mezinskis, G Bebris, and M Knite. The effect of heating conditions on the properties of nano- and microstructured ni–zn ferrite. *Physica Scripta*, 83(2):025601, jan 2011.

[158] C.N. Anumol, M. Chithra, M. Govindaraj Shalini, and Subasa C. Sahoo. Effect of annealing on structural and magnetic properties of nife2o4/znfe2o4 nanocomposites. *Journal of Magnetism and Magnetic Materials*, 469:81–88, 2019.

[159] Néel, M. Louis. Propriétés magnétiques des ferrites ; ferrimagnétisme et antiferromagnétisme. *Ann. Phys.*, 12(3):137–198, 1948.

[160] A.I. Nandapure, S.B. Kondawar, P.S. Sawadh, and B.I. Nandapure. Effect of zinc substitution on magnetic and electrical properties of nanocrystalline nickel ferrite synthesized by refluxing method. *Physica B: Condensed Matter*, 407(7):1104–1107, 2012.

[161] Y.B. Kannan, R. Saravanan, N. Srinivasan, and I. Ismail. Sintering effect on structural, magnetic and optical properties of ni0.5zn0.5fe2o4 ferrite nano particles. *Journal of Magnetism and Magnetic Materials*, 423:217–225, 2017.

[162] AT Raghavender, RG Kulkarni, and KM Jadhav. Magnetic properties of nanocrystalline al doped nickel ferrite synthesized by the sol-gel method. *Chinese journal of physics*, 46(3):366–375, 2008.

[163] PBC Rao and SP Setty. Electrical properties of ni-zn nano ferrite particles. *International Journal of Engineering Science and Technology*, 2(8):3351–3354, 2010.

[164] A.S. Džunuzović, N.I. Ilić, M.M. Vijatović Petrović, J.D. Bobić, B. Stojadinović, Z. Dohčević-Mitrović, and B.D. Stojanović. Structure and

properties of ni–zn ferrite obtained by auto-combustion method. *Journal of Magnetism and Magnetic Materials*, 374:245–251, 2015.

[165] Abdollah Hajalilou, Saiful Amri Mazlan, and Kamyar Shameli. A comparative study of different concentrations of pure zn powder effects on synthesis, structure, magnetic and microwave-absorbing properties in mechanically-alloyed ni–zn ferrite. *Journal of Physics and Chemistry of Solids*, 96-97:49–59, 2016.

[166] A. Narayanasamy and N. Sivakumar. Influence of mechanical milling and thermal annealing on electrical and magnetic properties of nanostructured ni-zn and cobalt ferrites. *Bulletin of Materials Science*, 31:373–380, 2008.

[167] Ch. Srinivas, E. Ranjith Kumar, B.V. Tirupanyam, Sher Singh Meena, Pramod Bhatt, C.L. Prajapat, T.V. Chandrasekhar Rao, and D.L. Sastry. Study of magnetic behavior in co-precipitated ni–zn ferrite nanoparticles and their potential use for gas sensor applications. *Journal of Magnetism and Magnetic Materials*, 502:166534, 2020.

[168] G. Alvarez, H. Montiel, J.F. Barron, M.P. Gutierrez, and R. Zamorano. Yafet–kittel-type magnetic ordering in ni0.35zn0.65fe2o4 ferrite detected by magnetosensitive microwave absorption measurements. *Journal of Magnetism and Magnetic Materials*, 322(3):348–352, 2010.

[169] David A. Andersson and Christopher R. Stanek. Mixing and non-stoichiometry in fe–ni–cr–zn–o spinel compounds: density functional theory calculations. *Phys. Chem. Chem. Phys.*, 15:15550–15564, 2013.

[170] W. F. Pong, M. H. Su, M.-H. Tsai, H. H. Hsieh, J. Y. Pieh, Y. K. Chang, K. C. Kuo, P. K. Tseng, J. F. Lee, S. C. Chung, C. I. Chen, K. L. Tsang, and C. T. Chen. Oxygen 1s x-ray-absorption near-edge structure of zn-ni ferrites: A comparison with the theoretical calculations. *Phys. Rev. B*, 54:16641–16645, Dec 1996.

[171] X.F. Zhu and L.F. Chen. First-principles study of the electronic and magnetic properties of a nickel-zinc ferrite: Znxni1-xfe2o4. *Journal of Magnetism and Magnetic Materials*, 323(23):3138–3142, 2011.

[172] A. Manikandan, L. John Kennedy, M. Bououdina, and J. Judith Vijaya. Synthesis, optical and magnetic properties of pure and co-doped znfe2o4 nanoparticles by microwave combustion method. *Journal of Magnetism and Magnetic Materials*, 349:249–258, 2014.

[173] Daniel Peeters, Dereje H. Taffa, Marissa M. Kerrigan, Andreas Ney, Niels Jöns, Detlef Rogalla, Stefan Cwik, Hans-Werner Becker, Markus Grafen, Andreas Ostendorf, Charles H. Winter, Sumit Chakraborty, Michael Wark, and Anjana Devi. Photoactive zinc ferrites fabricated via conventional cvd approach. *ACS Sustainable Chemistry & Engineering*, 5(4):2917–2926, 2017.

[174] Jennifer Hölscher, Henrik Lyder Andersen, Matilde Saura-Múzquiz, Pelle Gorm Garbus, and Mogens Christensen. Correlation between microstructure, cation distribution and magnetism in ni1-xznxfe2o4 nanocrystallites. *CrystEngComm*, 22:515–524, 2020.